



Cosmic-Ray Transport in Simulations of Star-forming Galactic Disks

Lucia Armillotta¹ , Eve C. Ostriker¹ , and Yan-Fei Jiang (姜燕飞)² ¹ Department of Astrophysical Sciences, Princeton University, Princeton, NJ 08544, USA; lucia.armillotta@princeton.edu² Center for Computational Astrophysics, Flatiron Institute, New York, NY 10010, USA

Received 2021 May 19; revised 2021 July 15; accepted 2021 August 4; published 2021 November 15

Abstract

Cosmic-ray transport on galactic scales depends on the detailed properties of the magnetized, multiphase interstellar medium (ISM). In this work, we postprocess a high-resolution TIGRESS magnetohydrodynamic simulation modeling a local galactic disk patch with a two-moment fluid algorithm for cosmic-ray transport. We consider a variety of prescriptions for the cosmic rays, from a simple, purely diffusive formalism with constant scattering coefficient, to a physically motivated model in which the scattering coefficient is set by the critical balance between streaming-driven Alfvén wave excitation and damping mediated by local gas properties. We separately focus on cosmic rays with kinetic energies of ~ 1 GeV (high-energy) and ~ 30 MeV (low energy), respectively important for ISM dynamics and chemistry. We find that simultaneously accounting for advection, streaming, and diffusion of cosmic rays is crucial for properly modeling their transport. Advection dominates in the high-velocity, low-density hot phase, while diffusion and streaming are more important in higher-density, cooler phases. Our physically motivated model shows that there is no single diffusivity for cosmic-ray transport: the scattering coefficient varies by four or more orders of magnitude, maximal at density $n_{\text{H}} \sim 0.01 \text{ cm}^{-3}$. The ion-neutral damping of Alfvén waves results in strong diffusion and nearly uniform cosmic-ray pressure within most of the mass of the ISM. However, cosmic rays are trapped near the disk midplane by the higher scattering rate in the surrounding lower-density, higher-ionization gas. The transport of high-energy cosmic rays differs from that of low-energy cosmic rays, with less effective diffusion and greater energy losses for the latter.

Unified Astronomy Thesaurus concepts: Cosmic rays (329); Magnetohydrodynamics (1964); Interstellar medium (847)

1. Introduction

Cosmic rays (CRs) are charged particles moving with relativistic speeds, observed over more than ten orders of magnitude in energy with a (broken) power-law distribution. Mainly generated within disk galaxies through shock acceleration in supernova remnants (e.g., Bell 1978; Blandford & Ostriker 1978; Schlickeiser 1989), CRs easily spread throughout the interstellar medium (ISM) thanks to their quasi-collisionless nature. In the Milky Way’s disk, the energy density of CRs—dominated by protons with kinetic energies of a few GeV (see reviews by Strong et al. 2007; Grenier et al. 2015)—is approximately in equipartition with the thermal, turbulent, and magnetic energy densities (e.g., Boulares & Cox 1990; Beck 2001). This suggests that CRs can significantly contribute to the dynamics of the ISM, potentially aiding in the internal support against gravity and/or helping to drive galactic winds. Additionally, CR ionization is very important in the dense gas that is shielded from UV, providing heating, driving chemical reactions, and maintaining the coupling to magnetic fields (e.g., Padovani et al. 2020). CRs therefore play several important roles in the evolution of galaxies.

The interaction between CRs and the surrounding gas is mostly mediated by the ambient magnetic field. Being charged particles, CRs gyrate around and stream along magnetic field lines, while scattering off of magnetic fluctuations on spatial scales of order the CR gyroradius. Scattering reduces the mean free path and effective propagation speed of CRs, thus allowing them to couple with the background thermal gas.

There are two main scenarios for the origin of magnetic fluctuations that scatter CRs, namely “self-confinement” and “extrinsic turbulence.” In the former scenario, the fluctuations

are Alfvén waves amplified by resonant streaming instabilities of CRs that develop when the bulk flow speed of the CR distribution exceeds the Alfvén speed in the background plasma (Kulsrud & Pearce 1969; Wentzel 1974). Scattering by resonant Alfvén waves isotropizes the CRs in the reference frame of the wave, tending to reduce streaming to the local Alfvén speed (e.g., Kulsrud 2005; Bai et al. 2019). However, damping mechanisms, including ion-neutral damping (Kulsrud & Pearce 1969), nonlinear Landau damping (Kulsrud 2005), linear Landau damping (Wiener et al. 2018), and turbulent damping (Farmer & Goldreich 2004; Lazarian 2016; Holguin et al. 2019) limit Alfvén wave amplification and therefore the CR scattering rate. In the extrinsic turbulence picture, the magnetic fluctuations are driven by mechanisms independent of CRs, such as turbulent cascades or other energy injection sources (e.g., Chandran 2000; Yan & Lazarian 2002). The same damping mechanisms mentioned above would also dissipate the magnetic energy of extrinsically driven MHD waves, thus reducing the rate of CR scattering (e.g., Xu & Lazarian 2017).

In both scenarios, the net CR flux is down the pressure gradient, and the magnetic field mediates the transfer of momentum from the CR distribution to the background gas. In addition to momentum, the self-confinement regime damping of Alfvén waves transfers energy to the surrounding gas at nearly the same rate waves are excited by CRs. In the extrinsic turbulence scenario, provided that the MHD waves have no preferred direction of propagation, CRs do not stream along with the waves. As a consequence, there is no transfer of energy from the CR distribution to the waves and, due to wave damping, from the waves to the gas. Instead, energy can flow from the waves to the CRs through second-order Fermi

acceleration (see reviews by Zweibel 2013, 2017 for a detailed overview of the two scenarios).

Since frequent wave–particle scattering can make the CR mean free path very short compared to other length scales of interest, in most astrophysical studies of ISM dynamics it is appropriate to treat CRs as a fluid. The transport of the CR fluid can be described in terms of diffusion relative to the hydromagnetic wave frame and advection along with the background magnetic field by thermal gas. In the self-confinement picture, the wave frame moves at the Alfvén speed, so this streaming has to be included together with diffusion and advection in the fluid treatment.

Estimates for the Milky Way disk suggest that self-confinement via resonant streaming instability is the dominant effect mediating transport for CRs with kinetic energies lower than a few tens of GeV (e.g., Zweibel 2013, 2017; Evoli et al. 2018). For CRs with higher energies, the growth rate of streaming instability rapidly decreases with increasing CR energy while the background turbulence has higher amplitude, so that scattering by extrinsic turbulence becomes more and more important (Sikl 1971; Blasi et al. 2012, see also Sections 2.2.3 and 2.2.4). Since the majority of the total energy density in CRs is held in particles with kinetic energies of a few GeV, while ionization is provided by CRs at even lower energy, the self-confinement CR transport framework is most relevant to understanding the effects of CRs on the background thermal gas. As we discuss in Section 2.2.3, for our calculations (focusing on GeV and lower energy) we shall consider self-generated waves rather than external turbulence for scattering. We do not investigate the CR acceleration mechanism itself.

As interaction with CRs represents a significant source of energy and momentum for the surrounding gas, understanding how they impact the ISM dynamics on galactic scales has been central in recent studies of galaxy evolution. Both analytic models (e.g., Breitschwerdt et al. 1991; Everett et al. 2008; Dorfi & Breitschwerdt 2012; Mao & Ostriker 2018) and magnetohydrodynamical (MHD) simulations of isolated galaxies or cosmological zoom-ins (e.g., Hanasz et al. 2013; Pakmor et al. 2016; Ruszkowski et al. 2017; Hopkins et al. 2021; Werhahn et al. 2021) and portions of ISM (e.g., Girichidis et al. 2016, 2018; Simpson et al. 2016; Farber et al. 2018) have demonstrated that CRs may play an important role in driving galactic outflows, regulating the level of star formation in disks, and shaping the multiphase gas distribution in the circumgalactic medium. However, the degree to which CRs affect these phenomena is strongly sensitive to the way different CR transport mechanisms, i.e., diffusion, streaming, and advection, are treated in the model (e.g., Ruszkowski et al. 2017; Chan et al. 2019).

The uncertainty regarding a fluid prescription for CR transport is mainly due to the complicated microphysical processes at play and to the consequent difficulty of connecting the microscales comparable to the CR gyroradius, where scattering takes place, to the macroscales of the galaxies. Historically, most studies of CR propagation on galactic scales have focused on our Galaxy and have made use of direct measurements of CR energy density and abundances of nuclei to constrain the details of the transport process, generally treated via an energy-dependent diffusive formalism (e.g., Cummings et al. 2016; Guo et al. 2016; Jóhannesson et al. 2016; Korsmeier & Cuoco 2016, see also review by Amato & Blasi 2018 and references therein). This approach is very

effective in representing the observable consequences of CR propagation to reproduce most of the available data in great detail. However, the prescriptions for the underlying gas distribution are generally highly simplified, assume spatially constant CR diffusivity that ignores the multiphase structure of the gas, and often neglect bulk transport via advection and streaming. These assumptions are certainly inaccurate (e.g., Crocker et al. 2021; Krumholz et al. 2020; Hopkins et al. 2021). Clearly, treating the different mechanisms involved in the CR transport as a function of the background gas properties is required for a more physical characterization of CR propagation on galactic scales and coupling with the surrounding plasma. At the same time, numerical studies of CR-ISM interactions are most meaningful if the ISM treatment accurately represents the physics of the multiphase, magnetized gas (including self-consistent treatment of star formation and feedback) at sufficiently high spatial resolution.

Beyond ISM dynamics, understanding how CRs propagate within galaxies is also crucial to investigate their effect on the chemistry of the gas. While CRs with relatively high kinetic energies (a few GeV) interact with the background gas mostly through collisionless processes, CRs with kinetic energies lower than 100 MeV are an important source of collisional ionization and heating of the ISM. While their small contribution to the total CR energy density makes low-energy CRs irrelevant to galactic-scale gas dynamics, they deeply impact the thermal, chemical, and dynamical evolution of the densest regions of the ISM, which are otherwise shielded from ionizing photons (see reviews by Grenier et al. 2015; Padovani et al. 2020). In particular, by heating and ionizing the background gas, CRs affect its temperature and couple it to the magnetic field, respectively. Both these effects are crucial to the internal dynamics of dense molecular clouds, including self-gravitating fragmentation, and as a consequence to the rate and character of star formation.

The goal of this paper is to investigate the propagation of CRs in a galactic environment (mass-containing disk + low-density corona) with conditions typical of the Sun’s environment in the Milky Way. For this purpose, we extract a set of snapshots from the TIGRESS³ MHD simulation modeling a patch of galactic disk representative of our solar neighborhood (Kim & Ostriker 2017, 2018). For each snapshot, we compute the propagation of CRs depending on the underlying distribution of thermal gas density, velocity, and magnetic field. The advantage of the TIGRESS simulations is that star cluster formation and feedback from supernovae are modeled in a self-consistent manner. This provides a realistic representation of the multiphase ISM and of the distribution of supernovae—assumed to be the only source of CRs in our models—within it. The original TIGRESS simulations do not include CRs, so in this work we calculate the transport of CRs by postprocessing the selected simulation snapshots. The back-reaction of thermal gas and magnetic field to the CR pressure is therefore not directly investigated in this paper.

In this work, we shall consider a variety of models to compute the transport of CRs, from simple models with either constant diffusion or streaming only, to a more detailed model in which the rate of CR scattering varies with the properties of the background gas in-line with the predictions of the self-confinement scenario. These models are separately applied to high-energy (~ 1 GeV)

³ Three-phase Interstellar medium in Galaxies Resolving Evolution with Star formation and Supernova feedback.

and low-energy (~ 30 MeV) CR protons since their propagation evolves in different ways. These two energies are chosen as representative of the portion of the CR distribution that is most important for dynamics and for chemistry, respectively. While the former are almost collisionless, the latter undergo more significant kinetic energy losses due to their effective Coulomb interactions with the dense ISM. Moreover, the growth rate of Alfvén waves depends on the CR energy, implying different drift velocities for CRs with different energies.

The layout of the paper is as follows. In Section 2, we briefly describe the TIGRESS framework and provide the details of the CR transport models used to infer the distribution of CRs in the solar neighborhood environment modeled by TIGRESS. In Sections 3 and 4, we analyze the distribution of high-energy CRs predicted by transport models assuming spatially constant and variable scattering coefficients, respectively. In Section 5, we present our results for the distribution of low-energy CRs assuming variable scattering coefficient only. In Section 6, we discuss our work in relation to observational findings and other recent computational work. Finally, in Section 7, we summarize our main results.

2. Methods

2.1. MHD Simulation

The MHD simulation postprocessed in this work is performed with the TIGRESS framework (Kim & Ostriker 2017), in which local patches of galactic disks are self-consistently modeled with resolved star formation and supernova feedback. Here, we briefly summarize the relevant features of the simulation, and refer to Kim & Ostriker (2017) for a more detailed description.

The TIGRESS framework is built on the grid-based MHD code *Athena* (Stone et al. 2008). The ideal MHD equations are solved in a shearing-periodic box (Stone & Gardiner 2010) representing a kiloparsec-sized patch of a differentially rotating galactic disk. This treatment guarantees uniformly high spatial resolution, which is crucial for a realistic representation of the multiphase ISM. For the study of CR propagation, this is particularly important since transport is quite different in different thermal phases of the gas. The low-density, hot ISM achieves very high velocity in winds that are escaping from the disk; the moderate-density, moderate-velocity warm gas fills most of the midplane volume and makes up the majority of the ISM mass—and also participates in extraplanar fountain flows; and the high-density gas hosts star-forming regions. The ionization state (which determines wave damping rates) and Alfvén speeds (which can limit streaming speeds) are also quite different in the different phases.

Additional physics in TIGRESS includes self-gravity from gas and young stars, a fixed external gravitational potential representing the stellar disk and the dark matter halo, optically thin cooling, and grain photoelectric heating. Sink particles are implemented to follow the formation of and gas accretion onto star clusters in regions where gravitational collapse occurs (see Kim et al. 2020a for an update in the treatment of sink particle accretion). Each sink/star particle is treated as a star cluster with a coeval stellar population that fully samples the Kroupa initial mass function (Kroupa 2001). Young massive stars (star particle age $t_{\text{sp}} \lesssim 40$ Myr) provide feedback to the ISM in the form of far-ultraviolet (FUV) radiation and supernova explosions. The instantaneous FUV luminosity and supernova rate

for each star cluster are determined from the STARBURST99 population synthesis model (Leitherer et al. 1999).

While TIGRESS simulations for several different galactic environments have been completed (Kim et al. 2020a), in this work we analyze the simulation modeling the solar neighborhood environment. This simulation is based on the same model parameters for which resolution studies were presented in Kim & Ostriker (2017), and for which the fountain and wind flows were analyzed in Kim & Ostriker (2018) and Vijayan et al. (2020). This model adopts galactocentric distance $R_0 = 8$ kpc, the angular velocity of local galactic rotation $\Omega = 28 \text{ km s}^{-1} \text{ kpc}^{-1}$, shear parameter $d \ln \Omega / d \ln R = -1$, and initial gas surface density $\Sigma = 13 M_{\odot} \text{ yr}^{-1}$. The simulation we analyze has box size $L_x = L_y = 1024$ pc and $L_z = 7168$ pc with a uniform spatial resolution $\Delta x = 8$ pc. While other versions of this model have been run at resolutions down to $\Delta x = 1$ pc, we choose the present simulation for computational efficiency. Kim & Ostriker (2017, 2018) demonstrated that a spatial resolution of 8 pc is sufficient to achieve robust convergence of several ISM and outflow properties, and in Appendix B we verify that a resolution of 8 pc guarantees convergence of CR properties as well. We find that models with resolution $\Delta x = 16$ pc are still converged, while models with lower resolution ($\Delta x \geq 32$ pc) are not converged in the distribution of CR pressure and are characterized by large temporal fluctuations.

As discussed in Kim & Ostriker (2017), the TIGRESS simulations (and similar simulations from other groups such as Gatto et al. 2017) are subject to transient effects at early times. After $t \approx 100$ Myr, the system has reached a self-regulated state: feedback from young massive stars drives turbulent motions and heats the ISM, thus providing the turbulent, thermal, and magnetic support needed to offset the vertical weight of the gas. Only a small fraction of the gas collapses to create the star clusters that supply the energy to maintain the ISM equilibrium. Some of the gas that is heated and accelerated by supernova explosions breaks out of the galactic plane into the coronal region, driving multiphase outflows consisting of hot winds and warm fountains. For the present work, we investigate the time range 200–550 Myr, covering many star formation/feedback cycles and outflow/inflow events (see Figure 1 in this paper and Figure 3 in Vijayan et al. 2020). We select and postprocess 10 snapshots at equal intervals within this time range (vertical dotted lines in Figure 1).

Figure 2 displays the distribution on the grid of several quantities from a sample MHD simulation snapshot at $t = 286$ Myr, when a strong outflow driven by supernova feedback is present. The upper (lower) set of panels shows x – z (x – y) projections along \hat{y} (\hat{z}) or slices at $y = 0$ ($z = 0$). From left to right, the upper/lower panels show: the hydrogen column density N_{H} overlaid with the star particle positions, hydrogen number density $n_{\text{H}} = \rho / (1.4 m_p)$, gas temperature T , gas speed v and direction, Alfvén speed $v_A = B / \sqrt{4\pi\rho}$ and direction, thermal pressure P_t , vertical kinetic pressure $P_{k,z} = \rho v_z^2$, and vertical magnetic stress $P_{m,z} = (B_x^2 + B_y^2 - B_z^2) / 8\pi$. Here, ρ is the gas mass density, B is the magnetic field magnitude, v_z is the gas velocity in the vertical direction, and B_x , B_y , and B_z are the magnetic field components along the x -, y -, and z -directions, respectively.

Thermal pressure, vertical kinetic pressure, and vertical magnetic stress provide support against the vertical weight of the gas. The arrows in the gas velocity and Alfvén speed slices

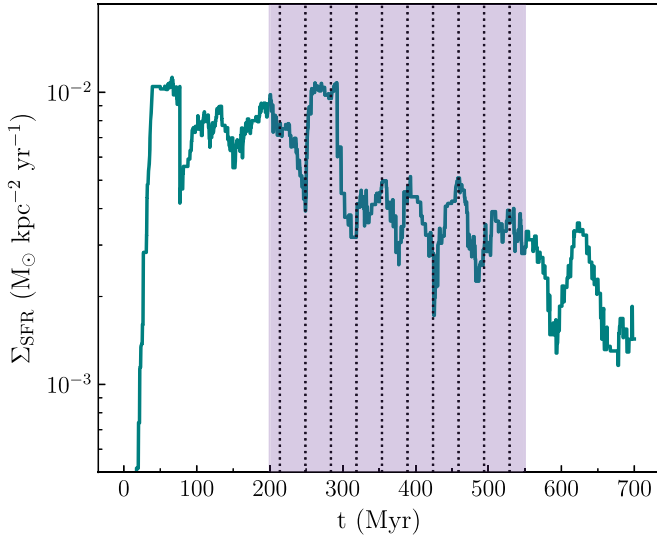


Figure 1. Star formation rate per unit area Σ_{SFR} as a function of time for clusters younger than 40 Myr in the TIGRESS simulation modeling the solar neighborhood environment. The shaded region denotes the time range investigated in this paper. The vertical dotted lines indicate the times of the snapshots postprocessed with the CR transport code.

indicate the projected direction of the gas velocity and Alfvén speed, respectively. We note that, while v and v_A are comparable in the warm/cold ($T \lesssim 10^4$ K) and moderate/high-density ($n_H \gtrsim 0.1 \text{ cm}^{-3}$) phase of the gas ($v \simeq v_A \simeq 10 \text{ km s}^{-1}$), the gas velocity dominates in the hot ($T > 10^6$ K) and rarefied ($n_H \lesssim 10^{-3} \text{ cm}^{-3}$) phase ($v \gg 100 \text{ km s}^{-1}$ and $v_A \lesssim 1 \text{ km s}^{-1}$). Moreover, while the gas velocity streamlines are outflowing for the hot gas in the extraplanar region ($|z| \gtrsim 300 \text{ pc}$), the motions are turbulent within the warm/cold gas. The magnetic field lines are primarily horizontal near the midplane, while aligning more (but not entirely) with the outflow velocities in the extraplanar region.

Figure 3 shows the volume-weighted and mass-weighted temperature-density and magnetic pressure-thermal pressure phase diagrams averaged over the 10 selected snapshots. The magnetic pressure is defined as $P_m = (B_x^2 + B_y^2 + B_z^2)/8\pi$. The dashed line in the magnetic pressure-thermal pressure diagram denotes equipartition, i.e., plasma $\beta = 1$, while the dotted and dotted-dashed lines indicate the relations plasma $\beta = 10$ and 100, respectively. The temperature-density diagrams indicate that the hot and warm gas components dominate in terms of volume—with the former widely distributed in the extraplanar region and the latter located mostly in the galactic disk and in a few clouds/filaments at higher latitudes (see Figure 2). The warm phase dominates the mass, with some contribution from the denser cold phase. The magnetic-thermal pressure diagram shows that, in terms of mass, most of the gas is characterized by rough equality between thermal and magnetic pressure. As clearly visible in Figure 2, thermal and magnetic pressures are nearly in equipartition in the denser portions of ISM. At higher latitudes, the magnetic pressure decreases much faster than the thermal pressure, especially in regions occupied by rarefied, hot gas. This explains why, in terms of volume, a significant fraction of gas has magnetic pressure well below the equipartition curve, while having moderate thermal pressure ($P_m \sim 0.1 - 0.01 P_t$ and $\log(P_t/k_B) \sim 2-3$). The locus with extremely low P_m and

moderately high P_t in the bottom-left panel represents the interior of superbubbles.

2.2. Postprocessing with Cosmic Ray

Each snapshot selected from the MHD simulation is postprocessed with the algorithm for CR transport implemented in the *Athena++* code (Stone et al. 2020) by Jiang & Oh (2018). CRs are treated as a relativistic fluid, whose energy and momentum evolution (in the absence of external sources and collisional losses) is described by the following two moment equations:

$$\frac{\partial e_c}{\partial t} + \nabla \cdot \mathbf{F}_c = -(\mathbf{v} + \mathbf{v}_s) \cdot \vec{\sigma}_{\text{tot}} \cdot [\mathbf{F}_c - \mathbf{v} \cdot (\vec{P}_c + e_c \vec{I})], \quad (1)$$

$$\frac{1}{v_m^2} \frac{\partial \mathbf{F}_c}{\partial t} + \nabla \cdot \vec{P}_c = -\vec{\sigma}_{\text{tot}} \cdot [\mathbf{F}_c - \mathbf{v} \cdot (\vec{P}_c + e_c \vec{I})], \quad (2)$$

where e_c and \mathbf{F}_c are the energy density and energy flux, respectively. We take the CR pressure tensor as approximately isotropic in the streaming frame, i.e., $\vec{P}_c \equiv P_c \vec{I}$, with $P_c = (\gamma_c - 1)e_c = e_c/3$, where $\gamma_c = 4/3$ is the adiabatic index of the relativistic fluid, and \vec{I} is the identity tensor. With these assumptions, the second term in the square brackets of Equations (1) and (2) becomes $(4/3)\mathbf{v}e_c$. These transport equations are supplemented by additional source and sink terms, to represent an injection of CR energy from supernovae and collisional losses (see Sections 2.2.1 and 2.2.2).

The CR streaming velocity,

$$\mathbf{v}_s = -v_{A,i} \frac{\mathbf{B} \cdot (\nabla \cdot \vec{P}_c)}{|\mathbf{B} \cdot (\nabla \cdot \vec{P}_c)|} = -v_{A,i} \frac{\hat{\mathbf{B}} \cdot \nabla P_c}{|\hat{\mathbf{B}} \cdot \nabla P_c|}, \quad (3)$$

is defined to have the same magnitude as the local Alfvén speed in the ions, $v_{A,i} \equiv \mathbf{B}/\sqrt{4\pi\rho_i}$, oriented along the local magnetic field and pointing down the CR pressure gradient. We note that the ion density, ρ_i , is the same as ρ for gas that is high enough temperature to be fully ionized (so that $|\mathbf{v}_s| = v_A$), but is low compared to ρ in the warm/cool gas (so that $|\mathbf{v}_s| = v_{A,i} \gg v_A$; see Section 2.2.5).

The speed v_m represents the maximum velocity CRs can propagate in the simulation. In principle, this should be equal to the speed of light. However, Jiang & Oh (2018) demonstrated that the simulation outcomes are not sensitive to the exact value of v_m as long as v_m is much larger than any other speed in the simulation; this “reduced speed of light” approximation is discussed in the context of two-moment radiation methods in Skinner & Ostriker (2013). Here, we adopt $v_m = 10^4 \text{ km s}^{-1}$, and, since all our simulations reach a steady state (see below), our results are insensitive to this choice.

The diagonal tensor $\vec{\sigma}_{\text{tot}}$ encodes the response to particle-wave interactions that cannot be resolved at macroscopic scales in the ISM. Along the direction of the magnetic field, the total coefficient,

$$\sigma_{\text{tot},\parallel}^{-1} = \sigma_{\parallel}^{-1} + \frac{v_{A,i}}{|\hat{\mathbf{B}} \cdot \nabla P_c|} (P_c + e_c), \quad (4)$$

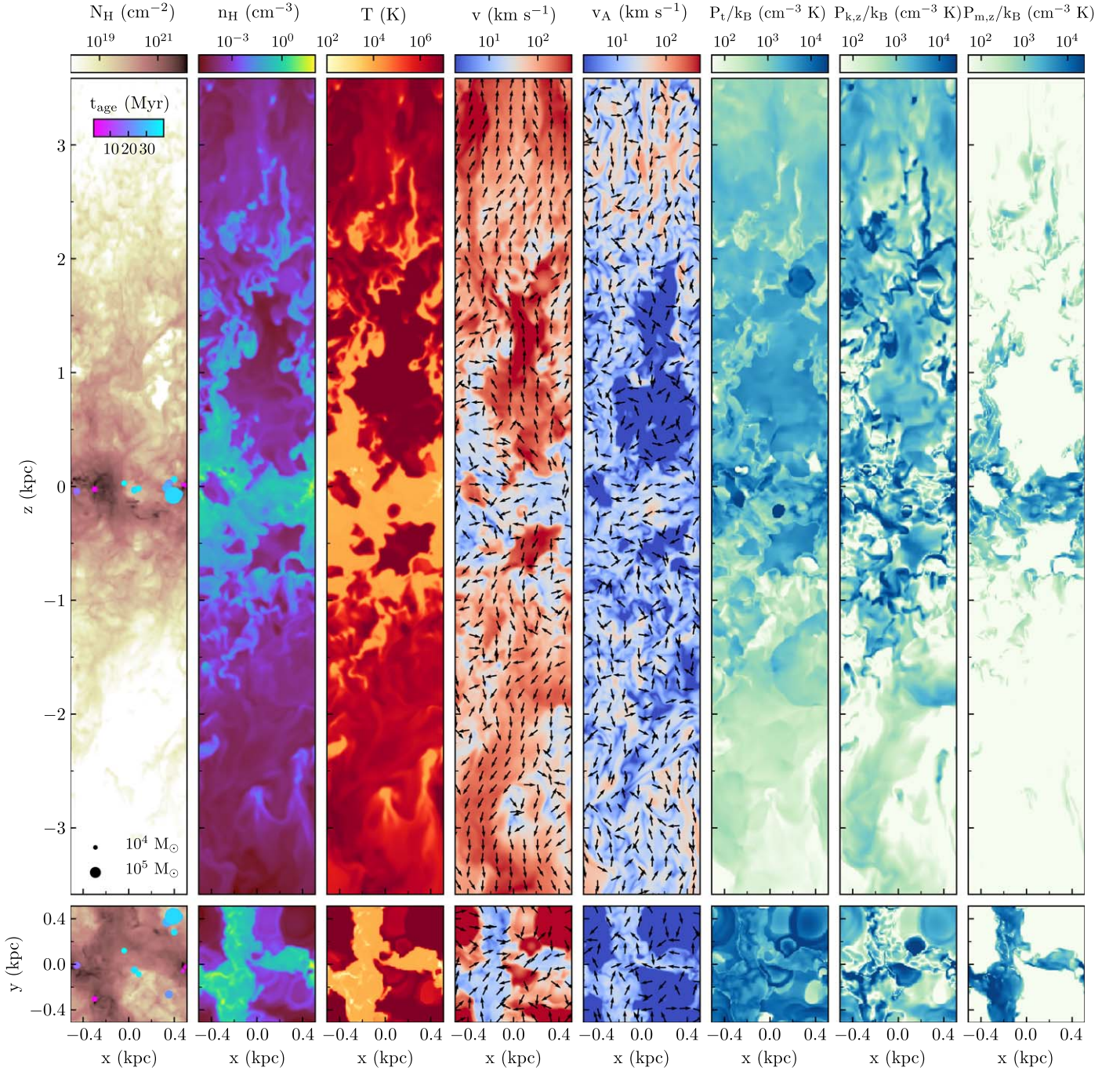


Figure 2. Sample snapshot ($t = 286$ Myr) from the TIGRESS simulation modeling the solar environment. The far-left panel shows the hydrogen number density projected along the y - (top panel) and z -direction (bottom panel). The projected positions of young ($t_{\text{sp}} \leq 40$ Myr) star particles are shown as colored circles, with size and color indicating their mass and mass-weighted age, respectively. Continuing to the right, the panels show the slices through the center of the simulation box of hydrogen number density n_{H} , gas temperature T , gas speed v , Alfvén speed v_{A} , thermal pressure P_{t} , kinetic vertical pressure $P_{k,z}$ and magnetic vertical stress $P_{m,z}$. The arrows overlaid on the gas velocity and Alfvén speed slices indicate the projected directions of the gas velocity and Alfvén speed, respectively. The thermal pressure, kinetic pressure, and magnetic stress are divided by the Boltzmann constant $k_{\text{B}} = 1.38 \times 10^{-16}$ erg K^{-1} .

allows for both scattering and streaming, while in the directions perpendicular to the magnetic field there is only scattering,

$$\sigma_{\text{tot},\perp} = \sigma_{\perp}. \quad (5)$$

For the relativistic case, $\sigma_{\parallel} = \nu_{\parallel}/c^2$ and $\sigma_{\perp} = \nu_{\perp}/c^2$ for ν_{\parallel} the scattering rate parallel to \hat{B} due to Alfvén waves that are resonant with the CR gyro-motion (see Section 2.2.3), and ν_{\perp} an effective perpendicular scattering rate.

In Equations (1) and (2), the left-hand side describes the transport of CRs in the simulation frame, while the right-hand side (rhs) represents the source and sink terms for the CR energy density or flux. In Equation (1), the term $-\mathbf{v} \cdot [\vec{\sigma}_{\text{tot}} (\mathbf{F}_{\text{c}} - 4/3 \nu_{\text{e}})]$ describes the direct CR pressure work done on or by the gas; in steady state this reduces to $\mathbf{v} \cdot \nabla P_{\text{c}}$ (and can be either positive or negative). The term $-\mathbf{v}_{\text{s}} \cdot [\vec{\sigma}_{\text{tot}} (\mathbf{F}_{\text{c}} - 4/3 \nu_{\text{e}})]$ represents the rate of energy transferred to the gas via wave damping; in steady state this becomes $\mathbf{v}_{\text{s}} \cdot \nabla P_{\text{c}}$. The

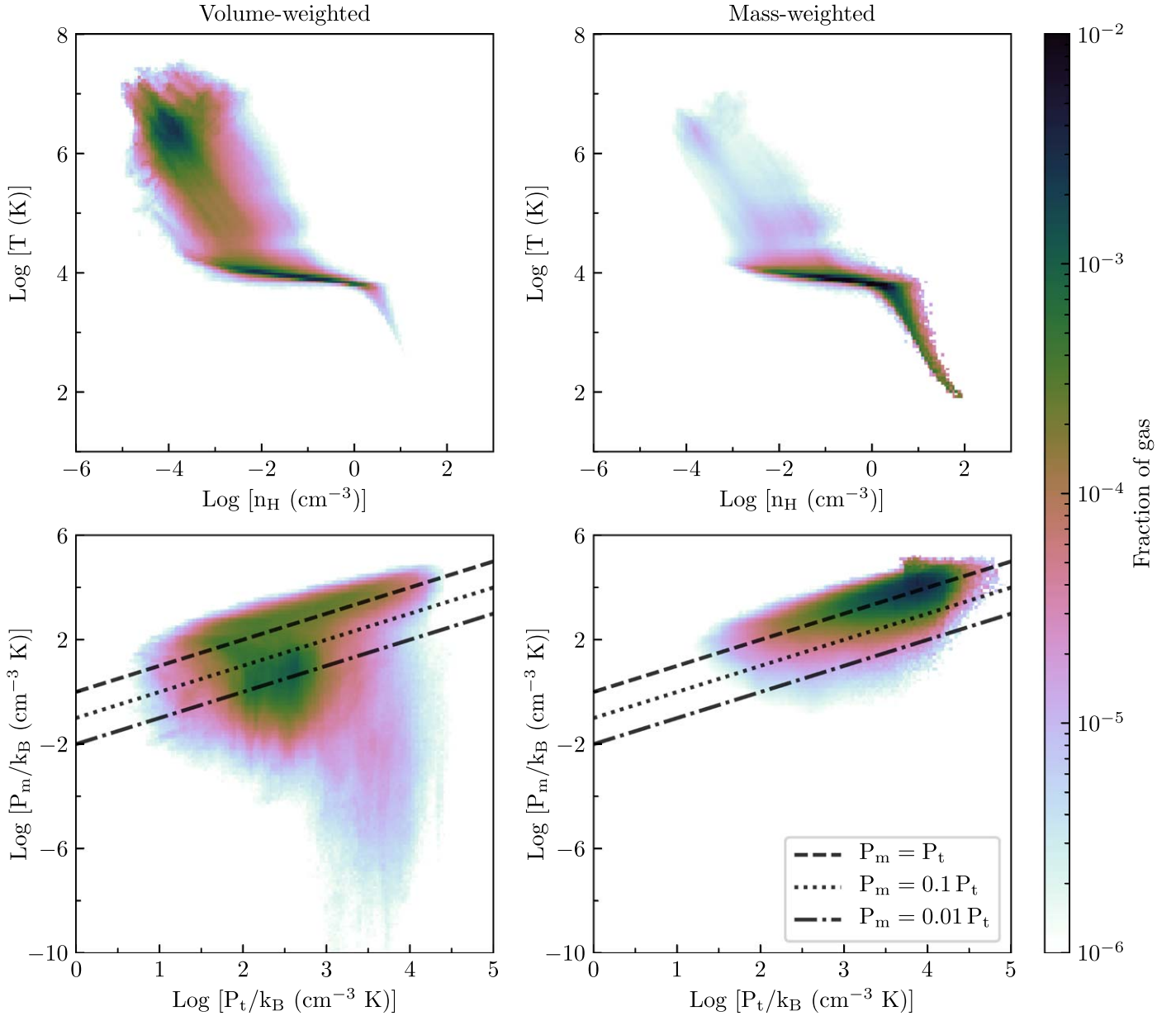


Figure 3. Time-averaged gas distribution in the density n_H and temperature T phase plane (top panels) and in the thermal pressure P_t/k_B and magnetic pressure P_m/k_B phase plane (bottom panels). The distributions are computed as a two-dimensional probability density function showing the volume (left panels) and mass (right panels) of gas within each logarithmic bin, normalized by the bin area. The dashed black lines in the bottom panels denote the thermal-magnetic pressure equipartition curve, while the dotted and dotted-dashed lines denote the relations $P_m = 0.1 P_t$ and $P_m = 0.01 P_t$, respectively.

term proportional to v_s is always negative because CRs always stream down the CR pressure gradient. The rhs terms of Equation (2) are written as the product of the particle-wave interaction coefficient and the flux evaluated in the rest frame of the fluid. This term asymptotes to zero in the absence of CR scattering (yielding $\sigma \rightarrow 0$), either because wave damping is extremely strong or because there is no wave growth.

In steady state, Equation (2) reduces to the canonical expression for F_c ,

$$F_c = \frac{4}{3} e_c (v + v_s) - \sigma^{\leftrightarrow -1} \cdot \nabla P_c, \quad (6)$$

obtained by combining Equations (2)–(5). In this limit, the CR flux can be decomposed into three components: the advective flux $F_a = 4/3 e_c v$, the streaming flux $F_s = 4/3 e_c v_s$, and the

diffusive flux $F_d = -\sigma^{\leftrightarrow -1} \cdot \nabla P_c$. In Sections 3 and 4, we analyze the contribution of each of these components to the total flux once the overall CR distribution has reached a steady state, i.e., when $\partial e_{c,\text{tot}}/\partial t \simeq \partial F_{c,\text{tot}}/\partial t \simeq 0$, where $e_{c,\text{tot}}$ and $F_{c,\text{tot}}$ are the energy and flux density integrated over the entire simulation box. In particular, we compare the three components of the CR propagation speed, i.e., gas-advection velocity v , Alfvén speed $v_{A,i}$, and diffusive speed relative to the waves, defined as

$$v_d = \frac{3}{4} \frac{|F_d|}{e_c} = -\frac{1}{4} \sigma^{\leftrightarrow -1} \cdot \frac{\nabla e_c}{e_c}. \quad (7)$$

Below, we explain how we compute some of the terms appearing in Equations (1) and (2) as well as additional explicit source and sink terms. In particular, in Sections 2.2.1 and 2.2.2

we describe how an injection of CRs from supernova explosions and collisional losses are included in the code through their respective source and sink terms, while in Section 2.2.3 we present the different approaches used to calculate the scattering coefficients σ_{\parallel} and σ_{\perp} . In Sections 2.2.4 and 2.2.5, we show how some quantities relevant for the calculation of the scattering rate are computed. Finally, in Section 2.2.6, we summarize the models of CR transport explored in this work.

2.2.1. Cosmic-Ray Injection

For a star cluster particle of mass m_{sp} and mass-weighted age t_{sp} , we calculate the rate of injected CR energy as $\dot{E}_{\text{c,sp}} = \epsilon_{\text{c}} E_{\text{SN}} \dot{N}_{\text{SN}}$, where ϵ_{c} is the fraction of supernova energy that goes into the production of CRs, $E_{\text{SN}} = 10^{51}$ erg is the energy released by an individual supernova event, and $\dot{N}_{\text{SN}} = m_{\text{sp}} \xi_{\text{SN}}(t_{\text{sp}})$ is the number of supernovae per unit time. ξ_{SN} , defined as the number of supernovae per unit time per star cluster mass measured at a given time t_{sp} , is determined from the STARBURST99 code (see Kim & Ostriker 2017).

The injection of CR energy from supernovae enters in the rhs of Equation (1) through a source term Q . We assume that the injected energy is distributed around each star cluster particle following a Gaussian profile, and, in each cell, we calculate the injected CR energy density per unit time as

$$Q = \frac{1}{2\pi\sqrt{2\pi}\sigma_{\text{inj}}^3} \sum_{\text{sp}=1}^{N_{\text{sp}}} \dot{E}_{\text{c,sp}} \cdot \exp(-r_{\text{sp}}^2/2\sigma_{\text{inj}}^2), \quad (8)$$

where the sum is taken over all the star cluster particles in the simulation box. r_{sp} is the distance between the cell center and the star particle, while σ_{inj} is the standard deviation of the distribution. We explore different values of σ_{inj} , from $2\Delta x$ to $10\Delta x$, and we find that the final CR distribution is almost independent of this choice.

In most of the CR transport models analyzed in this work, we assume that 10% of the supernova energy is converted into CR energy ($\epsilon_{\text{c}} = 0.1$, e.g., Morlino & Caprioli 2012; Ackermann et al. 2014). We point out that ϵ_{c} linearly scales with ϵ_{c} ($\partial \epsilon_{\text{c}} / \partial t \propto Q$, where Q does not depend on ϵ_{c}). Therefore, our reported results for CR energy density or pressure could be renormalized to a different fraction of the SN energy injection rate simply by multiplying by $\epsilon_{\text{c}}/0.1$ (exceptions are presented in Section 5).

In the case that the sum of other rhs terms in Equation (1) is negligible compared to the injected CR energy density, in steady state the average flux along the z -direction, $\langle F_{\text{c},z} \rangle$, can be written as $0.5\epsilon_{\text{c}} E_{\text{SN}} \langle \Sigma_{\text{SFR}} \rangle / m_{\star}$, where $m_{\star} = 95.5 M_{\odot}$ is the total mass of new stars per supernova and Σ_{SFR} is the star formation rate density. In the TIGRESS simulation analyzed in this paper, the average value of Σ_{SFR} is $\simeq 4 \times 10^{-3} M_{\odot} \text{ yr}^{-1} \text{ kpc}^{-2}$ (Kim & Ostriker 2017), which, given our assumption $\epsilon_{\text{c}} = 0.1$, corresponds to $\langle F_{\text{c},z} \rangle = 2 \times 10^{45} \text{ erg yr}^{-1} \text{ kpc}^{-2}$. We note, however, that the average flux can be reduced/increased relative to this by up to a factor of 3 due to the energy transferred to/from the gas (terms on the rhs of Equation (1)).

2.2.2. Energy Losses

CRs lose their energy due to collisional interactions with the surrounding gas. As CR energy losses are proportional to the

gas density, the dense ISM is the place where losses are expected to be more significant. Ionization of atomic and molecular hydrogen is the main mechanism responsible for energy losses of CRs with kinetic energies $E_{\text{k}} \equiv E - m_{\text{p}}c^2 \lesssim 100 \text{ MeV}$, with E the total relativistic energy, while losses due to pion production via elastic collisions with ambient atoms are dominant for CRs with kinetic energies $E_{\text{k}} \gtrsim 1 \text{ GeV}$.

Due to collisions with the ambient gas, individual CRs lose energy at a rate

$$\frac{dE}{dt} = -v_{\text{p}} L(E) n_{\text{H}} \equiv -\Lambda_{\text{coll}}(E) E n_{\text{H}}, \quad (9)$$

where $L(E)$ is the energy loss function, defined as the product of the energy lost per ionization event and the cross section of the collisional interaction (see review by Padovani et al. 2020), and v_{p} is the proton velocity,

$$v_{\text{p}} = c \sqrt{1 - \left(\frac{m_{\text{p}}c^2}{E} \right)^2}, \quad (10)$$

with m_{p} the proton mass. Considering a population of CRs with different energies, the energy lost per unit time per unit volume, Γ_{loss} , would therefore be

$$\Gamma_{\text{loss}} = -n_{\text{H}} \int \Lambda_{\text{coll}}(E) E n_{\text{c}}(E) dE_{\text{k}}, \quad (11)$$

where $n_{\text{c}}(E_{\text{k}})$ is the number of CRs per unit volume and unit kinetic energy and the integral is evaluated over the entire CR energy spectrum.

In practice, Equation (11) might be evaluated as a discrete sum over a finite number of energy bins. However, for the calculations performed in this work, we use the so-called “single bin” approximation, i.e., we assume that all CRs are characterized by a single energy E . Equation (11) then becomes

$$\Gamma_{\text{loss}} = -\Lambda_{\text{coll}}(E) n_{\text{H}} e_{\text{c}}. \quad (12)$$

As explained in Section 1, we want to analyze the transport of both CRs with kinetic energies of about 1 GeV, which dominate the CR energy budget and are therefore dynamically important for the surrounding gas, and CRs with kinetic energies of about 30 MeV, which play a fundamental role in the process of gas ionization and heating (e.g., Draine 2011). For this reason, we perform two different sets of simulations: in one set we adopt $\Lambda_{\text{coll}} = 4 \times 10^{-16} \text{ cm}^3 \text{ s}^{-1}$, representative of CRs with kinetic energies of about 1 GeV, while in the other we adopt $\Lambda_{\text{coll}} = 9 \times 10^{-16} \text{ cm}^3 \text{ s}^{-1}$, representative of CRs with kinetic energies of about 30 MeV. The value of the proton loss function at a given energy is extracted from the gray line in Figure 2 of Padovani et al. (2020), representing the loss function for a medium of pure atomic hydrogen, and multiplied by a factor of 1.21, to account for elements heavier than hydrogen. In the following, we will refer to CR protons with $E_{\text{k}} \simeq 1 \text{ GeV}$ as high-energy CRs and to CR protons with $E_{\text{k}} \simeq 30 \text{ MeV}$ as low-energy CRs.

Since collisional losses affect not only the energy density of CRs, but also their flux, we update both the rhs of Equation (1) and the rhs of Equation (2) adding the term $\Gamma_{E_{\text{c}},\text{loss}} = -\Lambda_{\text{coll}}(E) n_{\text{H}} e_{\text{c}}$ and $\Gamma_{F_{\text{c}},\text{loss}} = -\Lambda_{\text{coll}}(E) n_{\text{H}} F_{\text{c}} / v_{\text{p}}^2$, respectively.

Table 1
List of CR Transport Models

| High-energy CRs ($E_k \simeq 1 \text{ GeV}$, $\Lambda_{\text{coll}} = 4 \times 10^{-16} \text{ cm}^3 \text{ s}^{-1}$) | | | | | | |
|---|------------|------------------------|----------------------|------------|------------|------------------------|
| 1. Diffusion only, $\sigma_{\parallel} = 10^{-28} \text{ cm}^{-2} \text{ s}$, $\sigma_{\perp} = 10 \sigma_{\parallel}$, $\Lambda_{\text{coll}} = 0$ | | | | | | |
| 2. Streaming only, $ v_s = v_A $, $\Lambda_{\text{coll}} = 0$ | | | | | | |
| 3. Diffusion and streaming, $ v_s = v_A $, $\Lambda_{\text{coll}} = 0$ | | | | | | |
| $\sigma_{\parallel} \text{ (cm}^{-2} \text{ s)}$ | 10^{-27} | 10^{-28} | 10^{-28} | 10^{-28} | 10^{-29} | 10^{-30} |
| $\sigma_{\perp} \text{ (cm}^{-2} \text{ s)}$ | 10^{-26} | 10^{-27} | 10^{-28} | 10^{-29} | 10^{-28} | 10^{-29} |
| 4. Diffusion, streaming, and advection, $ v_s = v_A $ | | | | | | |
| $\sigma_{\parallel} \text{ (cm}^{-2} \text{ s)}$ | 10^{-27} | 10^{-28} | 10^{-29} | 10^{-28} | | |
| $\sigma_{\perp} \text{ (cm}^{-2} \text{ s)}$ | 10^{-26} | 10^{-27} | 10^{-28} | ... | | |
| 5. Self-consistent model, variable σ_{\parallel} , $ v_s = v_{A,i} $ | | | | | | |
| δ | -0.35 | | -0.35 | 0.1 | -0.8 | -0.8 |
| σ_{\perp} | ... | $10\sigma_{\parallel}$ | σ_{\parallel} | ... | ... | $10\sigma_{\parallel}$ |
| Low-energy CRs ($E_k = 30 \text{ MeV}$, $\Lambda_{\text{coll}} = 9 \times 10^{-16} \text{ cm}^3 \text{ s}^{-1}$) | | | | | | |
| 1. Self-consistent model, variable σ_{\parallel} , $ v_s = v_{A,i} $ | | | | | | |
| δ_{inj} | -0.8 | -0.35 | -1.0 | | | |

2.2.3. Scattering Coefficient

In Section 1, we have seen that there are two main processes responsible for CR scattering, namely “self-confinement” and “extrinsic turbulence.” In the first scenario, CRs are scattered by Alfvén waves that the CRs themselves excite, while in the second scenario CRs are scattered by the background turbulent magnetic field. The self-confinement mechanism dominates the scattering for CRs with kinetic energies lower than 100 GeV (Zweibel 2013, 2017), and it is, therefore, relevant for the range of energies we are interested to study in this paper.

In the CR transport algorithm adopted here, the degree of scattering is parametrized by the scattering coefficients σ_{\parallel} and σ_{\perp} in the CR flux equation (see Equation (2)). The most common approach that has been adopted in MHD (and HD) simulations is to assume constant values for the scattering coefficients based on empirical estimates in the Milky Way. These estimates are inferred using CR propagation models based on analytic prescriptions for the gas distribution and/or assuming spatially constant isotropic diffusion (see Section 1 and references therein). While these models are able to match many observed CR properties, they often neglect a number of factors that may be key to a full understanding of the physics behind the transport of CRs on galactic scales, especially the role of advection and local variations of the background gas properties (e.g., magnetic field structure, gas density, and ionization fraction).

In this work, we follow two different general approaches. First, in Section 3, we perform simulations with spatially constant values for the scattering coefficients. While σ_{\parallel} represents the gyro-resonant scattering rate along the local magnetic field direction, σ_{\perp} can be understood as scattering along unresolved fluctuations of the mean magnetic field. We explore a range of values for σ_{\parallel} going from 10^{-27} to $10^{-30} \text{ cm}^{-2} \text{ s}$, where $\sigma_{\parallel} \sim 10^{-28} - 10^{-29} \text{ cm}^{-2} \text{ s}$ is the scattering coefficient usually adopted for CR protons of a few GeV in simulations of Milky Way-like environments. The range of σ_{\parallel} and σ_{\perp} explored in this work is listed in Table 1 (see

Section 2.2.6). Second, in Section 4, we derive the scattering coefficient σ_{\parallel} in a self-consistent manner based on the predictions of the quasi-linear theory for the growth of Alfvén gyro-resonant waves and assuming balance between the rate of wave growth and the rate of wave damping (Kulsrud & Pearce 1969). CRs interact with Alfvén waves that they themselves drive via resonant streaming instability.

Given a distribution of CRs that is isotropic in a frame moving at drift speed v_D with respect to the gas velocity along the magnetic field, from Kulsrud (2005) the growth rate of resonant Alfvén waves in a fully ionized plasma is

$$\Gamma_{\text{stream}}(p_1) = \frac{\pi \Omega_0 m_p}{4 \rho} \left(\frac{v_D}{v_A} - 1 \right) n_1, \quad (13)$$

where

$$n_1 \equiv 4\pi p_1 \int_{p_1}^{\infty} p F(p) dp. \quad (14)$$

Here, $\Omega_0 = e|B|/(m_p c)$ is the cyclotron frequency for e the electron charge, c the speed of light, m_p the proton mass, and $F(p)$ the CR distribution function in momentum space in the streaming frame (see Section 2.2.4 for a description of how $F(p)$ is computed in the code). The momentum $p_1 = m_p \Omega_0 / k$ is the resonant value for wavenumber k . The momentum p_1 corresponds to the component along the magnetic field, i.e., $p_1 = \mathbf{p} \cdot \hat{\mathbf{B}}$ for relativistic momentum $p = [(E/c)^2 - (m_p c)^2]^{1/2}$ and $E = E_k + mc^2$ the total relativistic energy. In general, the growth rate depends on particle energy since the spectrum enters in n_1 . In Appendix A.1, we show how n_1 relates to the CR number density n_c and energy density e_c for our parameterization of the CR distribution as a broken power law (see Section 2.2.4). For a pure power-law distribution, $\Gamma_{\text{stream}}(p_1) \sim \Omega_0 n_c (p > p_1) / n_H$ with an order-unity coefficient, i.e., the growth rate at p_1 scales with the total number density of CRs with momentum exceeding p_1 .

We can also relate the CR drift velocity to the fluxes as $v_D = (3/4)(F_{c,\parallel} - F_{a,\parallel})/e_c$, which in steady state (see Equation (6)) becomes $v_D = (3/4)(F_{c,\parallel} + F_{d,\parallel})/e_c = v_A + |\hat{\mathbf{B}} \cdot \nabla P_c| / (4P_c \sigma_{\parallel})$, with $F_{c,\parallel}$, $F_{a,\parallel}$, $F_{s,\parallel}$ and $F_{d,\parallel}$ the components of the total, advective, streaming, and diffusive flux along the magnetic field direction, and $\hat{\mathbf{B}}$ the magnetic field direction. Substituting in for v_D/v_A in Equation (13), the growth rate can be rewritten as

$$\Gamma_{\text{stream}}(p_1) = \frac{\pi^2 \Omega_0 m_p v_A}{4 B^2} \frac{|\hat{\mathbf{B}} \cdot \nabla P_c|}{\sigma_{\parallel} P_c} n_i. \quad (15)$$

The growth of Alfvén waves is hampered by damping mechanisms that cause those waves to dissipate. Here, we consider two main damping mechanisms: ion-neutral damping and nonlinear Landau damping.

The ion-neutral damping arises from friction between ions and neutrals in partially ionized gas. In this regime, Alfvén waves propagate only in the ions (nearly decoupled from neutrals) at the scales where wave-particle interaction takes place, since the collision frequency is typically much lower than the frequency of resonant waves. Alfvén waves in the ions are damped by collisions with neutrals at a rate (Kulsrud & Pearce 1969)

$$\Gamma_{\text{damp,in}} = \frac{1}{2} \frac{n_n m_n}{m_n + m_i} \langle \sigma v \rangle_{\text{in}}, \quad (16)$$

where n_n is the neutral number density, m_n is the mean mass of neutrals, m_i is the mean mass of ions (see Section 2.2.5 for the definition of neutral and ion mass and density), and $\langle \sigma v \rangle_{\text{in}}$ is the rate coefficient for ion-neutral collisions ($\sim 3 \times 10^{-9} \text{ cm}^3 \text{ s}^{-1}$, Draine 2011, Table 2.1).

Equation (13) is derived under the assumption that the background plasma is fully ionized. In the decoupled regime, the resonant Alfvén waves propagate at the ion Alfvén speed $v_{A,i} = B / \sqrt{4\pi \rho_i}$ —with ρ_i the ion mass density—rather than at the Alfvén speed $v_A = B / \sqrt{4\pi \rho}$, which applies either for $\rho \approx \rho_i$ (nearly fully ionized plasma) or for wavelengths at which the neutrals and ions are well coupled (see Plotnikov et al. 2021). In Equation (15), this can be accounted for with the substitution $v_A \rightarrow v_{A,i}$ to obtain $\Gamma_{\text{stream},i}$.

In the simplest version of the self-confinement scenario (Kulsrud & Pearce 1969; Kulsrud & Cesarsky 1971), it is assumed that wave growth and damping balance. Setting $\Gamma_{\text{stream},i} = \Gamma_{\text{damp,in}}$, the parallel scattering coefficient becomes

$$\sigma_{\parallel,\text{in}}(p_1) = \frac{\pi}{8} \frac{|\hat{\mathbf{B}} \cdot \nabla P_c|}{v_{A,i} P_c} \frac{\Omega_0}{n_n \langle \sigma v \rangle_{\text{in}}} \frac{m_p(m_n + m_i)}{m_i m_n} \frac{n_i}{n_i}. \quad (17)$$

The nonlinear Landau damping occurs when thermal ions have a Landau resonance with the beat wave formed by the interaction of two resonant Alfvén waves. The rate of nonlinear Landau damping is (Kulsrud 2005)

$$\Gamma_{\text{damp,nll}} = 0.3 \Omega \frac{v_{ti}}{c} \left(\frac{\delta B}{B} \right)^2, \quad (18)$$

where $\Omega = \Omega_0/\gamma(p_1)$ is the relativistic cyclotron frequency, with γ the Lorentz factor of CRs with momentum p_1 , v_{ti} is the ion thermal velocity (which we set equal to the gas sound speed), and $\delta B/B$ is the magnetic field fluctuation at the resonant scale. The quasi-linear theory predicts that the scattering rate is $\nu_s \sim \Omega(\delta B/B)^2$, while the scattering coefficient is

$\sigma_{\parallel} \sim \nu_s/v_p^2 \sim \Omega(\delta B/B)^2/v_p^2$ so that $\Gamma_{\text{damp,nll}} = 0.3(v_{ti}v_p^2/c)\sigma_{\parallel}$. Again assuming $\Gamma_{\text{stream}} = \Gamma_{\text{damp,nll}}$ for self-confinement, the parallel scattering coefficient becomes

$$\sigma_{\parallel,\text{nll}}(p_1) = \sqrt{\frac{\pi}{16} \frac{|\hat{\mathbf{B}} \cdot \nabla P_c|}{v_{A,i} P_c} \frac{\Omega_0 c}{0.3 v_{ti} v_p^2} \frac{m_p n_i}{m_i n_i}} \quad (19)$$

for nonlinear Landau damping.⁴ In the code, the local scattering coefficient is set by the damping mechanism that contributes the most to the Alfvén wave dissipation, i.e., σ_{\parallel} is equal to the minimum between the results of Equations (17) and (19). In Sections 4 and 5, we see that the ion-neutral damping mechanism dominates in the cooler and denser portions of the ISM, while the nonlinear Landau damping mechanism dominates in the hot and ionized phase of the gas.

2.2.4. CR Spectrum

In this section, we explain how we compute the distribution function of CR protons in momentum space, $F(p)$, relevant for the calculation of n_i in Equations (17) and (19). $F(p)$ is related to the number of CRs per unit volume and unit energy $n_c(E_k)$ as

$$F(p) = \frac{n_c(E_k)}{4\pi p^2} \frac{dE_k}{dp}. \quad (20)$$

In turn, $n_c(E_k)$ can be written as a function of the CR energy flux spectrum $j(E_k)$ as $n_c(E_k) = j(E_k)/v_p$. Here, we adopt the spectrum of CR protons proposed by Padovani et al. (2018) for the solar neighborhood,

$$j(E_k) = C \frac{E_k^{\delta}}{(E_k + E_t)^{2.7+\delta}} \text{ eV}^{-1} \text{ cm}^{-2} \text{ s}^{-1}, \quad (21)$$

where the adopted value for E_t is 650 MeV. The high-energy slope of this function, -2.7 , is well determined (e.g., Aguilar et al. 2014, 2015), while the low-energy slope δ is uncertain. A simple extrapolation of the Voyager 1 data down energies of 1 MeV predicts $\delta \approx 0.1$ (Cummings et al. 2016). However, a slope $\delta \approx 0.1$ fails to reproduce the CR ionization rate measured in local diffuse clouds ($n \approx 100 \text{ cm}^{-3}$, $T \approx 100 \text{ K}$) from H_3^+ emission (e.g., Indriolo & McCall 2012). Padovani et al. (2018) found that the low-energy slope required to reproduce the observed CR ionization rate at the edges of molecular clouds must rise toward low energy, with best fit $\delta = -0.8$. The authors however noticed that the average Galactic value of δ is likely to lie between -0.8 and 0.1 . In fact, δ is expected to increase (spectral flattening) within clouds as low-energy CRs preferentially lose energy ionizing and heating the ambient gas (see Section 2.2.2).

In this work, we adopt two different approaches for the calculation of $j(E_k)$ (Equation (21)) depending on whether we model the propagation of high-energy or low-energy CRs. In simulations of high-energy CRs, we adopt a spatially constant value of δ . We explore three values of the low-energy slope: $\delta = -0.35$ (default simulation), $\delta = 0.1$ and $\delta = -0.8$ (the results of these two cases are discussed in Appendix A.3). The normalization factor C is evaluated in each cell depending on the local value of the CR energy density. Since CRs with kinetic energies of about 1 GeV dominate the total energy

⁴ Strictly speaking, the wave energy growth rate is $2\Gamma_{\text{stream},i}$ while the theoretical scattering rate coefficient is $(\pi/8)(\delta B/B)^2\Omega$; taken together this would introduce a factor 0.8 inside the square root of Equation (19).

budget of CRs with kinetic energy above E_t , we can assume $e_c \simeq \int_{E_t}^{\infty} E n_c(E_k) dE_k$ for the high-energy CRs. In any given cell, C can then be calculated as

$$C = e_c(\text{GeV}) \left(\int_{E_t}^{\infty} \frac{E E_k^{\delta}}{v_p (E_k + E_t)^{2.7+\delta}} dE_k \right)^{-1} \frac{\text{eV}^{1.7}}{\text{cm}^2 \text{ s}} \quad (22)$$

where $e_c(\text{GeV})$ is from the high-energy CRs. The value of C is then used in normalizing the spectrum which is input to the scattering rate (Section 2.2.3) as well as the CR ionization rate (Section 2.2.5) calculations.

In simulations of low-energy CRs, we instead calculate the local value of δ based on the local energy density of both low-energy and high-energy CRs. For the low-energy CRs, $e_c = E n_c(E_k) dE_k$ represents the energy density of CRs with kinetic energy between $E_k - dE_k/2$ and $E_k + dE_k/2$, where we adopt $E_k = 30 \text{ MeV}$ and an energy width bin dE_k equal to 1 MeV . We then calculate the low-energy slope of the CR spectrum as

$$\delta = \frac{\log(e_c(\text{MeV})/C) + \log(v_p(E_k + E_t)^{2.7}) - \log(EdE_k)}{\log(E_k) - \log(E_k + E_t)}, \quad (23)$$

where now $e_c(\text{MeV})$, v_p , E_k , and E refer to the low-energy CRs, while the value of C is taken from the corresponding default simulation of high-energy CRs. This is possible because the kinetic energy is mainly contained in the higher-energy portion of the spectrum in Equation (21), so for a given total CR energy input rate (taken as 10% of the SN energy) the normalization constant C is nearly independent of δ for the range we consider (see also Appendix A.3, where we show that the pressure of high-energy CRs is almost independent of the adopted δ). Since C is proportional to $e_c(\text{GeV})$, δ from Equation (23) depends on the relative energy deposited in high- and low-energy CRs, but not on the absolute level. For the high-energy CRs, we assume that a fraction $\epsilon_c(\text{GeV}) = 0.1$ of the SN energy input rate is deposited at $E_k \gtrsim E_t$. For the low-energy CRs, we must make an assumption about the CR injection spectrum in order to calculate the corresponding energy deposition fraction $\epsilon_c(\text{MeV})$. We explore three different values of the low-energy slope of the injection spectrum: $\delta_{\text{inj}} = 0.1$, $\delta_{\text{inj}} = -0.35$, and $\delta_{\text{inj}} = -0.8$. For these values of δ , the fractions of CRs with $E_k = 30 \pm 1/2 \text{ MeV}$ are 0.005, 0.02, and 0.07, corresponding to $\epsilon_c = 5 \times 10^{-4}$, 2×10^{-3} , and 7×10^{-3} , respectively.

2.2.5. CR Ionization Rate and Ionization Fraction

In this section, we explain how the ion and neutral densities are calculated in Equations (17) and (19). The ion number density is calculated as $n_i = x_i n_H$, where the hydrogen number density n_H is an output of the MHD simulation and x_i is the ion fraction. For gas at $T > 2 \times 10^4 \text{ K}$, the ion fraction is calculated from the values tabulated by Sutherland & Dopita (1993), while, for gas at $T \leq 2 \times 10^4 \text{ K}$, the ion fraction is calculated as (Draine 2011)

$$x_i = x_M + \frac{\sqrt{(\beta + \chi + x_M)^2 + 4\beta} - (\beta + \chi + x_M)}{2}, \quad (24)$$

where $x_M = 1.68 \times 10^{-4}$ is adopted for the ion fraction of species with ionization potential $< 13.6 \text{ eV}$ (the largest

contributor from the metals is C^+), while the second term on the rhs is the fraction of ionized hydrogen x_{H^+} . In Equation (24), β is defined as $\zeta_H/(\alpha_{\text{rr}} n_H)$, where ζ_H is the CR ionization rate per hydrogen atom and $\alpha_{\text{rr}} = 1.42 \times 10^{-12} \text{ cm}^3 \text{ s}^{-1}$ is adopted for the rate coefficient for radiative recombination of ionized hydrogen, while χ is defined as $\alpha_{\text{gr}}/\alpha_{\text{rr}}$, where $\alpha_{\text{gr}} = 2.83 \times 10^{-14} \text{ cm}^3 \text{ s}^{-1}$ is adopted for the grain-assisted recombination rate coefficient. Note that we have chosen this value to be representative of the cold neutral medium ($T \simeq 100 \text{ K}$, $n_H \simeq 10\text{--}100 \text{ cm}^{-3}$), rather than the warm neutral medium ($T \simeq 10^4 \text{ K}$, $n_H \simeq 0.1\text{--}1 \text{ cm}^{-3}$), where α_{gr} is actually smaller. The reason is that $x_i \approx \beta^{1/2}$ at the typical densities of the warm medium ($4\beta \gg \beta + \chi + x_M$) and changing the value of α_{gr} marginally affects the value of x_i . For warm gas (most of the neutrals), the ion fraction can be approximated as $x_i = 0.008(\zeta_H/10^{-16} \text{ s}^{-1})^{1/2} (n_H/1 \text{ cm}^{-3})^{-1/2}$. Given the CR ionization rate per hydrogen atom of $\sim 3 \times 10^{-16} \text{ s}^{-1}$ measured in local diffuse clouds, the ion number density at the average densities of the local ISM ($n_H \simeq 0.1\text{--}1 \text{ cm}^{-3}$) is $\sim 0.02 \text{ cm}^{-3}$.

The CR ionization rate per atomic hydrogen ζ_H accounts for ionization due to CR nuclei and secondary electrons produced by primary ionization events. It can be approximated as $\zeta_H = 1.5 \zeta_c$, where ζ_c is the ionization rate per atomic hydrogen due to nuclei only (primary ionization rate), and it is calculated as

$$\zeta_c = \int_{E_{k,\text{min}}}^{E_{k,\text{max}}} \frac{v_p n_c(E_k) L_{\text{ion}}(E_k)}{\epsilon} dE_k \quad (25)$$

(Padovani et al. 2020). In Equation (25), $n_c(E_k)$ is computed as explained in Section 2.2.4, $\epsilon \approx 50 \text{ eV}$ is the average energy lost by each proton per ionization event, and $L_{\text{ion}}(E_k)$ is the proton loss function due to hydrogen ionization. We adopt the power-law approximation proposed by Silsbee & Ivlev (2019),

$$L_{\text{ion}}(E_k) = L_0 \left(\frac{E_k}{E_0} \right)^{-0.82} \quad (26)$$

where $L_0 = 1.27 \times 10^{-15} \text{ eV cm}^2$ and $E_0 = 1 \text{ MeV}$. Equation (26) holds over the range of kinetic energies between 10^5 and 10^9 eV , where CR losses due to ionization of atomic and molecular hydrogen are relevant (see also Section 2.2.2). The minimum kinetic energy for CRs, $E_{k,\text{min}}$, is unknown since Voyager 1 does not probe energies below 1 MeV . We therefore assume, following Padovani et al. (2018), that the lower limit of the integral in Equation (25) is $E_{k,\text{min}} = 10^5 \text{ eV}$. The upper limit is $E_{k,\text{max}} = 10^9 \text{ eV}$ as Coulomb losses are negligible above that density. In Appendix A.2, we show how the value of ζ_c depends on the low-energy slope of the spectrum, on the CR pressure through the normalization factor C (Equation (22)), and on the choice of $E_{k,\text{min}}$.

From n_i , we compute the ion mass density—relevant for the calculation of the ion Alfvén speed—as $\rho_i = \mu_i m_p n_i$, where μ_i is the ion mean molecular weight. For gas at $T > 2 \times 10^4 \text{ K}$, we adopt $\mu_i \approx 2 \mu$, where μ is the total mean molecular weight tabulated by Sutherland & Dopita (1993) as a function of temperature. For gas at $T \leq 2 \times 10^4 \text{ K}$, we calculate the ion mean molecular weight as $\mu_i = (x_{H^+} m_p + x_M m_M)/(x_i m_p)$, with $m_M \approx 12 m_p$ the mean ion mass of species with ionization potential larger than 13.6 eV .

Finally, in Equation (17), we calculate the neutral mass density as $n_n m_n = \rho - \rho_i$ and the mean ion mass as $m_i = \mu_i m_p$. Moreover, we assume that the mean neutral mass is $m_n \approx 2 m_p$ for gas at $T < 100$ K, where hydrogen is predominantly in molecular form, and $m_n \approx m_p$ for gas at $100 \leq T \leq 2 \times 10^4$ K, where hydrogen is predominantly in atomic form.

2.2.6. Summary of CR Transport Models

The algorithm for CR propagation presented in the previous sections is applied to the 10 snapshots selected from the TIGRESS simulation modeling the solar neighborhood environment (see Section 2.1). The energy and flux densities of CRs are evolved through space and time according to Equations (1) and (2), while the background MHD quantities are frozen in time. We stop and analyze the simulations once the overall distributions of CR energy density has reached a steady state, i.e., $(e_{c,\text{tot}}(t) - e_{c,\text{tot}}(t - 0.1 \text{ Myr}))/e_{c,\text{tot}}(t) < 10^{-6}$, with $e_{c,\text{tot}} = \int_{\text{Vol}} e_c dx^3$.

Our goal is to explore the predictions of different models of CR propagation, and we therefore consider several different models in which the parameters are treated differently. The models explored in this work are listed in Table 1. We separately investigate the propagation of high-energy ($E_k \sim 1$ GeV) and low-energy ($E_k = 30$ MeV) CRs adopting two different values of Λ_{coll} , the rate coefficient for collisional losses (see Equation (12)).

First, in Section 3, we consider high-energy CRs with spatially constant scattering coefficients. We consider propagation models with (1) only diffusion ($v_s = 0$, $v = 0$), (2) only streaming ($\sigma_{\parallel} = \sigma_{\perp} \gg 1$, $v = 0$), (3) both diffusion and streaming but no advection ($v = 0$), and (4) diffusion, streaming and advection. For the latter two cases we explore different combinations of spatially constant σ_{\parallel} and σ_{\perp} . Note that we set the streaming speed to the magnitude of the ideal Alfvén speed, $v_A = B/(4\pi\rho)^{1/2}$ for ρ the total gas density, and, in models without advection, we neglect the effect of collisional losses setting $\Lambda_{\text{coll}} = 0$.

Second, in Section 4 we consider physically motivated models (including diffusion, streaming, and advection) in which σ_{\parallel} varies based on the local CR pressure and gas properties (see Section 2.2.3 for details). In these models, the streaming velocity is set to $v_{A,i}$. Calculating the scattering coefficient in a self-consistent manner requires making an assumption for the low-energy slope of the CR energy spectrum δ (see Equation (21)), since σ_{\parallel} depends on the ionization fraction x_i , and x_i in warm/cold gas depends on the ionization rate produced by low-energy CRs. Here, we consider three different values of δ . Also, we model the propagation of CRs either in the absence (we set $\sigma_{\perp} \gg 1$) or in the presence of diffusion perpendicular to the magnetic field direction. For the latter case, we consider either isotropic ($\sigma_{\perp} = \sigma_{\parallel}$) or anisotropic diffusion (with $\sigma_{\perp} = 10 \sigma_{\parallel}$).

For low-energy CRs, in Section 5 we investigate propagation models with a variable scattering coefficient only. All models include streaming, advection, and diffusion parallel to the magnetic field direction. We explore the effect of three different assumptions for the low-energy slope of the CR injection spectrum δ_{inj} , which entails different fractions of supernova energy going into the production of low-energy CRs.

3. High-energy Cosmic Rays: Models with a Spatially Constant Scattering Coefficient

In this section, we consider CR transport models in which the scattering rate coefficient is set to a spatially constant value. This is helpful for gauging the effects of different values of σ , and also useful for making contact with the many works in the literature that have adopted spatially constant σ .

3.1. Models Without Advection

We start with the analysis of CR transport models neglecting advection. These models have been applied to a single TIGRESS snapshot ($t = 286$ Myr, Figure 2) only, rather than to the full set of 10 snapshots. Figure 4 shows the distribution on the grid of CR pressure predicted by the different models. The first two panels on the left refer to the models assuming pure diffusion and pure streaming, respectively. In the model with pure diffusion, σ_{\parallel} is chosen to be $10^{-28} \text{ cm}^2 \text{ s}$. The other models include both diffusion and streaming and are performed with different values of σ_{\parallel} , from 10^{-27} to $10^{-30} \text{ cm}^2 \text{ s}$. An immediate conclusion from Figure 4 is that in the absence of advection, regardless of the CR propagation model, the distribution of CR pressure is very smooth across the grid compared to the distribution of the magnetohydrodynamical quantities shown in Figure 2. The model with pure streaming and, to a lesser extent, the models with relatively high scattering coefficient, predict a higher CR pressure in proximity to CR injection sites (see the distribution of young star clusters in Figure 2). Streaming of CRs is quite ineffective within expanding supernova bubbles, where the magnetic field is chaotic and the Alfvén speed is extremely low ($\ll 1 \text{ km s}^{-1}$). For the same reason, a steady state is not reached before 1 Gyr in the simulation accounting for CR streaming only. Diffusion is clearly crucial for spreading CRs beyond their injection sites. Also evident from Figure 4, and consistent with expectations, is that the CR pressure decreases at higher σ_{\parallel} since diffusion becomes more and more effective ($F_d \propto 1/\sigma$).

In Figure 5, we show the horizontally averaged vertical profiles of P_c predicted by the four models with both streaming and diffusion. As noted above, the value of P_c at a given z is lower for smaller σ_{\parallel} . In the midplane, P_c becomes comparable with the other relevant pressures if we assume $\sigma_{\parallel} = 10^{-30} \text{ cm}^2 \text{ s}$. We point out that this value is lower than the range $\sigma \sim 10^{-29} - 10^{-28} \text{ cm}^2 \text{ s}$ predicted by traditional studies of CR propagation in our Galaxy that neglect advection and do not employ detailed magnetic field structure (see Section 6.3 for a discussion). The comparison with the horizontally averaged profiles of thermal, kinetic, and magnetic pressure (dotted, dashed, and dotted-dashed gray lines, respectively) confirms that the distribution of CR pressure is extremely uniform compared to that of the other pressures, even in cases where streaming is the dominant mechanism of CR transport (i.e., $\sigma_{\parallel} > 10^{-29} \text{ cm}^2 \text{ s}$; see Section 3.1.1). As pointed out in Section 2.1, in much of the volume, magnetic field lines are mostly tangled. With random changes of the magnetic field orientation, streaming transport resembles diffusion on scales larger than the coherence length of the field line, and contributes to producing a uniform distribution of CRs across space. We note, however, that there is a greater degree of large-scale field alignment near the midplane—where the preferential horizontal field helps confine CRs—and at high-latitude

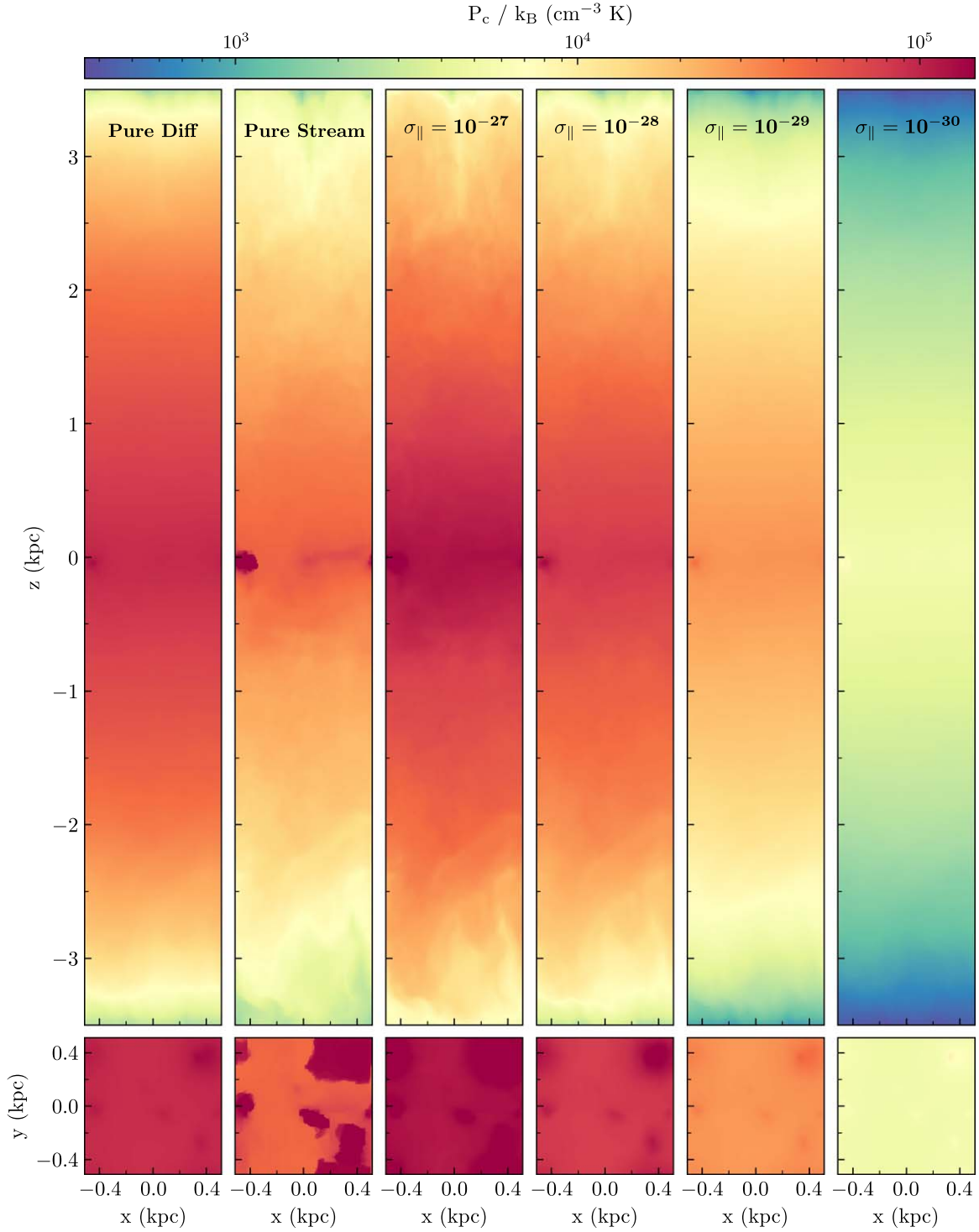


Figure 4. Distribution on the grid of the CR pressure for different models of CR transport neglecting advection, showing $y = 0$ slices of P_c . The first two panels on the left are models with pure CR diffusion ($\sigma_{\parallel} = 10^{-28} \text{ cm}^2 \text{ s}$) and pure CR streaming, respectively. The remaining panels are for models with both CR diffusion and streaming. These adopt different values of σ_{\parallel} (from left to right: $10^{-27} \text{ cm}^2 \text{ s}$, $10^{-28} \text{ cm}^2 \text{ s}$, $10^{-29} \text{ cm}^2 \text{ s}$, and $10^{-30} \text{ cm}^2 \text{ s}$) and σ_{\perp} ($\sigma_{\perp} = 10 \sigma_{\parallel}$). The $t = 286 \text{ Myr}$ TIGRESS snapshot is used (see Figure 2).

regions where the enhanced vertical alignment does help transport CRs out of the disk.

3.1.1. Streaming versus Diffusive Transport

We investigate the relative importance of streaming and diffusive transport, evaluating the ratio of Alfvén speed and

diffusive speed (Equation (7)) across the simulation box. The left panel of Figure 6 shows the distribution on the grid of $|v_A|/|v_d|$ in models with different choices of σ_{\parallel} , from 10^{-28} to $10^{-30} \text{ cm}^2 \text{ s}$. Streaming transport largely dominates in the model with $\sigma_{\parallel} = 10^{-28} \text{ cm}^2 \text{ s}$, except for a few regions characterized by low Alfvén speeds ($v_A \ll 1 \text{ km s}^{-1}$, see Figure 2). A visual comparison between the Alfvén speed

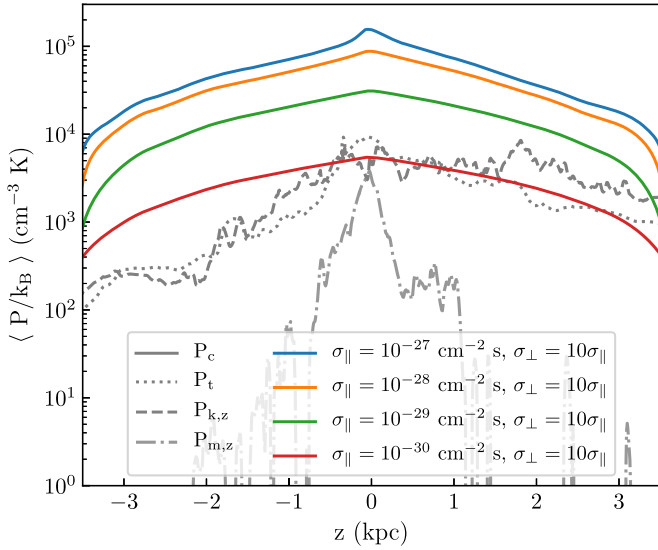


Figure 5. Horizontally averaged CR pressure P_c as a function of z for different models of CR transport including both diffusion and streaming (solid lines). Each color corresponds to a given value of σ_{\parallel} , from $10^{-27} \text{ cm}^{-2} \text{ s}$ (blue line) to $10^{-30} \text{ cm}^{-2} \text{ s}$ (red line). All these models assume $\sigma_{\perp} = 10 \sigma_{\parallel}$. The gray lines show the horizontally averaged profiles of thermal pressure P_t (dotted line), vertical kinetic pressure $P_{k,z}$ (dashed line), and vertical magnetic stress $P_{m,z}$ (dotted-dashed line). These profiles are obtained by postprocessing the TIGRESS snapshot at $t = 286 \text{ Myr}$.

snapshot and the density and temperature snapshots in Figure 2 shows that low Alfvén speeds occur within expanding supernova bubbles and at the base of the hot winds generated by their blowout. The ratio $|v_A|/|v_d|$ is closer to unity in the model with $\sigma_{\parallel} = 10^{-29} \text{ cm}^{-2} \text{ s}$, indicating an equivalent contribution of streaming and diffusion, except for the regions with $v_A \ll 1 \text{ km s}^{-1}$, where diffusion is more important. Instead, diffusive transport is largely dominant in the model with $\sigma_{\parallel} = 10^{-30} \text{ cm}^{-2} \text{ s}$.

The right panel of Figure 6 shows the volume-weighted (red histograms) and mass-weighted (blue histograms) probability distributions of $|v_A|/|v_d|$ across the simulation domain for the three different choices of σ_{\parallel} . In all models, the mass-weighted distributions present more pronounced peaks and less extended tails toward low values of $|v_A|/|v_d|$ compared to the volume-weighted distributions. This is because the regions at higher density, which contribute the most to the mass budget (see Figure 3), are characterized by larger Alfvén speeds ($v_A \gtrsim 10 \text{ km s}^{-1}$ for $n_H > 0.1 \text{ cm}^{-3}$, see Figure 2) and, therefore, significant CR streaming. The difference between the volume-weighted and mass-weighted distribution is reflected in slightly different median values, with the volume-weighted median systematically lower than the mass-weighted median. Regardless of the weight chosen to analyze the distribution of $|v_A|/|v_d|$, the evidence discussed in the previous paragraph is confirmed: streaming is the dominant transport mechanism in the model assuming $\sigma_{\parallel} = 10^{-28} \text{ cm}^{-2} \text{ s}$, while diffusion is the dominant mechanism in the model assuming $\sigma_{\parallel} = 10^{-30} \text{ cm}^{-2} \text{ s}$.

3.1.2. Diffusion Perpendicular to the Magnetic Field Lines

So far, we have focused on the effect on CR transport produced by different choices of σ_{\parallel} . Since all the analyzed models assume $\sigma_{\perp} = 10 \sigma_{\parallel}$, an increase/decrease of σ_{\parallel} has

always implied an increase/decrease of σ_{\perp} by the same factor. In this section, we investigate the extent to which diffusion perpendicular to the magnetic field contributes to the overall CR propagation by comparing the results of models with different ratios of σ_{\parallel} and σ_{\perp} . The left panel of Figure 7 displays the average vertical profile of CR pressure for models with the same $\sigma_{\perp} = 10^{-28} \text{ cm}^{-2} \text{ s}$ and different σ_{\parallel} , ranging from $10^{-27} \text{ cm}^{-2} \text{ s}$ to $10^{-29} \text{ cm}^{-2} \text{ s}$. In contrast, the middle panel shows the average vertical profile of CR pressure for models with the same $\sigma_{\parallel} = 10^{-28} \text{ cm}^{-2} \text{ s}$ and different σ_{\perp} . As expected, CR pressure P_c increases with σ_{\parallel} when σ_{\perp} is constant, while P_c increases with σ_{\perp} when σ_{\parallel} is constant, but the sensitivity to changes is not the same. In both panels, the purple lines represent the same model with $\sigma_{\perp} = \sigma_{\parallel} = 10^{-28} \text{ cm}^{-2} \text{ s}$ with either an increase/decrease of σ_{\parallel} (red/green line on left) or increase/decrease of σ_{\perp} (orange/cyan line on the right). Evidently, varying σ_{\perp} rather than σ_{\parallel} entails a greater change in CR pressure. For example, in the midplane, P_c decreases by a factor ~ 3 when σ_{\perp} decreases from $10^{-28} \text{ cm}^{-2} \text{ s}$ to $10^{-29} \text{ cm}^{-2} \text{ s}$, while it decreases by a factor ~ 1.3 when σ_{\parallel} decreases from 10^{-28} to $10^{-29} \text{ cm}^{-2} \text{ s}$.

In the right panel of Figure 7, we analyze the ratio of the diffusive flux perpendicular to the magnetic field, $F_{d,\perp}$, to the total CR flux, as a function of $\cos \theta = |\hat{B} \cdot \nabla P_c|/|\nabla P_c|$. The analysis is performed for the model adopting $\sigma_{\perp} = \sigma_{\parallel} = 10^{-28} \text{ cm}^{-2} \text{ s}$. The average ratio $|F_{d,\perp}|/|F_c|$ increases when the magnetic pressure gradient is not aligned with the magnetic field, and becomes larger than 0.5 for $\cos \theta \lesssim 0.25$. This behavior indicates that diffusion perpendicular to the magnetic field direction is the main propagation mechanism in regions where the magnetic field is nearly perpendicular to the CR pressure gradient. Diffusion perpendicular to the magnetic field direction is therefore crucial for the propagation of CRs that would be otherwise confined, either by a tangled magnetic field (at high altitude) or by a mostly horizontal magnetic field (near the midplane). This result explains the significant variation of CR pressure led by variations of σ_{\perp} .

3.2. Models Including Advection

In this section, we present the predictions of CR propagation models with spatially constant scattering including advective transport, in addition to streaming and diffusion. Figure 8 shows the distribution on the grid of CR pressure for three different choices of σ_{\parallel} , from 10^{-27} to $10^{-29} \text{ cm}^{-2} \text{ s}$, for a single MHD snapshot at $t = 286 \text{ Myr}$. Except for the case with a low scattering coefficient ($\sigma_{\parallel} = 10^{-29} \text{ cm}^{-2} \text{ s}$), where the high diffusivity produces a relatively uniform CR pressure across the grid, the distribution of CRs closely follows the gas distribution (see Figure 2). CRs accumulate in regions with high density and low temperature, where the relatively low gas velocities ($v < 50 \text{ km s}^{-1}$) do not foster their removal. By contrast, CRs in regions with hot and fast-moving winds ($v \gg 100 \text{ km s}^{-1}$) are rapidly advected away from the midplane. Figure 2 shows that the velocity streamlines of the hot winds channel gas out of the disk, allowing CRs coupled to the hot phase gas to escape through these “chimneys.” The importance of advective transport is particularly evident in the model with a high scattering coefficient ($\sigma_{\parallel} = 10^{-27} \text{ cm}^{-2} \text{ s}$), where CR diffusion is negligible (see Sections 3.1.1 and 3.2.1). The correlation between CRs and the density/temperature distribution in the left panel of Figure 8 contrasts strongly with the very smooth CR pressure profile in the third

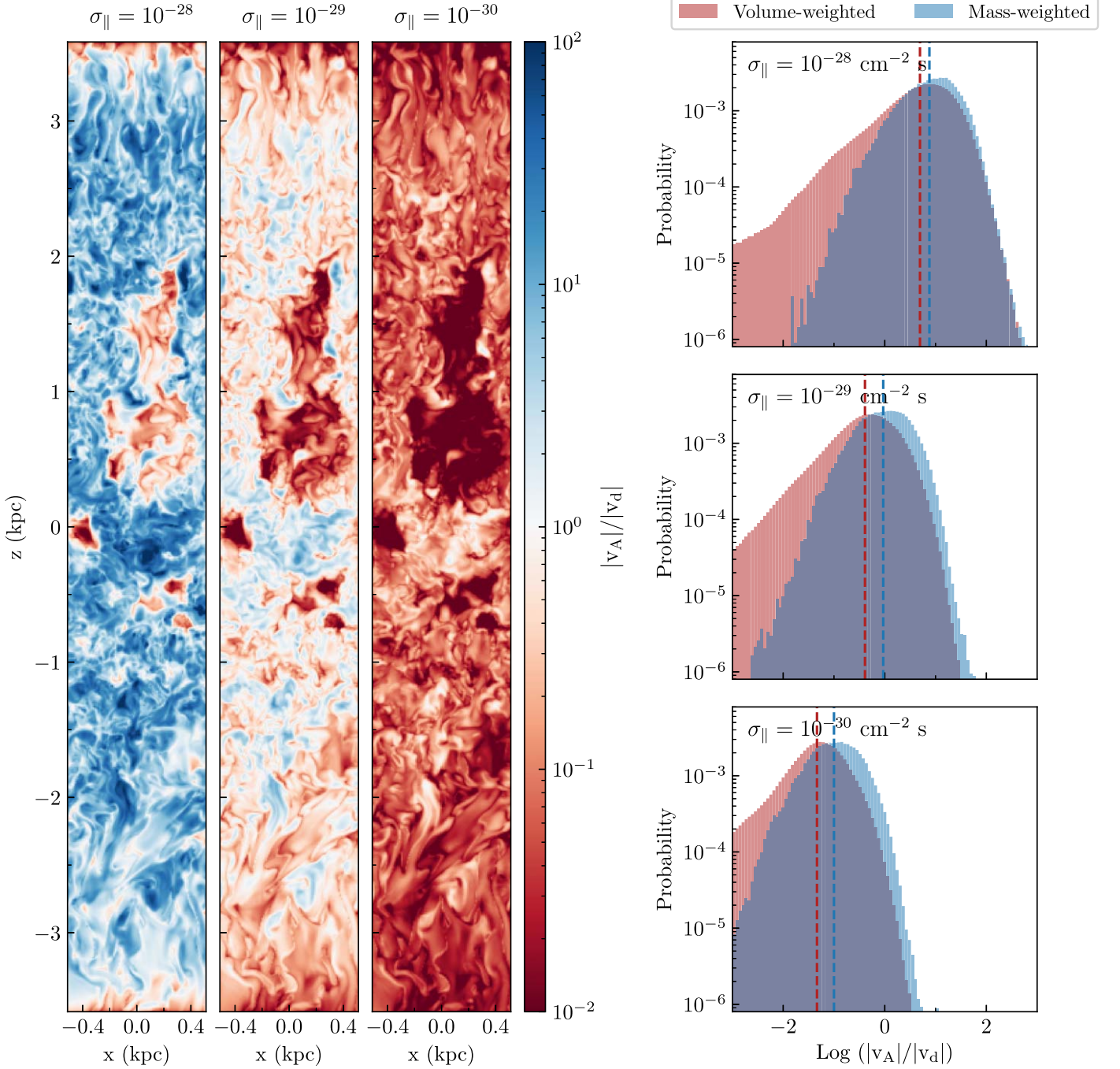


Figure 6. Analysis of the relative contribution of streaming and diffusion to the overall CR propagation in the absence of advection. Left side: distribution on the grid of the ratio between Alfvén speed $|v_A|$ and diffusive speed $|v_d|$ in models with $\sigma_{\parallel} = 10^{-28} \text{ cm}^{-2} \text{ s}$ (left panel), $\sigma_{\parallel} = 10^{-29} \text{ cm}^{-2} \text{ s}$ (middle panel) and $\sigma_{\parallel} = 10^{-30} \text{ cm}^{-2} \text{ s}$ (right panel). Right side: volume-weighted (red histograms) and mass-weighted (blue histograms) probability distributions of $|v_A|/|v_d|$ for $\sigma_{\parallel} = 10^{-28} \text{ cm}^{-2} \text{ s}$ (top panel), $\sigma_{\parallel} = 10^{-29} \text{ cm}^{-2} \text{ s}$ (middle panel) and $\sigma_{\parallel} = 10^{-30} \text{ cm}^{-2} \text{ s}$ (bottom panel). The red and blue dashed lines indicate the median values of the volume-weighted and mass-weighted distributions, respectively.

panel of Figure 4, and more generally the smooth CR distributions in all the models without advection.

Figure 9 shows horizontally averaged vertical profiles of P_c as in Figure 5, but now for models with advection. The colored solid lines refer to models including collisional losses, while the corresponding dotted–dotted–dashed lines refer to models not accounting for collisional losses. Unlike the results shown in Figure 5, now the CR pressure profile significantly changes with σ_{\parallel} . For $\sigma_{\parallel} = 10^{-29} \text{ cm}^{-2} \text{ s}$, the profile is relatively flat and

does not show significant variations as a function of z , while for $\sigma_{\parallel} = 10^{-27} \text{ cm}^{-2} \text{ s}$, the CR pressure peaks in the midplane, where the gas velocity is relatively low and mainly oriented in xy -direction, and decreases at higher z . Comparing profiles in Figure 9 with Figure 5 for each σ , we see that the CR pressure in the disk decreases by about one order of magnitude when advection is included. As a consequence, the midplane CR pressure is comparable to the other relevant pressure for $10^{-29} \lesssim \sigma_{\parallel} \lesssim 10^{-28} \text{ cm}^{-2} \text{ s}$, while this is true only for a much

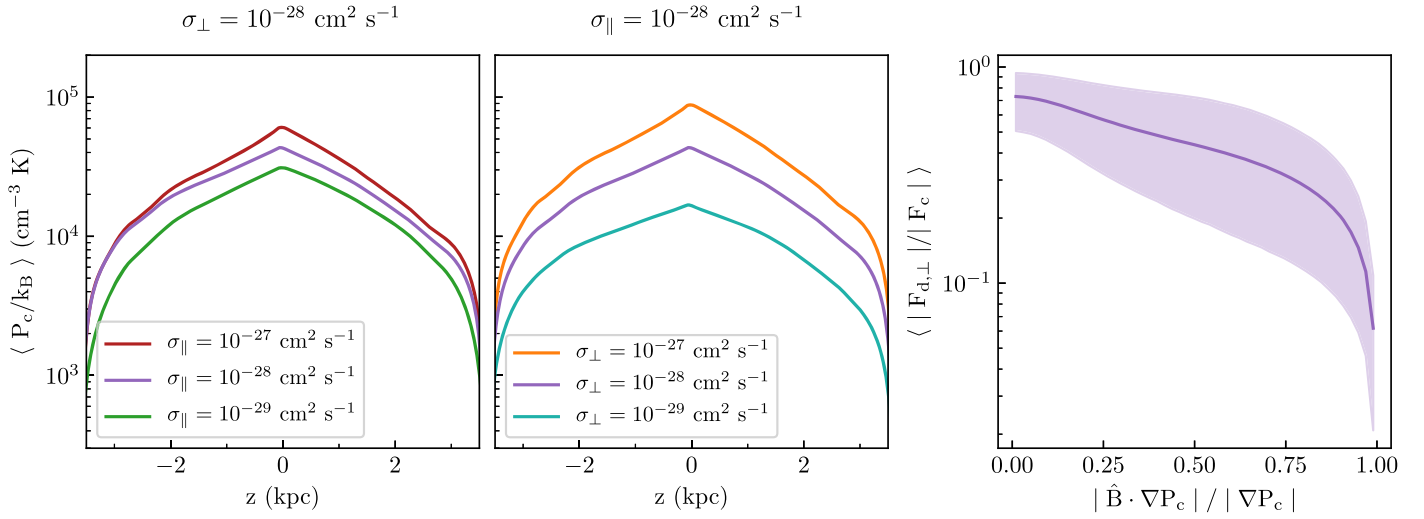


Figure 7. Analysis of the relative effects of diffusion parallel and perpendicular to the magnetic field direction in models neglecting CR advection. Left panel: horizontally averaged CR pressure as a function of z for models with same $\sigma_{\perp} = 10^{-28} \text{ cm}^2 \text{ s}^{-1}$ and different σ_{\parallel} , from $10^{-27} \text{ cm}^2 \text{ s}^{-1}$ (red line) to $10^{-29} \text{ cm}^2 \text{ s}^{-1}$ (green line). Middle panel: same as in the left panel, but for models with the same $\sigma_{\parallel} = 10^{-28} \text{ cm}^2 \text{ s}^{-1}$ and σ_{\perp} ranging from $10^{-27} \text{ cm}^2 \text{ s}^{-1}$ (orange line) to $10^{-29} \text{ cm}^2 \text{ s}^{-1}$ (cyan line). Right panel: average ratio of $|F_{d,\perp}|$ to $|F_c|$ as a function of the cosine of the angle between the magnetic field direction and the CR pressure gradient direction, for the model with $\sigma_{\parallel} = \sigma_{\perp} = 10^{-28} \text{ cm}^2 \text{ s}^{-1}$ (purple line in the three panels). The shaded area covers the 16th and 84th percentiles of the distribution.

lower scattering coefficient ($\sigma_{\parallel} = 10^{-30} \text{ cm}^2 \text{ s}^{-1}$) in the absence of advection. The results of Figures 8 and 9 demonstrate that accounting for the advection of CRs by galactic winds is crucial in models of CR propagation, since CRs can easily escape from the galactic disk by flowing out along with the hot fast-moving gas. We further explore this point in Section 3.2.1.

Another important result of Figure 9 comes from the comparison of the vertical profiles of CR pressure obtained in the absence and in the presence of CR collisional losses. The change of CR pressure is almost negligible in models with $\sigma_{\parallel} \leq 10^{-28} \text{ cm}^2 \text{ s}^{-1}$, while it is more significant in the model assuming $\sigma_{\parallel} = 10^{-27} \text{ cm}^2 \text{ s}^{-1}$, especially in the midplane, where P_c decreases by $\sim 25\%$ when CR losses are included. We note that the rate of CR energy losses is proportional to the gas density (see Equation (12)). Therefore, CR losses are more effective for relatively high scattering coefficients, as this traps CRs in denser portions of the ISM for a longer time.

3.2.1. Importance of Advective Transport

We have seen that advection by fast-moving gas plays a key role in rapidly carrying CRs far from their injection sites. In Figure 10, we further quantify the relative contribution of advection compared to streaming and diffusion. The left side of Figure 10 displays the distribution on a grid of the ratio between the advection speed and the sum of the Alfvén and diffusive speeds, $|v|/(|v_A| + |v_d|)$. We show results for models with three different σ_{\parallel} for the same $t = 286 \text{ Myr}$ MHD snapshot. For all values of σ_{\parallel} , advection completely dominates in the hot gas, and is marginally more important than diffusion and streaming in much of the remaining volume. In higher-density gas, which fills much of the midplane and is present in clumps/filaments at high latitude, advection is subdominant. For the higher-density regions, the importance of advective transport decreases at lower σ_{\parallel} as diffusion becomes more and more effective.

The right panel of Figure 10 shows the volume-weighted (red histograms) and mass-weighted (blue histograms) probability distributions of $|v|/|v_{\text{eff}}|$, $|v_A|/|v_{\text{eff}}|$, and $|v_d|/|v_{\text{eff}}|$, with

$|v_{\text{eff}}| = |3/4 F_c/e_c|$ the effective CR propagation speed, for the three choices of the scattering coefficient.⁵ When volume-weighted, transport of CRs is mostly through advection with the ambient gas, as on average the gas velocity dominates over the other relevant velocities, regardless of the value of σ_{\parallel} . However, when weighted by gas mass, the distribution shifts to lower values of $|v|/|v_t|$. As previously noted, streaming and diffusion are more important in regions characterized by higher densities. In the model with $\sigma_{\parallel} = 10^{-29} \text{ cm}^2 \text{ s}^{-1}$, the mass-weighted median of the diffusive speed distribution is higher than the medians of the advective and streaming speed distributions. Thus, when the CR scattering coefficient is relatively low, diffusion is the main transport mechanism of CR propagation in higher-density regions. For $\sigma_{\parallel} = 10^{-29} \text{ cm}^2 \text{ s}^{-1}$, diffusion dominates over streaming even in terms of volume. For the higher values $\sigma_{\parallel} = 10^{-28}$ and $10^{-27} \text{ cm}^2 \text{ s}^{-1}$, however, both the mass-weighted median diffusion speed and streaming speed are lower than the advection speed.

In Section 3.1.1, for models without advection, we have seen that a low scattering coefficient ($\sigma_{\parallel} < 10^{-29} \text{ cm}^2 \text{ s}^{-1}$) is required for diffusion to be dominant over streaming. However, once advection is included, the median diffusion speed exceeds the median streaming speed even for $\sigma_{\parallel} \sim 10^{-28} \text{ cm}^2 \text{ s}^{-1}$. It is striking that once advection is once included, it becomes the main CR transport mechanism in many high-latitude regions that would otherwise be dominated by streaming (compare Figure 10 with Figure 6) and where CRs would be trapped by tangled magnetic fields. For the same reason, the diffusive flux in the direction perpendicular to the magnetic field, which is crucial for the propagation of CRs when advection is neglected (see Section 3.1.2), plays a minor role in the presence of

⁵ We note that the moduli of individual propagation speed components, v , v_A , and v_d , can exceed the modulus of the effective propagation speed v_{eff} . This is mostly due to vector cancellation in v_{eff} , but also to the presence of zones out of steady-state equilibrium, for which Equation (6) does not hold. In fact, even if the overall system is approximately in equilibrium, there are always a number of cells far from such conditions. These cells are usually characterized by $\sigma_{\text{tot},\parallel} \approx 0$ (either because the magnetic field is nearly perpendicular to the CR pressure gradient, or because of very low scattering coefficients). In this case, the rhs of Equation (2) approaches zero.

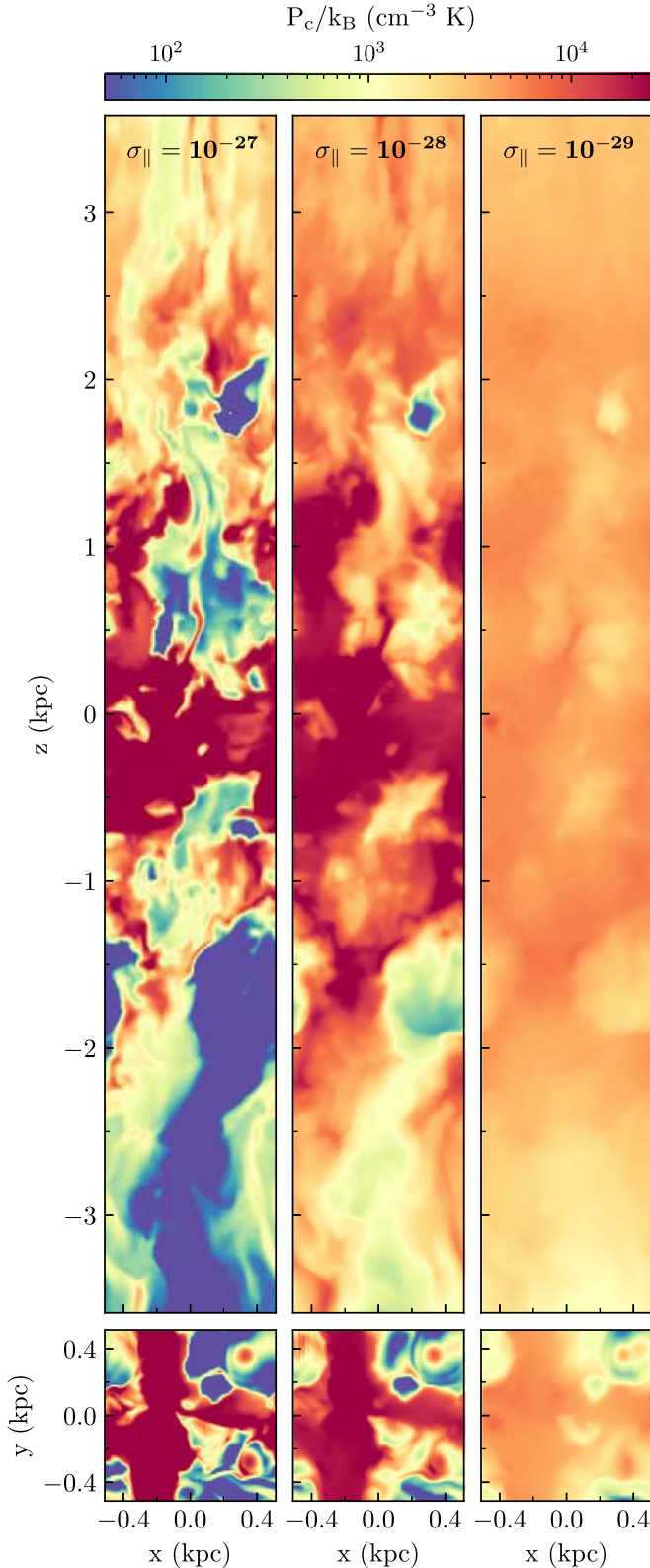


Figure 8. Distribution on the grid of CR pressure for different models of CR transport including advection, showing $y=0$ slices of P_c . While all these models assume spatially constant scattering, they adopt different values of the scattering coefficient: $\sigma_{\parallel} = 10^{-27} \text{ cm}^{-2} \text{ s}$ (left panel), $\sigma_{\parallel} = 10^{-28} \text{ cm}^{-2} \text{ s}$ (middle panel), and $\sigma_{\parallel} = 10^{-29} \text{ cm}^{-2} \text{ s}$ (right panel). As in Figure 4, the $t = 286 \text{ Myr}$ TIGRESS snapshot is used (see Figure 2).

advection. For example, in the model with $\sigma_{\parallel} = 10^{-28} \text{ cm}^{-2} \text{ s}$, if we suppress perpendicular diffusion entirely when advection

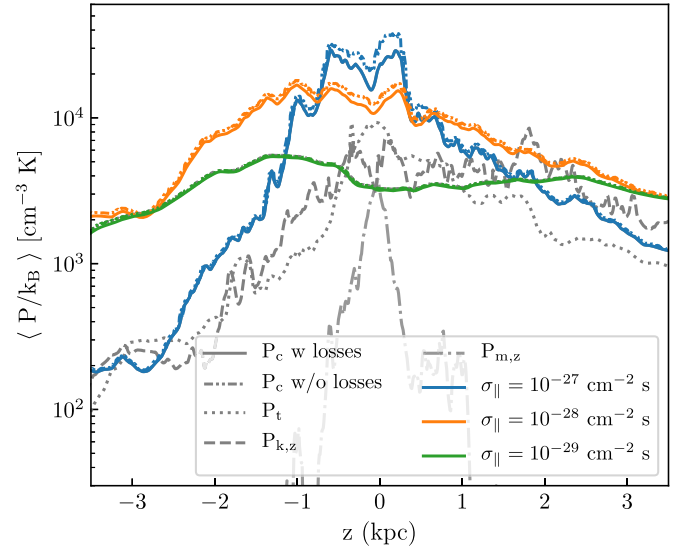


Figure 9. Horizontally averaged CR pressure P_c as a function of z for different models of CR transport including diffusion, streaming, and advection, for the same $t = 286 \text{ Myr}$ snapshot as Figure 5. Different colors correspond to different σ_{\parallel} : $10^{-27} \text{ cm}^{-2} \text{ s}$ (blue), $10^{-28} \text{ cm}^{-2} \text{ s}$ (orange), and $10^{-29} \text{ cm}^{-2} \text{ s}$ (green). The dotted-dotted-dashed lines show models neglecting CR collisional losses, while the solid lines are for models that include losses. The gray lines show the horizontally averaged vertical profiles of thermal pressure P_t (dotted), vertical kinetic pressure $P_{k,z}$ (dashed), and vertical magnetic stress $P_{m,z}$ (dotted-dashed) from the MHD snapshot.

is turned on, it leads to less than a factor of 2 variation of CR pressure near the midplane. In contrast, for the analogous case without advection, variations of σ_{\perp} lead to much more significant variations of CR pressure (see Figure 7).

3.2.2. Time-averaged Results

In Sections 3.1 and 3.2, we have analyzed results from a single TIGRESS snapshot. Here we use 10 postprocessed TIGRESS snapshots to investigate the temporally averaged CR distribution in models including all the relevant mechanisms of CR transport, i.e., diffusion, streaming, and advection. As shown by Vijayan et al. (2020), the gas properties are in a statistically steady state when averaged over several star formation cycles. Therefore, averaging the CR pressure at different times (over $t = 200\text{--}550 \text{ Myr}$), we are able to study mean trends.

Figure 11 shows the horizontally and temporally averaged profiles of CR pressure, thermal pressure, vertical kinetic pressure, and vertical magnetic stress as a function of z for models of CR propagation with different σ_{\parallel} . As highlighted in the discussion of Figure 9, the CR pressure profile becomes flatter and smoother for a low scattering rate since CRs escape from the midplane more easily and what would otherwise be inhomogeneities are erased by strong diffusion. In the midplane, the CR pressure is comparable to the thermal and vertical kinetic pressures for $\sigma_{\parallel} \lesssim 10^{-29} \text{ cm}^{-2} \text{ s}$. For a higher scattering coefficient ($\sigma_{\parallel} \gtrsim 10^{-29} \text{ cm}^{-2} \text{ s}$), the midplane CR pressure is above equipartition. We note that the value of σ_{\parallel} required to obtain pressure equipartition is slightly higher for the snapshot analyzed in Figure 9. That snapshot is representative of an outflow-dominated period, when advection by fast-moving winds is particularly effective at removing CRs from the disk.

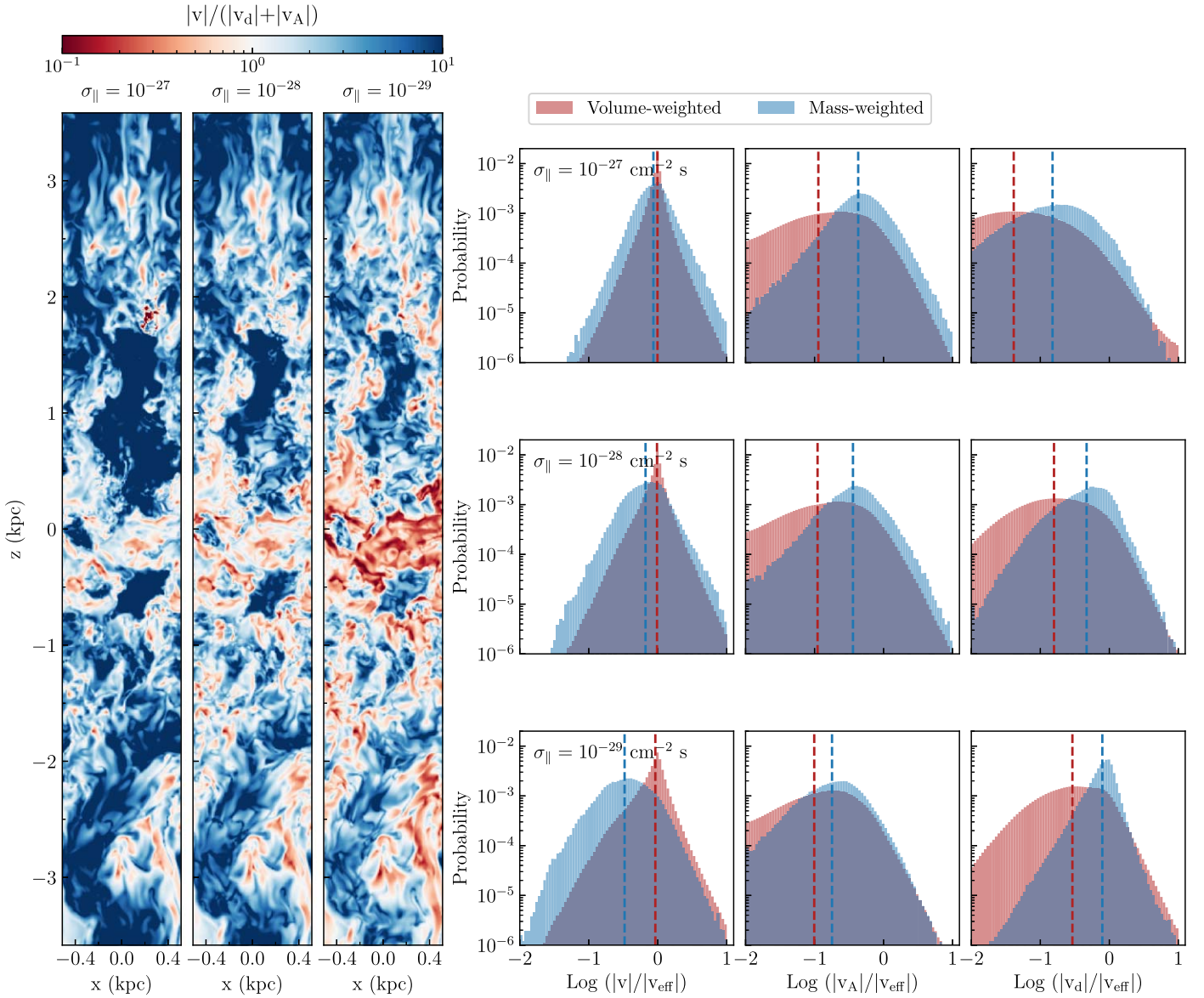


Figure 10. Analysis of the relative contribution of streaming, diffusion, and advection to the propagation of CRs in models assuming spatially constant scattering. Left side: distribution on the grid of the ratio between the gas speed v and the sum of the Alfvén and diffusive speeds $|v_A| + |v_d|$ for models with $\sigma_{\parallel} = 10^{-27} \text{ cm}^{-2} \text{ s}$ (left panel), $\sigma_{\parallel} = 10^{-28} \text{ cm}^{-2} \text{ s}$ (middle panel), and $\sigma_{\parallel} = 10^{-29} \text{ cm}^{-2} \text{ s}$ (right panel). Right side: each column shows the volume-weighted (red histograms) and mass-weighted (blue histograms) probability distribution of the ratio of $|v|$ (left column), $|v_A|$ (middle column), and $|v_d|$ (right column) relative to $|v_{\text{eff}}| \equiv |3/4 F_c/e_c|$ (an effective CR transport speed). Each row displays results for a model with given σ_{\parallel} , from $10^{-27} \text{ cm}^{-2} \text{ s}$ (top) to 10^{-29} cm^{-2} (bottom). The red and blue dashed lines indicate the median values of the volume-weighted and mass-weighted distributions, respectively. The analysis is for the $t = 286 \text{ Myr}$ TIGRESS snapshot.

We point out that for all cases, the CR scale height ($\gtrsim 1 \text{ kpc}$) is larger than the scale height of thermal and kinetic pressure ($\sim 300\text{--}400 \text{ pc}$, Kim & Ostriker 2017; Vijayan et al. 2020). This suggests that in conditions typical of our solar neighborhood, the force exerted by CRs on the gas ($\propto \partial P_c / \partial z$) is less important to supporting the vertical weight of the galactic disk than the thermal and kinetic forces, especially if $\sigma_{\parallel} < 10^{-28} \text{ cm}^{-2} \text{ s}$. At high latitudes, however, the CR force dominates over the other forces, which suggests that CRs may be important in accelerating galactic winds from the extraplanar corona/fountain region.

Finally, for each transport model, we have calculated the time-averaged individual sink/source energy terms. These consist of integrals over the whole simulation domain of the terms on the rhs of Equation (1) ($\mathbf{v}_s \cdot \nabla P_c$ and $\mathbf{v} \cdot \nabla P_c$ in steady state), as well as the integral of $\Lambda_{\text{coll}}(E)n_{\text{H}}e_c$. The average CR

energy injected per unit time is the same for all propagation models, equal to $1.8 \times 10^{38} \text{ erg s}^{-1}$. The rates of collisional and streaming energy losses and the rate of work exchange with the gas decrease in absolute value as σ_{\parallel} decreases. In all cases, we find that the $\mathbf{v} \cdot \nabla P_c$ energy exchange term is positive, i.e., on average the gas is doing work on the CR population. Detailed examination of the simulations shows that the largest contributions to the work term come from the midplane region, at interfaces where hot gas (superbubbles) is expanding at high velocity into warm/cold gas where CR densities are high. Relative to the input, for $\sigma_{\parallel} = 10^{-27} \text{ cm}^{-2} \text{ s}$ we find the collisional loss is 0.68, the streaming loss is 2.1, and the gain from the gas is 2.1. For $\sigma_{\parallel} = 10^{-28} \text{ cm}^{-2} \text{ s}$, the relative collisional loss is 0.37, the streaming loss is 1.2, and the gain from the gas is 1.8. For $\sigma_{\parallel} = 10^{-29} \text{ cm}^{-2} \text{ s}$, the relative

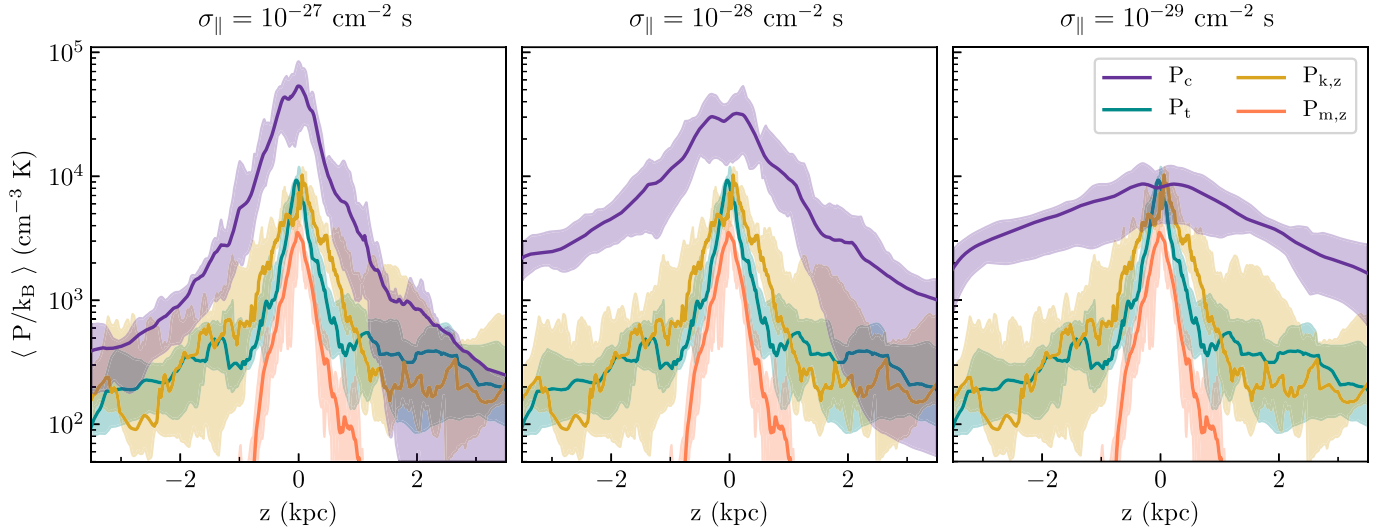


Figure 11. Horizontally and temporally averaged vertical profiles of CR pressure P_c (purple), thermal pressure P_t (cyan), kinetic pressure $P_{k,z}$ (yellow), and magnetic stress $P_{m,z}$ (orange) in models including advection and assuming spatially constant scattering. From left to right, panels show results from models with $\sigma_{\parallel} = 10^{-27}$, 10^{-28} , and $10^{-29} \text{ cm}^{-2} \text{ s}$. The shaded area covers the 16th and 84th percentiles from the temporal distribution.

collisional loss is 0.078, the streaming loss is 0.13, and the gain from the gas is 0.72.

Depending on the adopted value of σ_{\parallel} , different models have different CR grammage. The grammage gives a measure of the column of gas traversed by CRs during their propagation, defined for an individual particle as $X = \int \rho v_p dt = \int \rho v_p dE / \dot{E} = \int \rho v_p dE / (n_H \Lambda_{\text{coll}}(E) E) \approx (\mu_H m_p v_p / \Lambda_{\text{coll}}(E)) \times \Delta E / E$, with $\mu_H = 1.4$. Averaging over particles, $\Delta E / E$ is the mean fractional energy loss suffered by an individual particle from collisions, which is related to the collisional energy loss rate \dot{E}_{loss} and energy injection rate \dot{E}_{inj} over the whole domain by $\Delta E / E \approx \dot{E}_{\text{loss}} / \dot{E}_{\text{inj}}$. The grammage can then be calculated as

$$X = \mu_H m_p v_p \frac{\int d^3x n_H e_c}{\dot{E}_{\text{inj}}}, \quad (27)$$

where \dot{E}_{loss} is obtained by integrating $\Lambda_{\text{coll}}(E) n_H e_c$ over the domain. Clearly, the grammage increases if the CR energy density is concentrated near the midplane where the gas density is high. We find $X \sim 103 \text{ g cm}^{-2}$ for $\sigma_{\parallel} = 10^{-27} \text{ cm}^{-2} \text{ s}$, $X \sim 60 \text{ g cm}^{-2}$ for $\sigma_{\parallel} = 10^{-28} \text{ cm}^{-2} \text{ s}$, and $X \sim 12 \text{ g cm}^{-2}$ for $\sigma_{\parallel} = 10^{-29} \text{ cm}^{-2} \text{ s}$. We note that the grammage obtained assuming $\sigma_{\parallel} = 10^{-29} \text{ cm}^{-2} \text{ s}$ is in good agreement with the CR grammage measured at the Earth ($\sim 10 \text{ g cm}^{-2}$, e.g., Hanasz et al. 2021).

3.3. CR Pressure versus Gas Density in the Absence and in the Presence of Advection

We conclude our study of constant- σ models by analyzing how the CR pressure varies with the local gas density. In the left panel of Figure 12, we show the mean value of P_c as a function of n_H from models either including (solid lines) or neglecting (dashed lines) advection, based on the $t = 286 \text{ Myr}$ snapshot. We compare results obtained for $\sigma_{\parallel} = 10^{-27}$, 10^{-28} , and $10^{-29} \text{ cm}^{-2} \text{ s}$. As highlighted in Section 3.2, at given σ_{\parallel} the mean CR pressure decreases when advection is included. Advection makes the most difference when the scattering coefficient is relatively high ($\sigma_{\parallel} \simeq 10^{-28} - 10^{-27} \text{ cm}^{-2} \text{ s}$). In these cases, when advection is included the mean value of P_c

rapidly decreases for $n_H \lesssim 0.1 \text{ cm}^{-3}$. This is because the low-density regions generally consist of gas heated and accelerated to high velocity by SN shocks, and the high-velocity flows remove CRs efficiently.

The right panel of Figure 12 shows the temporally averaged mean of P_c as a function of n_H . Only models including advection are considered here. In all models, the average value of P_c flattens at sufficiently high densities where diffusion of CRs dominates over advection (see Figure 10). As noted above, the higher the scattering coefficient the stronger the correlation between CR pressure and gas density. In the model with $\sigma_{\parallel} = 10^{-27} \text{ cm}^{-2} \text{ s}$, the average value of P_c rapidly increases with n_H up to $n_H \sim 1 \text{ cm}^{-3}$, since CRs are strongly confined within the midplane and advection is increasingly ineffective in the high-density regions where velocities are relatively low. The correlation between P_c and n_H weakens at lower σ_{\parallel} since diffusion is more and more effective in smoothing out CR inhomogeneities and allowing CRs to leave the midplane region where they are deposited. Moreover, the increasing effectiveness of diffusion results in a lower scatter of P_c around its mean value.

4. High-energy Cosmic Rays: Models with Variable Scattering Coefficient

In this section, we investigate the distribution of CRs when we adopt a spatially varying σ , computed under the assumption that CRs are scattered by streaming-driven Alfvén waves (the self-confinement scenario), as described in Section 2.2.3. The value of σ_{\parallel} varies across the simulation box depending on the local properties of CRs and thermal gas, and we use the ion Alfvén speed $v_{A,i}$ (rather than v_A) in the CR energy and momentum equations (Equations (1) and (2)) and the computation of the scattering rates (Equations (17) and (19)). As we shall show, in the higher-density gas where gas velocities are low and advection is ineffective, $v_{A,i}/v_A = x_i^{-1/2}$ can exceed 10 since $x_i \lesssim 10^{-2}$. An accurate estimate of the ionization fraction (which depends on the low-energy CRs) is therefore important for proper computation of CR transport in the neutral gas, which comprises most of the mass in the ISM.

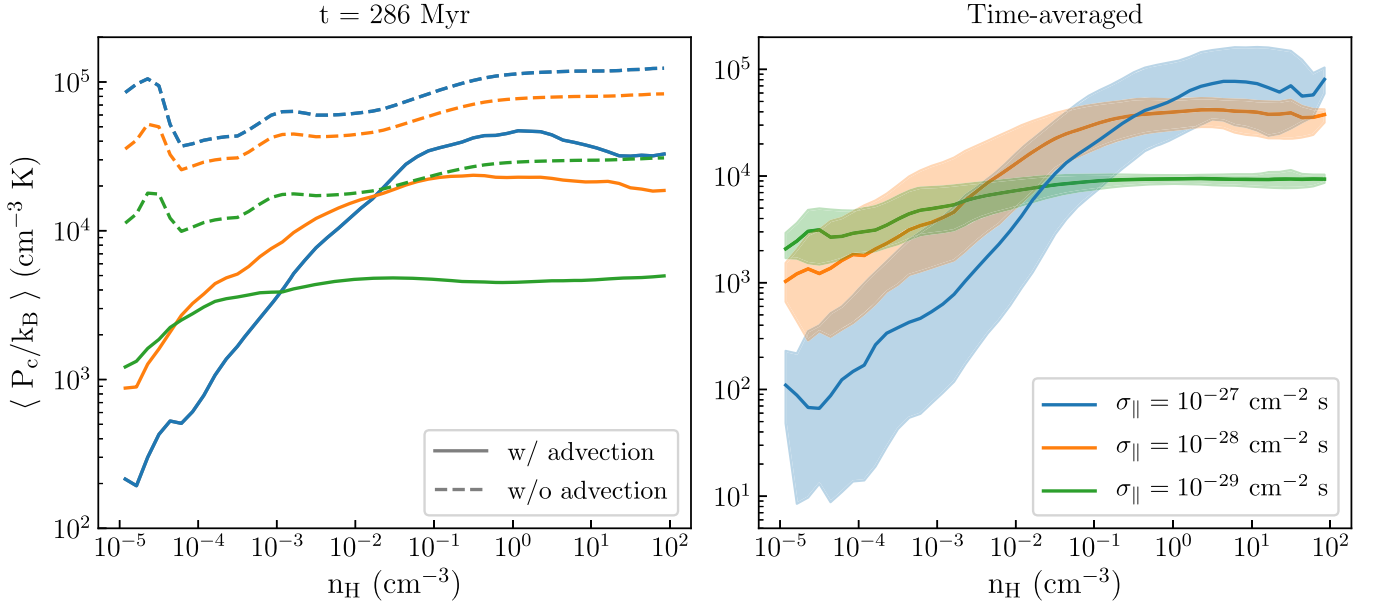


Figure 12. Mean CR pressure P_c as a function of hydrogen density n_H in models with spatially constant scattering coefficient: $\sigma_{\parallel} = 10^{-27} \text{ cm}^{-2} \text{ s}$ (blue lines), $\sigma_{\parallel} = 10^{-28} \text{ cm}^{-2} \text{ s}$ (orange lines), and $\sigma_{\parallel} = 10^{-29} \text{ cm}^{-2} \text{ s}$ (green lines). Left panel: comparison between models neglecting advection (dashed lines) and models including advection (solid lines) for a single snapshot at $t = 286 \text{ Myr}$. Right panel: temporally averaged results for models including advection. The shaded region covers the 16th and 84th percentiles from the temporal distribution.

To enable comparison with the models adopting constant scattering coefficient (Section 3.2), we first discuss the results of the self-consistent model assuming anisotropic diffusion and $\sigma_{\perp} = 10 \sigma_{\parallel}$. For the same snapshot shown in Figure 2, Figure 13 shows the distribution on the grid of some MHD quantities relevant for the self-consistent calculation: ion fraction x_i , ion density n_i , and ion Alfvén speed $v_{A,i}$, as well as the computed scattering coefficient σ_{\parallel} and P_c . The ion fraction (see Section 2.2.5 and Equation (24)) is $x_i \simeq 1$ in regions with densities $n_H \lesssim 10^{-2} \text{ cm}^{-3}$, meaning that gas is mostly ionized in those regions. In the midplane and in a few high-density filaments/clouds at higher latitudes, $x_i < 0.1$. The ion density is given by the product of the ion fraction and the hydrogen density. Therefore, $n_i \approx n_H$ ($n_i \ll n_H$) for $n_H \lesssim 10^{-2} \text{ cm}^{-3}$ ($n_H \gtrsim 0.1 \text{ cm}^{-3}$). The scattering coefficient distribution closely follows the distribution of these three MHD quantities, since it is inversely proportional to the ion Alfvén speed and to the ion density (see Equations (17) and (19)). In particular, σ_{\parallel} is relatively high ($\simeq 10^{-28} \text{ cm}^{-2} \text{ s}$) in low-density regions ($n_H < 10^{-2} \text{ cm}^{-3}$) and quite low ($\ll 10^{-29} \text{ cm}^{-2} \text{ s}$) in higher-density regions ($n_H > 10^{-1} \text{ cm}^{-3}$). Intermediate-density regions at the interface between neutral and ionized gas are characterized by the highest values of σ_{\parallel} ($\gtrsim 10^{-28} \text{ cm}^{-2} \text{ s}$).

4.1. Scattering Rate Coefficient and Vertical Profiles

We now turn to results based on ten postprocessed snapshots. The left panel of Figure 14 quantitatively analyzes the variation of σ_{\parallel} with density n_H , showing its temporally averaged median value. The dashed and dotted lines respectively show σ_{\parallel} assuming only nonlinear Landau damping (Equation (19)), and only ion-neutral damping (Equation (17)). Nonlinear Landau damping dominates at low density, where the gas is well ionized. The resulting scattering coefficient has a weak explicit dependence on the hydrogen density, $\sigma_{\parallel} = \sigma_{\parallel, \text{NLL}} \propto (v_{A,i} n_i)^{-1/2} \propto n_H^{-1/4}$. Rather than decreasing

with n_H , however, $\sigma_{\parallel, \text{NLL}}$ in Figure 14 slowly increases, which we attribute to the increase of the CR pressure gradient in higher-density gas with $\sigma_{\parallel, \text{NLL}} \propto (\hat{\mathbf{B}} \cdot \nabla P_c)^{1/2}$. Indeed, as pointed out in Section 3.2, advection of CRs is particularly effective in the fast-moving low-density gas, thus selectively reducing the CR pressure in these regions. Above $n_H \sim 10^{-2} \text{ cm}^{-3}$, gas becomes mostly neutral and ion-neutral damping becomes stronger than nonlinear Landau damping, so that $\sigma_{\parallel} = \sigma_{\parallel, \text{IN}}$. In this case, the scattering coefficient decreases with increasing the gas density, $\sigma_{\parallel, \text{IN}} \propto (v_{A,i} n_i n_n)^{-1} \propto n_H^{-5/4}$. Putting the different regimes together, σ_{\parallel} slowly increases from $\simeq 10^{-28} \text{ cm}^{-2} \text{ s}$ at $n_H \simeq 10^{-5} \text{ cm}^{-3}$ to $\simeq 10^{-27} \text{ cm}^{-2} \text{ s}$ at $n_H \simeq 10^{-2} \text{ cm}^{-3}$ and rapidly decreases at higher densities, reaching a value of $\simeq 10^{-33} \text{ cm}^{-2} \text{ s}$ at $n_H \simeq 10^2 \text{ cm}^{-3}$. At $n_H \simeq 10^{-1} \text{ cm}^{-3}$, the average scattering coefficient is a few times $10^{-30} \text{ cm}^{-2} \text{ s}$.

The above results for the dependence of scattering rate on density are useful for interpreting the CR pressure distribution displayed in the far right panel of Figure 13. The overall CR distribution follows the gas density distribution, as for the models with uniform $\sigma_{\parallel} = 10^{-27} \text{--} 10^{-28} \text{ cm}^{-2} \text{ s}$ (see Figure 8). Much of the simulation volume is occupied by gas at low density, characterized by $\sigma_{\parallel} \gtrsim 10^{-28} \text{ cm}^{-2} \text{ s}$. Therefore, it is not surprising that the overall CR distribution resembles that of models with high scattering coefficients and ineffective diffusion. The difference with respect to those models arises in regions at higher density $n_H \gtrsim 0.1 \text{ cm}^{-3}$, where the gas is mostly neutral. The very low scattering coefficient in this regime ($\sigma_{\parallel} \lesssim 10^{-29} \text{ cm}^{-2} \text{ s}$) makes diffusion particularly effective in smoothing out CR inhomogeneities within the dense gas.

The right panel of Figure 14 shows the horizontally and temporally averaged vertical profiles of CR pressure, thermal pressure, vertical kinetic pressure, and magnetic stress. The profiles of CR pressure obtained in simulations with uniform σ_{\parallel} are also displayed for comparison. In the midplane, the average CR pressure is higher than the average thermal and kinetic pressure by

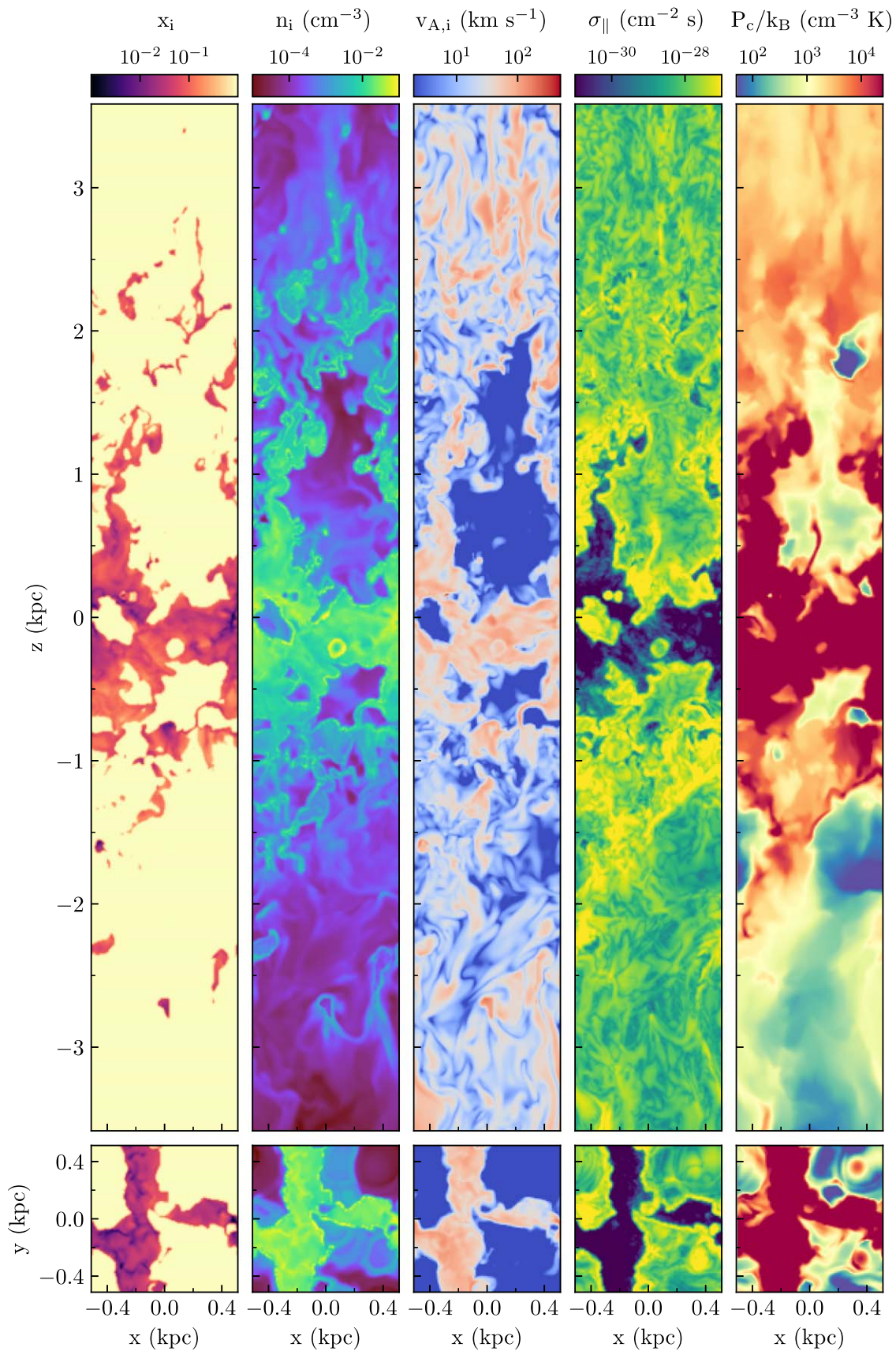


Figure 13. From left to right, distribution on the grid of ionization fraction x_i , ion density n_i , ion Alfvén speed $v_{A,i}$, scattering coefficient parallel in the magnetic field direction σ_{\parallel} , and CR pressure P_c in the self-consistent CR propagation model assuming $\sigma_{\perp} = 10 \sigma_{\parallel}$. The snapshot is taken at $t = 286$ Myr and the slices are extracted at the center of the simulation box.

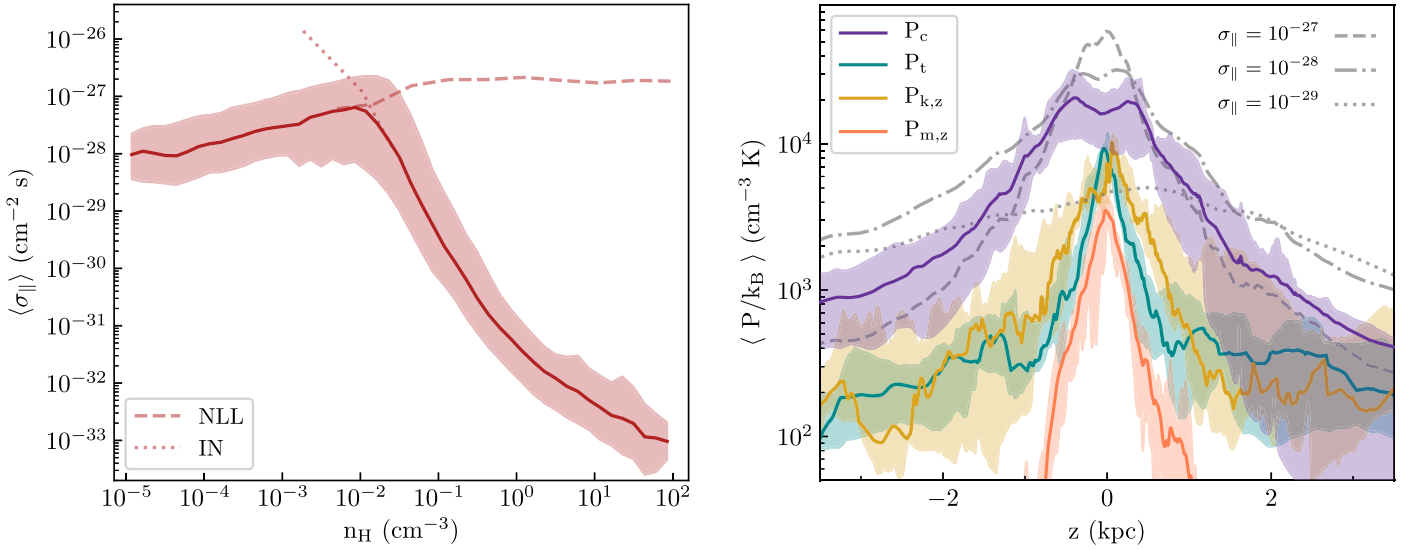


Figure 14. Outcomes of the CR propagation model for the spatially variable scattering treatment with $\sigma_{\perp} = 10 \sigma_{\parallel}$. Left panel: temporally averaged median of the scattering coefficient σ_{\parallel} as a function of hydrogen density n_{H} (solid line). The shaded area covers the temporally averaged variations, calculated as the difference between the 16th and 84th percentiles and the median of the distribution. The dashed and dotted lines show $\sigma_{\parallel, \text{NLL}}$ (Equation (19)) and $\sigma_{\parallel, \text{IN}}$ (Equation (17)), demonstrating that nonlinear Landau damping and ion-neutral damping are more important at low and high density, respectively. Right panel: horizontally and temporally averaged vertical profiles of CR pressure P_{c} (purple), thermal pressure P_{t} (cyan), vertical kinetic pressure $P_{\text{k,z}}$ (yellow), and vertical magnetic stress $P_{\text{m,z}}$ (orange). The shaded areas cover the 16th and 84th percentiles of temporal fluctuations. The dashed, dotted-dashed, and dotted lines indicate the horizontally and temporally averaged vertical profiles of P_{c} from the models with constant $\sigma_{\parallel} = 10^{-27} \text{ cm}^2 \text{ s}$, $10^{-28} \text{ cm}^2 \text{ s}$, and $10^{-29} \text{ cm}^2 \text{ s}$, respectively.

about a factor of 2. The variable- σ model has central P_{c} slightly lower than the $\sigma_{\parallel} = 10^{-28} \text{ cm}^2 \text{ s}$, and high-altitude wings similar to the $\sigma_{\parallel} = 10^{-27} \text{ cm}^2 \text{ s}$ model. Interestingly, even though most of the mass in the disk is at $n_{\text{H}} \simeq 0.1\text{--}1 \text{ cm}^{-3}$, where $\sigma_{\parallel} \lesssim 10^{-30} \text{ cm}^2 \text{ s}$, the midplane CR pressure is higher than that obtained with constant $\sigma_{\parallel} = 10^{-29} \text{ cm}^2 \text{ s}$ everywhere at $|z| \lesssim 1 \text{ kpc}$. Even though both diffusion and streaming are highly effective in the high-density regions of the disk (see also Section 4.2), the propagation of CRs out of the dense gas depends on the properties of the surrounding hotter and lower-density gas which has much higher scattering rates. As a result, CRs are effectively trapped in the midplane region. We conclude that the overall distribution of CRs depends on their propagation in the low-density, hot gas that sandwiches the disk at high altitude.

4.2. Role of Streaming, Diffusive and Advective Transport

In this section, we evaluate the relative contributions of diffusion, streaming, and advection to the overall CR transport when σ_{\parallel} is self-consistently calculated from a balance of the growth and damping rate of resonant Alfvén waves. Figure 15 shows the volume-weighted (red histograms) and mass-weighted (blue histograms) probability distributions of $|v|/|v_{\text{eff}}|$, $|v_{\text{A},i}|/|v_{\text{eff}}|$, and $|v_{\text{d}}|/|v_{\text{eff}}|$, which are the contributions to the total flux from advection, streaming, and diffusion.⁶ For the volume-weighted distributions, the overall profiles and median values are similar to those obtained adopting $\sigma_{\parallel} = 10^{-28} \text{ cm}^2 \text{ s}$. Indeed, most of the simulation volume is occupied by low-density gas ($n_{\text{H}} < 10^{-2} \text{ cm}^{-3}$; see Figure 2), where the average scattering

coefficient is $\gtrsim 10^{-28} \text{ cm}^2 \text{ s}$ (see Figure 14). As for the models with constant σ_{\parallel} , advection with the gas contributes the most to the CR propagation when weighted by volume.

In contrast, if we consider the mass-weighted distributions, both diffusion and streaming transport dominate over advection. In higher-density regions containing most of the gas mass, the scattering coefficient decreases to very low values (see the left panel of Figure 14) due to ion-neutral damping, and CR diffusion becomes quite strong. At the same time, the CR streaming velocity at the ion Alfvén speed $v_{\text{A},i}$ is significantly higher than the ideal Alfvén speed v_{A} adopted in models with constant σ_{\parallel} . For gas at densities above 1 cm^{-3} , the mean value of $v_{\text{A},i}$ is $\simeq 60 \text{ km s}^{-1}$, and the mean ratio $v_{\text{A},i}/v_{\text{A}} = x_i^{-1/2}$ is $\simeq 7$.

In the self-consistent model, we assume that the low-energy slope of the CR spectrum is $\delta = -0.35$ (see Section 2.2.4). This enters in the calculation of both σ_{\parallel} and $v_{\text{A},i}$ through n_i , since $x_i = n_i/n_{\text{H}}$ depends on the low-energy CR ionization rate in high-density/low-temperature regions (see Section 2.2.5).⁷ Since $v_{\text{d}} = |\hat{\mathbf{B}} \cdot \nabla P_{\text{c}}|/(4P_{\text{c}}\sigma_{\parallel})$, the ratio between $v_{\text{A},i} \propto 1/\sqrt{n_i}$ and $v_{\text{d}} \propto \sqrt{n_i}$ scales linearly in $1/x_i$. An increase/decrease of the adopted value of δ would lead to a lower/higher CR ionization rate ζ_{H} (see Equation (25)), with $x_i \propto \zeta_{\text{H}}^{1/2}$ in the warm neutral gas (see Equation (24)). Thus, streaming would be relatively more important compared to diffusion if the relative abundance of low-energy CRs is reduced (a flatter distribution—i.e., higher δ). Even though the relative contribution of diffusion and streaming transport varies with δ , the CR distribution is only weakly affected. We show the results of models assuming different values of δ in Appendix A.3.

Finally, we point out that the outcomes of Figure 15 refer to the self-consistent model assuming $\sigma_{\perp} = 10 \sigma_{\parallel}$. Clearly, the

⁶ In Section 3.2.1, we have explained that the moduli of v , v_{A} , and v_{d} can exceed the modulus of v_{eff} in zones out of steady-state equilibrium characterized by $\sigma_{\text{tot},\parallel} \approx 0$. In models with variable σ , deviations from equilibrium happen mainly in higher-density regions characterized by $\sigma_{\parallel} \ll 10^{-30} \text{ cm}^2 \text{ s} \approx 0$. This explains why the mass-weighted distribution of $v_{\text{d}}/v_{\text{eff}}$, dominated by CRs in higher-density regions, extends orders of magnitude above unity.

⁷ The slope of the low-energy CR spectrum δ also enters in the calculation of σ_{\parallel} through n_i (see Section 2.2.4). However, for the CRs with energies of $\sim 1 \text{ GeV}$ that we are considering in this section, the value of n_i is almost independent of the value of δ .

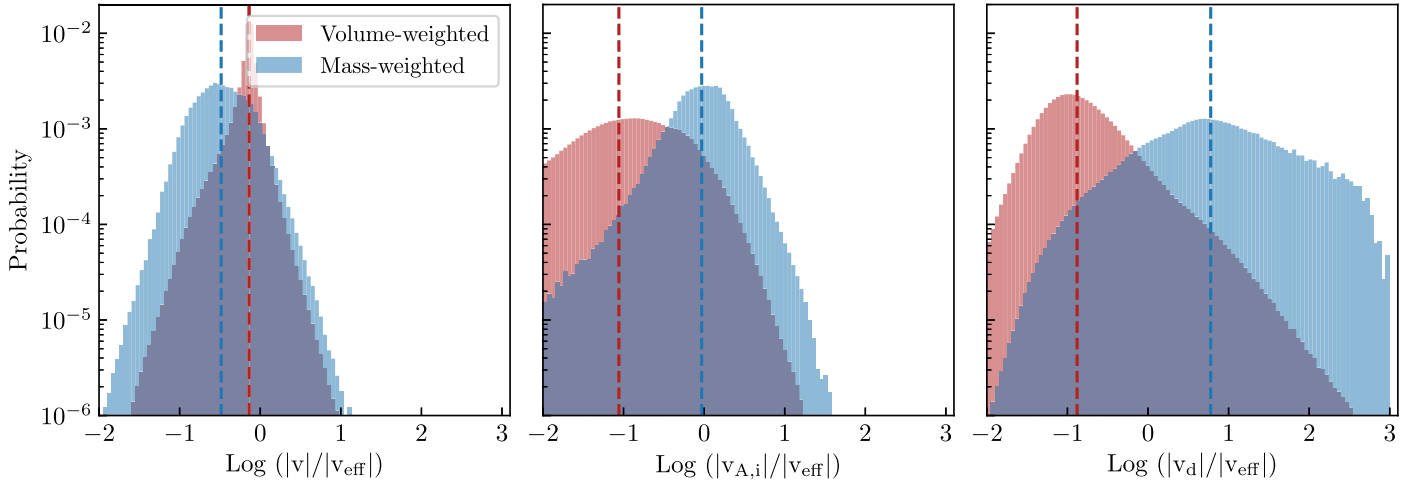


Figure 15. Relative contribution to the total CR flux from advection, streaming, and diffusive terms, for the self-consistent model with $\sigma_{\perp} = 10 \sigma_{\parallel}$. Volume-weighted (red histograms) and mass-weighted (blue histograms) show probability distributions of the ratio between advection speed v (left panel), ion Alfvén speed $v_{A,i}$ (middle panel), diffusive speed v_d (right panel), and the effective total CR propagation speed defined as $v_{\text{eff}} \equiv 3/4 |F_c|/e_c$. The red and blue dashed lines indicate the median values of the volume-weighted and mass-weighted distributions, respectively. The analysis is performed on the snapshots at $t = 286$ Myr.

relative importance of CR diffusion increases/decreases with increasing/decreasing σ_{\perp} , as we show in Section 4.3.

4.3. Models with Different Perpendicular Diffusion

For a uniform background magnetic field, due to pitch-angle scattering CRs diffuse along the magnetic field direction only. However, should magnetic field turbulence be present, CRs can also diffuse perpendicular to the mean magnetic field (e.g., Zweibel 2013; Shalchi 2020). There are several different regimes (see Shalchi 2019) with perpendicular diffusion coefficient $\kappa_{\perp} \sim \kappa_{\parallel} (\delta B/B)^2$ for $(\delta B/B)$ the fractional magnetic field perturbation and $\kappa_{\parallel} \equiv 1/\sigma_{\parallel}$ a parallel transport coefficient. In the case of diffusive parallel transport, the corresponding perpendicular scattering coefficient would be $\sigma_{\perp} \sim \sigma_{\parallel} (B/\delta B)^2$. At the gyroradius scale, $\sim 10^{-6}$ pc, $\delta B/B \ll 1$ and diffusion perpendicular to the mean magnetic field would be negligible compared to parallel diffusion. While in our simulations we directly follow the transport along the magnetic field, we cannot resolve this all the way down to the kinetic scales, and there would be an effective perpendicular diffusion corresponding to magnetic field perturbations (perpendicular “wandering”) that are unresolved by our grid. If we extrapolate the large-scale power down to the grid scale (8 pc) in our simulations, $(\delta B/B)^2$ is non-negligible, of order ~ 0.1 if perturbations are order-unity at the scale height of the disk (~ 300 pc). The implied effective perpendicular diffusion would then be an order of magnitude below the resolved parallel diffusion. While to some extent motivating the default choice $\sigma_{\perp} = 10 \sigma_{\parallel}$, this is by no means rigorous. To address the issue of uncertain perpendicular diffusion, in this section we explore the effect of different choices of σ_{\perp} on the distribution of CR pressure. In addition to the default model ($\sigma_{\parallel} = 10 \sigma_{\perp}$) discussed above, we postprocess the TIGRESS snapshots with a model ignoring perpendicular diffusion ($\sigma_{\perp} \gg 1$) and with a model assuming isotropic diffusion ($\sigma_{\perp} = \sigma_{\parallel}$).

The comparison of results for the three perpendicular diffusion choices is shown in Figure 16. The left panel shows the temporally averaged median value of σ_{\parallel} as a function of n_H . The profiles of σ_{\parallel} produced by the default model and by the model without perpendicular diffusion are nearly identical up to $n_H \simeq 10^{-2} \text{ cm}^{-3}$. At higher density, σ_{\parallel} decreases faster in the

presence of perpendicular diffusion. The model with isotropic diffusion has marginally slower growth in the low-density regime compared to the other two models, while decreasing at a high density similar to the default case. These differences can be attributed to the different CR pressure gradients in the three models. The value of σ_{\parallel} is proportional to $(\hat{\mathbf{B}} \cdot \nabla P_c)^{1/2}$ at low densities and to $|\hat{\mathbf{B}} \cdot \nabla P_c|$ at high densities. CR pressure gradients are more easily smoothed out when the overall diffusion is more effective. This explains why σ_{\parallel} is lower in the case of isotropic diffusion.

The right panel of Figure 16 shows the horizontally and temporally averaged vertical profiles of CR pressure for the three models of perpendicular diffusion. As expected, the CR pressure profile becomes flatter and flatter with increasing perpendicular diffusion. Interestingly, the profile of the default model is closer to that of the model ignoring perpendicular diffusion than to that of the model assuming isotropic diffusion. As discussed above, the overall CR propagation efficiency mostly depends on transport in the low/intermediate-density gas ($n_H < 0.1 \text{ cm}^{-3}$). In the low-density regime ($n_H < 10^{-2} \text{ cm}^{-3}$) advection is by far the dominant transport mechanism (see Section 4.2) and the presence or absence of perpendicular diffusion plays only a marginal role, as confirmed by the almost identical profiles of σ_{\parallel} in the models with pure parallel diffusion and $\sigma_{\parallel} = 10 \sigma_{\perp}$, and the very similar model with $\sigma_{\parallel} = \sigma_{\perp}$. Therefore, the transport of CRs is expected to proceed in the same way at low densities. The slightly different vertical profiles of P_c for the pure parallel diffusion and $\sigma_{\parallel} = 10 \sigma_{\perp}$ models are due to the different diffusivity in the intermediate-density gas ($n_H \simeq 10^{-2} - 10^{-1} \text{ cm}^{-3}$), generally located at the interface between cold/warm and hot gas where advective transport plays a smaller role. In these regions, perpendicular diffusion effectively contributes to transporting CRs perpendicular to the local magnetic field. The lower CR pressure gradients cause the parallel scattering coefficient to decrease (σ_{\parallel} decreases by an order of magnitude when $\sigma_{\perp} = 10 \sigma_{\parallel}$, at $n_H \sim 10^{-1} \text{ cm}^{-3}$) and enhancing the overall diffusion. At density $n_H \gtrsim 1 \text{ cm}^{-3}$ there is appreciably higher σ_{\parallel} for the pure parallel diffusion model than the models with nonzero σ_{\perp} , but this has a negligible effect on the overall

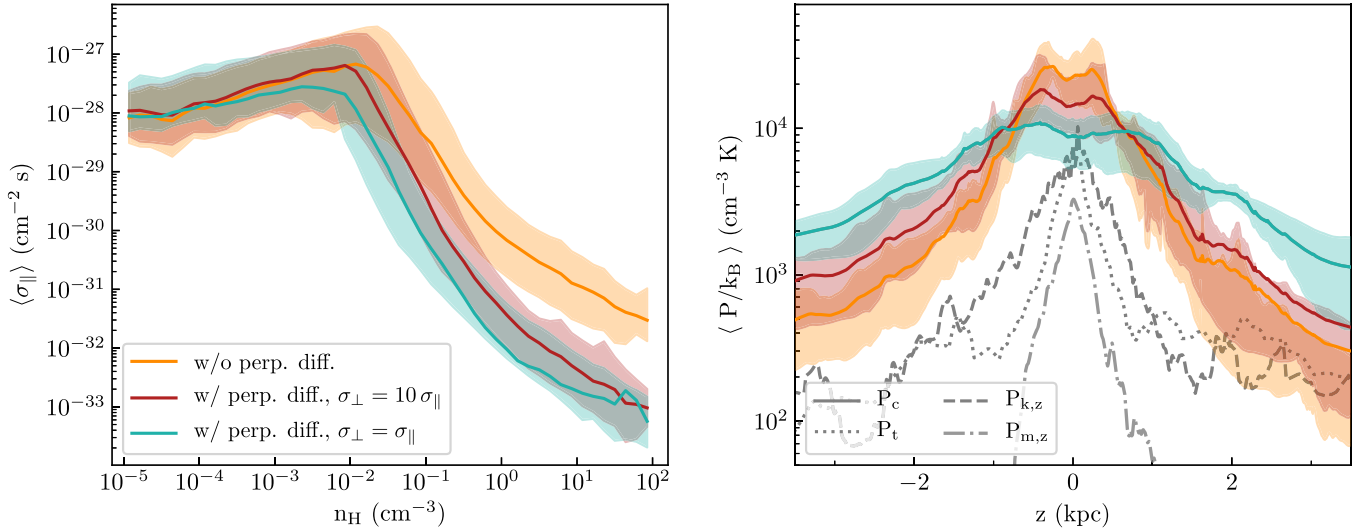


Figure 16. Outcomes of self-consistent CR transport models with different treatments of diffusion perpendicular to the magnetic field. We show cases without perpendicular diffusion (orange line), with $\sigma_{\perp} = 10 \sigma_{\parallel}$ (red line) and with isotropic diffusion $\sigma_{\perp} = \sigma_{\parallel}$ (turquoise line). Left panel: temporally averaged median of the scattering coefficient σ_{\parallel} as a function of hydrogen density n_{H} . Right panel: horizontally and temporally averaged vertical profiles of CR pressure P_{c} . For both panels, the shaded areas cover the 16th and 84th percentiles of temporal fluctuations. The gray lines show the horizontally and temporally averaged profiles of thermal pressure P_{t} (dotted line), vertical kinetic pressure $P_{\text{k,z}}$ (dashed line), and vertical magnetic stress $P_{\text{m,z}}$ (dotted-dashed line).

CR distribution because σ is still extremely low ($< 10^{-30}$ cm² s; see Section 4.4 and Figure 17).

In the presence of isotropic diffusion the CR pressure profile is much smoother than in the case with $\sigma_{\perp} = 10 \sigma_{\parallel}$, even though the parallel scattering coefficients are quite similar at very low density and differ by a factor of a few at higher densities. However, the factor-of-a-few reduction in σ_{\parallel} corresponds to a reduction of a few tens in σ_{\perp} compared to the $\sigma_{\perp} = 10 \sigma_{\parallel}$ case. The effect of reduced σ_{\perp} may be amplified at the interfaces between the midplane layer of warm/cold gas and the surrounding mostly hot corona because the magnetic field is preferentially horizontal near the midplane region. The result of isotropic diffusion is significantly more effective CR diffusion overall, and a lower central CR pressure.

Finally, we summarize the relative importance of individual energy sink/source terms for the three transport models analyzed here. We calculate the time-averaged integral of the sink/source terms in the rhs of Equation (1) over the whole simulation domain (see Section 3.2.2 for comparison with models assuming constant scattering). The average CR energy injected per unit time is 1.8×10^{38} erg s⁻¹ for all models. For the model without perpendicular diffusion, we find that relative to the input, the collisional loss is 0.34, the streaming loss is 1.9, and the energy gain from the gas is 1.6. For $\sigma_{\perp} = 10 \sigma_{\parallel}$, the relative collisional loss is 0.23, the streaming loss is 1.4, and the gain from the gas is 1.2. With isotropic diffusion, the relative collisional loss is 0.12, the streaming loss is 0.83, and the gain from the gas is 1.05. As noted for the constant diffusivity models, the total rates of energy transfer decrease with increasing diffusivity. In each model, the absolute value of the streaming loss rate and of the adiabatic gain rate is comparable, while the collisional loss rate is only 10%–20% of the other terms in absolute value.

From the total rate of collisional losses and the total rate of energy injection, we calculate that the grammage (Equation (27)). This is ~ 53 g cm² in the absence of perpendicular diffusion, ~ 34 g cm² when $\sigma_{\perp} = 10 \sigma_{\parallel}$, and ~ 20 g cm² for isotropic diffusion. These values are from 5 to 2 times larger than the grammage measured at the Earth

(~ 10 g cm⁻², e.g., Hanasz et al. 2021). We point out that the grammage is proportional to the rate of fractional losses, which depends on the CR energy density (see Equation (27)). The higher grammage measured in our physically motivated models reflects the fact that the predicted CR energy density is slightly larger than the observed one. We refer to Section 6.1 for a discussion about possible reasons for this mismatch.

4.4. Relation Between CR Pressure and Gas Density

We now analyze the relation between CR pressure and gas density in models with a variable scattering coefficient. In Figure 17, we show the temporally averaged mean of P_{c} as a function of n_{H} from the self-consistent models without perpendicular diffusion (orange), with $\sigma_{\perp} = 10 \sigma_{\parallel}$ (red), and with isotropic diffusion (turquoise). For comparison, we also plot the mean values of P_{c} from the models with $\sigma_{\parallel} = 10^{-27}$ cm² s and with $\sigma_{\parallel} = 10^{-28}$ cm² s. In all three self-consistent models, the mean value of P_{c} increases with n_{H} at low density while having a constant value in the high-density regime. The slope of $\log P_{\text{c}}$ versus $\log n_{\text{H}}$ in the low/intermediate-density regime and the value of P_{c} in the high-density plateau both decrease as the efficiency of perpendicular diffusion increases. As expected, the correlation between P_{c} and n_{H} weakens with isotropic diffusion, since CR inhomogeneities caused by nonuniform advection are more easily erased, while correlations strengthen in the absence of perpendicular diffusion. As explained for Figure 16, the value of P_{c} in the high-density gas is mainly determined by the propagation efficiency at the interface between cold/warm and hot gas. CRs are trapped in the dense neutral gas for a longer time when diffusion is less effective, thus increasing their pressure. The $P_{\text{c}}-n_{\text{H}}$ relation in the case without perpendicular diffusion resembles that of the $\sigma_{\parallel} = 10^{-27}$ cm² s model in the low-density regime, while it coincides with that of the $\sigma_{\parallel} = 10^{-28}$ cm² s model at high densities. This evidence suggests that the effective scattering coefficient for the most realistic model of CR propagation assuming pure parallel diffusion is between 10^{-27} and 10^{-28} cm² s.

It is interesting to note that, in addition to the extremely constant value of P_c at densities above $n_H \gtrsim 0.01$ – 0.1 (i.e., in the warm/cold gas), the three self-consistent models predict negligible scatter around the mean value of P_c , unlike the models with constant scattering coefficient in the range $\sigma_{\parallel} > 10^{-29} \text{ cm}^2 \text{ s}$ (see Figure 12). This is because ion-neutral damping reduces σ_{\parallel} below $10^{-29} \text{ cm}^2 \text{ s}$ in the high-density gas for all cases (see left panel of Figure 16), and this is low enough to make the CR pressure extremely uniform. This result is particularly important to understanding the dynamical effects of CRs. The absence of CR pressure gradients in the denser regions of the galactic disk implies that CRs do not apply forces to the gas there. This, together with the comparison between the CR and other pressure profiles in the right panel of Figure 16, suggests that CRs are not important to vertical support of the ISM disk in the midplane region, while at the same time having potentially great importance to galactic wind launching/fountain dynamics which takes place at high altitudes ($|z| \gtrsim 0.5 \text{ kpc}$).

5. Low-energy Cosmic Rays

In this section, we investigate the propagation and distribution of low-energy ($\sim 30 \text{ MeV}$) CRs using models with a variable scattering coefficient (see Sections 2.2.2 and 2.2.4 for the treatment of low-energy CRs) ignoring the presence of diffusion perpendicular to the magnetic field direction. Different models are characterized by different assumptions for the fraction of low-energy CRs injected per supernova event. The differing injection fractions correspond to different assumptions for the low-energy slope of the CR injection spectrum δ_{inj} , which is observationally quite uncertain. In this work, we explore three values of δ_{inj} : -0.8 , -0.35 , 0.1 .

5.1. Scattering Rate Coefficient and Mean Free Path

In the left panel of Figure 18, we compare the temporally averaged value of the scattering coefficient of high- and low-energy CRs as a function of hydrogen density. Even though the overall profiles are similar, i.e., σ_{\parallel} slightly increases with n_H up to $n_H \simeq 10^{-2} \text{ cm}^{-3}$ and rapidly decreases at higher densities, the scattering coefficient of low-energy CRs at a given density increases with decreasing δ_{inj} and, regardless of the value of δ_{inj} , is always higher than the scattering coefficient of high-energy CRs. We note that σ_{\parallel} depends on n_1 (Equation (15)), which in turn depends both on the shape of the CR energy spectrum and on the CR kinetic energy. In particular, in the low-density regime, where $\Gamma_{\text{nll}} > \Gamma_{\text{in}}$, $\sigma_{\parallel} \propto \sqrt{n_1}$, while in the high-density regime, where $\Gamma_{\text{nll}} < \Gamma_{\text{in}}$, $\sigma_{\parallel} \propto n_1$ (see Equations (19) and (17)). In Appendix A.1, we show that the value of n_1 at $E_k \sim 30 \text{ MeV}$ increases by a factor of ~ 7 when the low-energy slope of the spectrum decreases from 0.1 to -0.8 . In Figure 18, we can in fact see that the average ratio between the value of σ_{\parallel} predicted by the model assuming $\delta_{\text{inj}} = -0.8$ and the value of σ_{\parallel} predicted by the model assuming $\delta_{\text{inj}} = 0.1$ is ≈ 2 – 3 at $n_H \lesssim 10^{-2} \text{ cm}^{-3}$, where non-linear Landau damping dominates, and slightly less than one order of magnitude at $10^{-2} < n_H < 1 \text{ cm}^{-3}$, where ion-neutral damping dominates. At higher densities, the distributions of σ_{\parallel} predicted by the three different models for low-energy CRs nearly overlap. In this density regime, the scattering coefficient decreases with increasing the CR ionization rate (because $\sigma_{\parallel} \propto n_i^{-1/2} \propto \zeta_c^{-1/4}$; see Appendix A.3), which, in turn,

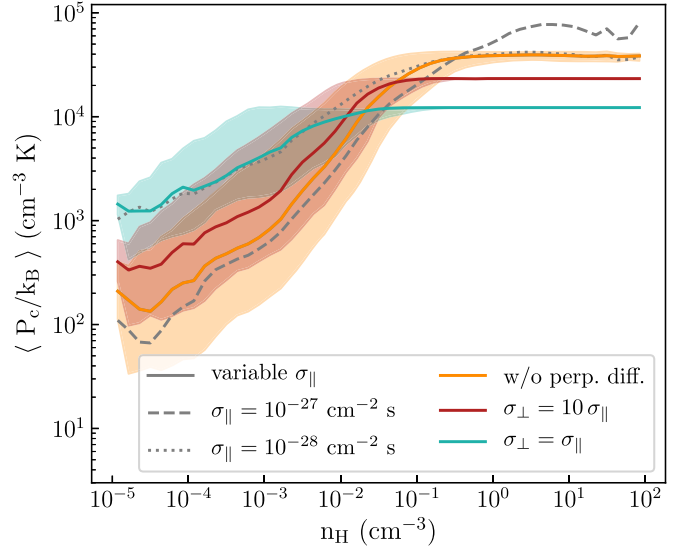


Figure 17. Temporally averaged mean CR pressure P_c as a function of hydrogen density n_H from self-consistent CR transport models with different treatments of diffusion perpendicular to the magnetic field. We show cases without perpendicular diffusion (orange line), with $\sigma_{\perp} = 10 \sigma_{\parallel}$ (red line), and with isotropic diffusion $\sigma_{\perp} = \sigma_{\parallel}$ (turquoise line). The shaded areas cover the 16th to 84th percentiles of the temporally averaged variations around the mean. For comparison, the results from models with $\sigma_{\parallel} = 10^{-27} \text{ cm}^2 \text{ s}$ (dashed gray line) and with $\sigma_{\parallel} = 10^{-28} \text{ cm}^2 \text{ s}$ (dotted gray line) are also shown.

increases with decreasing δ_{inj} . Thus, the tendency for σ_{\parallel} to increase with n_1 at lower δ_{inj} is counterbalanced by the decrease of $n_i^{-1/2}$.

In Appendix A.1, we also show that, regardless of the value of δ , n_1 is always higher at $E_k = 30 \text{ MeV}$ than at $E_k = 1 \text{ GeV}$ for a given spectrum normalization. In particular, the value of n_1 at $E_k = 30 \text{ MeV}$ is a factor of ~ 3 higher than the value of n_1 at $E_k = 1 \text{ GeV}$ if $\delta = 0.1$ and more than one order of magnitude if $\delta = -0.8$. In Figure 18, we can however observe that σ_{\parallel} decreases by more than a factor $\sqrt{n_1}$ going from low-energy to high-energy CRs at $n_H \lesssim 10^{-2} \text{ cm}^{-3}$. The reason is that, in the low-density regime, the scattering rate is inversely proportional to the particle speed v_p (see Equation (19)), which is higher for CRs with $E_k = 1 \text{ GeV}$ ($v_p \simeq 2.6 \times 10^{10} \text{ cm s}^{-1}$) than for CRs with $E_k = 30 \text{ MeV}$ ($v_p \simeq 7.4 \times 10^9 \text{ cm s}^{-1}$). Moreover, as diffusion becomes more important for high-energy CRs, the scale heights of their distribution decrease ($\sigma_{\parallel} = \sigma_{\parallel, \text{NLL}} \propto (|\hat{B} \cdot \nabla P_c|/P_c)^{-1/2}$).

The right panel of Figure 18 shows the temporally averaged mean free path of high- and low-energy CRs as a function of hydrogen density. The mean free path λ_c is calculated as $(v_p \sigma_{\parallel})^{-1}$, where v_p is the CR velocity (Equation (10)). Since the speed of CRs with $E_k = 1 \text{ GeV}$ is higher than the speed of CRs with $E_k = 30 \text{ MeV}$, the mean free path of high-energy CRs is only slightly larger than the mean free path predicted by the propagation models for low-energy CRs assuming $-0.35 < \delta_{\text{inj}} < 0.1$, even though the scattering coefficient is lower. For high-energy (low-energy) CRs, the average mean free path decreases from $\lambda_c \simeq 0.1$ – 0.2 pc ($\lambda_c \simeq 0.03$ – 0.06 pc) at $n_H = 10^{-5} \text{ cm}^{-3}$ to $\lambda_c \simeq 0.01$ – 0.03 pc ($\lambda_c \simeq 0.05$ – 0.1 pc) at $n_H \simeq 10^{-2} \text{ cm}^{-3}$, where scattering is highly effective. At higher densities, the mean free path quickly increases as the scattering coefficient decreases. At $n_H \simeq 10$ – 10^2 cm^{-3} —the characteristic density of cold atomic and diffuse molecular clouds— $\lambda_c \sim 30$ – 300 pc for low-energy CRs and slightly higher for high-energy CRs. With a mean free path in the cold dense gas comparable to the size of individual clouds,

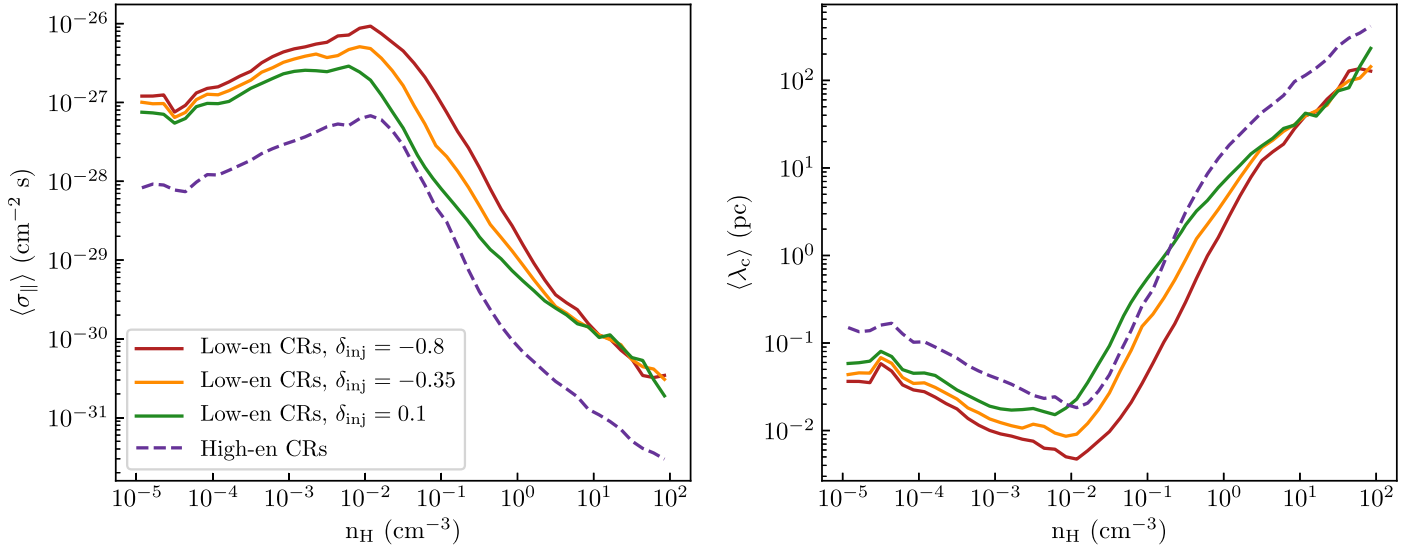


Figure 18. Temporally averaged median of the scattering coefficient σ_{\parallel} (left panel) and mean free path λ_c (right panel) of high-energy (dashed lines) and low-energy (solid lines) CRs. For low-energy CRs, three different values of the low-energy slope of the source spectrum have been explored: -0.8 (red lines), -0.35 (orange lines), and 0.1 (green lines). All cases assume no diffusion in the direction perpendicular to the magnetic field lines.

CRs freely stream across them (subject, however, to the increased collisional losses at higher density).

5.2. Density Dependence and CR Losses

The results of the propagation models for low-energy CRs and a comparison with results for high-energy CRs are displayed in Figure 19. The left panel shows the temporally averaged median density, $E_k n_c(E_k)$, of CRs with kinetic energy $E_k \simeq 30$ MeV and $E_k \simeq 1$ GeV in a bin of width E_k as a function of hydrogen density n_{H} . For low-energy CRs, $E_k n_c(E_k = 30 \text{ MeV}) = e_c(\text{MeV}) / \Delta E_k \cdot E_k / E(E_k)$, with $\Delta E_k = 1$ MeV (see Section 2.2.4). For high-energy CRs, the normalization of $n_c(E_k)$ is calculated from the energy density $e_c(\text{GeV})$ using Equation (22), while the low-energy slope is assumed to be -0.35 (default model). At a given n_{H} , the average CR density increases for lower δ_{inj} for the $E_k = 30$ MeV CRs, and for $\delta_{\text{inj}} = -0.35$ and -0.8 the number density is also higher than for the GeV CRs, consistent with the injection spectrum. Despite the shift in normalization, the distributions of CR density predicted by the four models are roughly similar, with n_c increasing up to $n_{\text{H}} \sim 0.01$ – 0.1 cm^{-3} and flattening at higher densities. However, unlike the model assuming $\delta_{\text{inj}} = 0.1$, the models with $\delta_{\text{inj}} = -0.35$ and -0.8 predict a slight decrease of CR density at $n_{\text{H}} \gtrsim 10 \text{ cm}^{-3}$. For these models, the higher scattering rates in the intermediate/low-density gas (see Figure 18) trap CRs more effectively near the midplane, and this provides more time for CRs in the dense gas to lose energy. Since the rate of energy losses increases with n_{H} (Equation (12)), the CR density decreases with n_{H} .

For a more direct comparison between the energy density distributions of high- and low-energy CRs, in the right panel of Figure 19 we show the average distributions of $P_c(\text{GeV})/\epsilon_c(\text{GeV})$ and $P_c(\text{MeV})/\epsilon_c(\text{MeV})$, where $\epsilon_c(\text{GeV})$ and $\epsilon_c(\text{MeV})$ are the fractions of supernova energy converted into GeV and MeV CRs respectively, as a function of n_{H} . ϵ_c is set to 0.1 for high-energy CRs, while it depends on the assumption made for δ_{inj} for low-energy CRs, as shown in the legend of Figure 19. As explained in Sections 3.3 and 4.4, the effect of increasing scattering is to prevent the propagation of

CRs from high-density to low-density regions. As a consequence, for higher σ the CR pressure tends to decrease in low-density regions and increase in higher-density regions (see also Figures 12 and 17). In Figure 19, at low gas densities P_c/ϵ_c indeed decreases going from high-energy to low-energy CRs and going from the model with $\delta_{\text{inj}} = 0.1$ to the model $\delta_{\text{inj}} = -0.8$. However, in the high-density regime, P_c/ϵ_c is always lower for low-energy than for high-energy CRs, even though the higher scattering of the MeV CRs traps them more effectively. The reason is that low-energy CRs undergo more significant collisional energy losses, which are particularly effective in dense gas.

We find that the average fraction of injected energy lost via collisions with the ambient gas is ~ 0.59 , ~ 0.52 and ~ 0.41 for low-energy CRs models adopting $\delta_{\text{inj}} = -0.8$, -0.35 , and 0.1 , respectively. These losses exceed the fractional loss $f_{\text{coll}} \sim 0.34$ for high-energy CRs. Based on Equation (27), the time-averaged grammage of low-energy CRs is ~ 12 , ~ 10 , and $\sim 8 \text{ g cm}^{-2}$ for the case $\delta_{\text{inj}} = -0.8$, -0.35 , and 0.1 , respectively, lower than the time-averaged grammage of high-energy CRs $\sim 53 \text{ g cm}^{-2}$. We note that even though the fractional loss is larger for low-energy CRs than for high-energy CRs, the latter are characterized by a larger velocity, which explains why their grammage exceeds the grammage of low-energy CRs.

5.3. Role of Streaming, Diffusive, and Advective Transport

In this section, we evaluate the relative contribution of streaming, diffusion, and advection to the overall propagation of low-energy CRs. Figure 20 shows the volume-weighted (red histograms) and mass-weighted (blue histograms) probability distributions of $|v|/|v_{\text{eff}}|$, $|v_{A,i}|/|v_{\text{eff}}|$, and $|v_d|/|v_{\text{eff}}|$ for the model adopting $\delta_{\text{inj}} = -0.35$. As for high-energy CRs, advection contributes the most to the transport of CRs when weighted by volume, while streaming and diffusion dominate over advection when weighted by gas mass (see Section 4.2). However, unlike high-energy CRs, the streaming velocity of low-energy CRs is on average larger than their diffusion velocity. While the streaming velocity distribution is the same

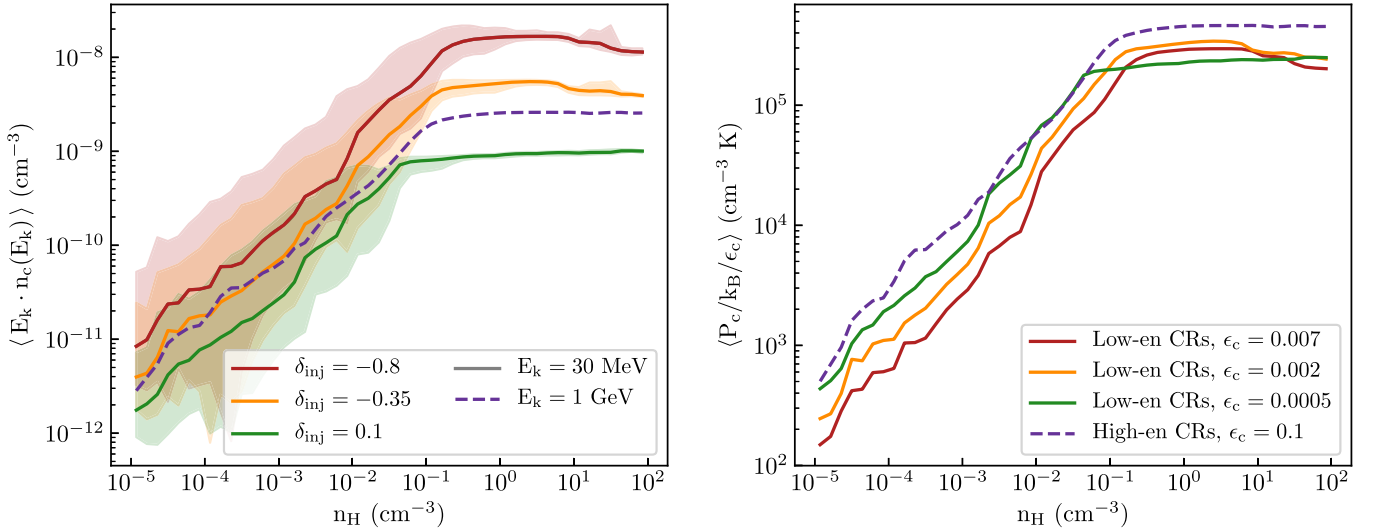


Figure 19. Comparison of the self-consistent transport model for high- and low-energy CRs, for models without perpendicular diffusion. For low-energy CRs, three different values of the low-energy slope of the injected spectrum have been explored: $\delta_{\text{inj}} = -0.8$ (red lines), -0.35 (orange lines), and 0.1 (green lines). Left panel: temporally averaged median density of CRs in a bin of width E_k as a function of hydrogen density n_H , for $E_k = 30$ MeV (solid lines), and $E_k = 1$ GeV (dashed line). The shaded areas cover the 16th and 84th percentiles of the distribution. Right panel: temporally averaged median pressure P_c of high-energy (dashed line) and low-energy (solid lines) CRs as a function of hydrogen density n_H . The value of P_c is divided by ϵ_c , the fraction of supernova energy converted into CRs with a given kinetic energy. The fraction $\epsilon_c = 0.1$ for high-energy CRs, while it depends on the assumption made for δ_{inj} for low-energy CRs.

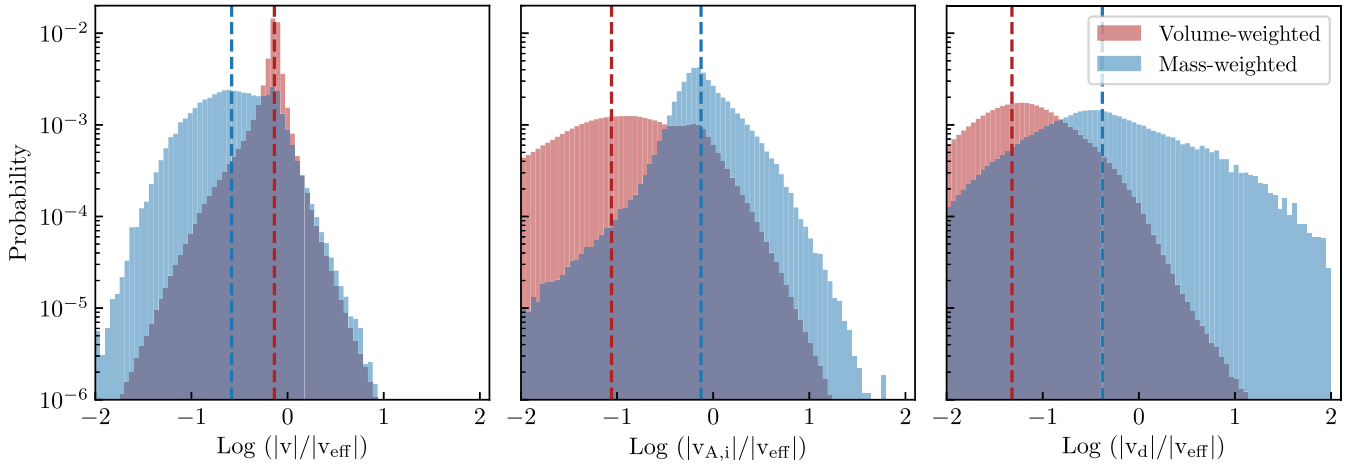


Figure 20. Relative contribution to the total flux of low-energy CRs from advection, streaming, and diffusive terms, for the self-consistent model without perpendicular diffusion. Volume-weighted (red histograms) and mass-weighted (blue histograms) show probability distributions of the ratio between advection speed v (left panel), ion Alfvén speed $v_{A,i}$ (middle panel), diffusive speed v_d (right panel), and the effective total CR propagation speed defined as v_{eff} . The red and blue dashed lines indicate the median values of the volume-weighted and mass-weighted distributions, respectively. The analysis is performed on the snapshot at $t = 286$ Myr adopting the model with $\delta_{\text{inj}} = -0.35$.

for low-energy and high-energy CRs,⁸ the diffusion velocity distribution is different. In Section 5.1, we have indeed seen that in higher-density regions, containing the bulk of the gas mass, the scattering coefficient of low-energy CRs is almost one order of magnitude larger than the scattering coefficient of high-energy CRs (see Figure 18), which results in a lower diffusion velocity for low-energy CRs compared to high-energy CRs. We therefore conclude that streaming is the primary transport mechanism for low-energy CRs in the midplane regions containing most of the ISM mass. We find that diffusion dominates over streaming in highly dense regions ($n_H > 10 \text{ cm}^{-3}$) only. A caveat, however, is that if the overall

level of CRs were decreased (e.g., with altered magnetic field topology; see Section 6.1), the scattering rate would drop and this would tend to enhance diffusion.

5.4. CR Spectrum and Ionization Rate

We now focus on the effect of different choices of δ_{inj} on the average CR ionization rate in the midplane region of the galactic disk ($|z| \leq 250$ pc). Figure 21 shows the temporally averaged low-energy slope of the CR spectrum (Equation (23)) and primary CR ionization rate of atomic hydrogen (Equation (25)) as a function of hydrogen density obtained under the three different assumptions of δ_{inj} . As the propagation of high- and low-energy CRs differ, with the latter scattering more and having more significant collisional energy losses, the local slope of the spectrum differs from the slope of the injected

⁸ Strictly speaking this could differ, but the spectrum normalization used to calculate the CR ionization rate (Equation (25)), relevant for the calculation of the ion Alfvén speed, is the same for low-energy and high-energy CRs.

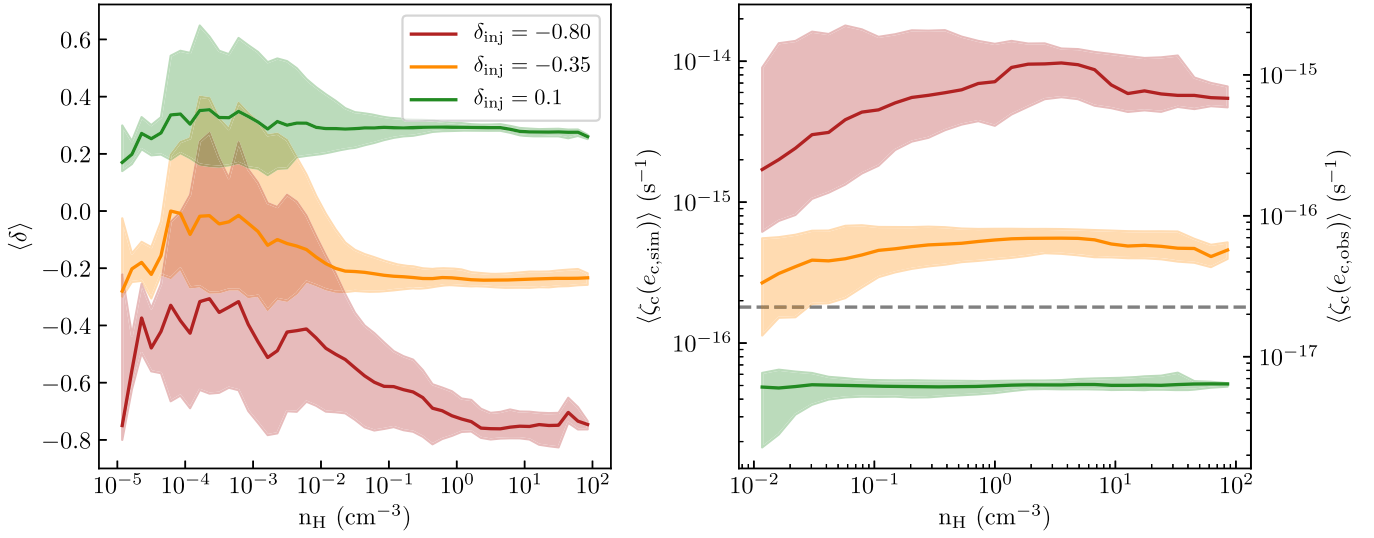


Figure 21. Temporally averaged median of the low-energy slope δ (left panel) and primary CR ionization rate of atomic hydrogen ζ_c (right panel) as a function of hydrogen density n_H in models with $\delta_{inj} = -0.8$ (red lines), $\delta_{inj} = -0.35$ (orange lines), and $\delta_{inj} = 0.1$ (green lines). In the right panel, the left-hand side y-axis denotes $\zeta_c(e_{c,sim})$, the primary CR ionization rate calculated adopting the spectrum normalization C (Equation (22)) predicted by the self-consistent GeV propagation model without perpendicular diffusion analyzed in Section 4.3, while the right-hand-side y-axis denotes $\zeta_c(e_{c,obs})$, the primary CR ionization rate calculated assuming that the mean energy density of high-energy CRs near the midplane is 1 eV cm^{-3} , as observed in the solar neighborhood. In both plots, the shaded areas cover the 16th and 84th percentiles of the distribution at a given n_H .

spectrum. The local slope δ is equal to δ_{inj} at very low densities ($n_H \sim 10^{-5} \text{ cm}^{-3}$) only, i.e., at the typical densities of supernova remnants where CRs are injected, and increases with the gas density up to $n_H \approx 10^{-3} \text{ cm}^{-3}$. Since diffusion is less effective for low-energy CRs, the ratio between $e_c(\text{GeV})$ and $e_c(\text{MeV})$ is higher than their injection ratio in the low-density regime away from injection sites (see Section 5.3 and Figure 19), thus making the CR spectrum flatter at $n \sim 10^{-3} \text{ cm}^{-3}$. At higher densities, δ approaches a constant value for $n_H \gtrsim 0.1\text{--}1 \text{ cm}^{-3}$ which is slightly larger than δ_{inj} . This reflects the near-constant level of e_c for both high- and low-energy CRs at high gas densities. We note that the scatter in the distribution of δ increases at a given n_H with decreasing δ_{inj} as diffusion becomes less effective.

In the right panel of Figure 21, the trend of the CR ionization rate ζ_c is analyzed for $n_H \geq 10^{-2} \text{ cm}^{-3}$ only, since hydrogen is fully ionized at lower densities. The overall distribution of ζ_c reflects that of e_c for low-energy CRs (Figure 19), i.e., ζ_c becomes more uniform with increasing δ_{inj} . In the local Milky Way, the primary CR ionization rate of atomic hydrogen measured in local diffuse molecular clouds ($n_H \approx 100 \text{ cm}^{-3}$) is $\zeta_c = 1.8^{+1.3}_{-1.1} \times 10^{-16} \text{ s}^{-1}$ (e.g., Indriolo & McCall 2012; Indriolo et al. 2015; Bacalla et al. 2019; see also review by Padovani et al. 2020 and references therein). These numbers lie between the value of $\zeta_c \approx 6 \times 10^{-17} \text{ s}^{-1}$ predicted by the model assuming $\delta_{inj} = 0.1$ and the value of $\zeta_c \approx 5 \times 10^{-16} \text{ s}^{-1}$ predicted by the model assuming $\delta_{inj} = -0.35$ at $n_H \approx 100 \text{ cm}^{-3}$. However, as we shall discuss in Section 6.1, the average energy density of high-energy CRs predicted by the self-consistent model is in fact larger than the average energy density measured in the local ISM, and the normalization of the ionization rate is set by the GeV energy density (in this case, using the model without perpendicular diffusion). To match the observed midplane GeV energy density of 1 eV cm^{-3} , we can reduce the ionization rates predicted by our models, $\zeta_c(e_{sim})$, by a factor of 8; the resulting $\zeta_c(e_{obs})$ is indicated on the rhs y-axis of Figure 21. Accounting for this reduction, the observed CR ionization rate lies between the value of $\zeta_c \approx 7 \times 10^{-17} \text{ s}^{-1}$

predicted by the model adopting $\delta_{inj} = -0.35$ and the value of $\zeta_c \approx 7 \times 10^{-16} \text{ s}^{-1}$ predicted by the model adopting $\delta_{inj} = -0.8$. We note that the values of ζ_c displayed in Figure 21 have been obtained adopting $E_{k,min} = 10^5 \text{ eV}$ in Equation (25). Using $E_{k,min} = 10^6 \text{ eV}$, consistent with the minimum CR energy probed by Voyager 1, the value of $\zeta_c(e_{obs})$ for the $\delta_{inj} = -0.8$ model would be in better agreement with the observed value (see Appendix A.2).

We conclude that $-0.35 < \delta < -0.8$ might be a good approximation for the low-energy slope of the injected CR energy spectrum and that the average value of δ at the average ISM densities ($n_H \approx 0.1\text{--}1 \text{ cm}^{-3}$) is likely to lie between -0.7 and -0.25 . Moreover, we note that the slight anticorrelation between CR ionization rate and hydrogen density predicted by the model adopting $\delta_{inj} = -0.8$ at $n_H > 1 \text{ cm}^{-3}$ is generally in agreement with observations of diffuse molecular clouds in the solar neighborhood (e.g., Neufeld & Wolfire 2017, but note that the observed anticorrelation is between the CR ionization rate and column density rather than volume density). We further discuss these results in Section 6.4.

6. Discussion

6.1. CR Pressure in the Galactic Disk

Except for the case with isotropic diffusion, the self-consistent propagation models presented in Section 4 predict that near the midplane the average pressure of CRs with kinetic energies of $\gtrsim 1 \text{ GeV}$ is $P_c/k_B = (2\text{--}3) \times 10^4 \text{ cm}^{-3} \text{ K}$, under the assumption that the energy input rate is $\epsilon_c = 10\%$ of the SN rate. This is a few times larger than the midplane thermal, kinetic, and magnetic field pressures, each of which is $\approx 10^4 \text{ cm}^{-3} \text{ K}$ in the warm/cold atomic gas which comprises most of the ISM's mass (see Figures 2 and 16, and note that the magnetic pressure is lower in the hot gas). While still close to equipartition, the CR pressure here exceeds that of the other ISM components. This can be compared with the local Milky Way, where the estimated cosmic ray, thermal, kinetic, and magnetic pressures are individually in the range

$\sim 3000\text{--}10,000\text{ cm}^{-3}\text{ K}$, i.e., somewhat closer to equipartition with each other (as well as slightly smaller than in the simulation).

When star formation feedback dominates other energy inputs to the ISM, approximate equipartition can be understood based on input rates (mostly from radiation and supernovae) and the response of the ISM to the various forms of input. The individual pressures are set by balancing far-UV (photoelectric) heating and cooling for thermal pressure (Ostriker et al. 2010), balancing momentum flux injection from supernovae with kinetic turbulent pressure (Ostriker & Shetty 2011), and applying turbulent driving in combination with shear to maintain the pressure in the magnetic field (Kim & Ostriker 2015). The ratios between midplane pressure components and the star formation rate per unit area Σ_{SFR} are the feedback “yield” components (Kim et al. 2013, 2020a, 2020b; E. C. Ostriker & C.-G. Kim 2021, in preparation), and the ratios among the individual pressure components simply reflect the relative feedback yields.

Just as for the other pressure components that derive from star formation feedback, there must be a relationship between the midplane CR pressure $P_c(0)$ and Σ_{SFR} . In the case of negligible losses (collisional or via work on the gas), the average vertical flux of CR energy above the SN input layer would be $F_{c,z} = (1/2)\epsilon_c E_{\text{SN}} \Sigma_{\text{SFR}} / m_*$, where m_* is the total mass of new stars per supernova ($95.5 M_\odot$ in Kim & Ostriker 2017, from a Kroupa IMF); this “no-losses” CR flux is $2 \times 10^{45}\text{ erg yr}^{-1}\text{ kpc}^{-2}$. We can also relate the flux and pressure by $P_c(0) = \sigma_{\text{eff}} H_{c,\text{eff}} F_{c,z}$ for $H_{c,\text{eff}} = \langle |d \ln P_c / dz| \rangle^{-1}$ an effective CR scale height and σ_{eff}^{-1} an effective diffusion coefficient. With $H_{c,\text{eff}} \sim 1.0\text{ kpc}$ from our self-consistent simulations with $\sigma_\perp = 10\sigma_\parallel$, the midplane pressure-flux relation would be satisfied for $\sigma_{\text{eff}} = 7 \times 10^{-29}\text{ cm}^{-2}\text{ s}$, while $H_{c,\text{eff}} \sim 0.7\text{ kpc}$ and $\sigma_{\text{eff}} = 2 \times 10^{-28}\text{ cm}^{-2}\text{ s}$ for the model without perpendicular diffusion. Note that these values of σ_{eff} use the actual midplane CR pressure and vertical CR flux at $|z| = 1\text{ kpc}$ ($2.4 \times 10^{45}\text{ erg yr}^{-1}\text{ kpc}^{-2}$ or $1.9 \times 10^{45}\text{ erg yr}^{-1}\text{ kpc}^{-2}$, respectively), which differ slightly from the “no-losses” vertical CR flux. By comparison, the P_c versus n_{H} relation in our self-consistent models is best matched by the constant σ models when $\sigma_\parallel = 10^{-27}\text{--}10^{-28}\text{ cm}^{-2}\text{ s}$ (depending on the density range; see Figure 17), consistent with the measured peaks in σ_\parallel in Figure 16. The lower σ_{eff} can be understood since (1) in fact advection dominates in the lowest-density gas, and (2) Alfvénic streaming and diffusion are comparable when realistic ionization is taken into account (Figure 15). Both of these effects increase the rate of transport, contributing to a reduction in σ_{eff} compared to the actual scattering rate. The corresponding CR feedback “yield”

$$\Upsilon_c \equiv \frac{P_c(0)}{\Sigma_{\text{SFR}}} = \frac{1}{2} \epsilon_c \sigma_{\text{eff}} H_{c,\text{eff}} \frac{E_{\text{SNe}}}{m_*} \quad (28)$$

would then be $\Upsilon_c \sim 600\text{ km s}^{-1}$ or $\sim 1000\text{ km s}^{-1}$, respectively, for the $\sigma_\perp = 10\sigma_\parallel$ model or the model without perpendicular diffusion.

In the TIGRESS simulations (and presumably for the real ISM as well), the disk as a whole is in vertical dynamical equilibrium, with the ISM weight \mathcal{W} balanced by the difference ΔP between midplane pressure and pressure at the top of the atomic/molecular layer. In the current TIGRESS simulations, the weight is balanced by the sum of the midplane thermal, kinetic, and magnetic pressure (Kim et al. 2020b; Vijayan et al. 2020; Ostriker & Kim 2021, in preparation). If $P_{\text{tot}}(0) \approx \Delta P \approx \mathcal{W}$, we then have $\Sigma_{\text{SFR}} = \mathcal{W}/\Upsilon$ using the

total feedback yield Υ . In the pressure-regulated, feedback-modulated theory, Υ then controls the star formation rate, with thermal+turbulent+magnetic terms yielding $\Upsilon \sim 10^3\text{ km s}^{-1}$ for the solar neighborhood model (Kim & Ostriker 2017).

In principle, CR pressure could also contribute to the vertical support of the disk, and in doing so participate in regulating the star formation rate. However, it is important to note that only the *difference* ΔP between midplane and high-altitude pressure contributes to vertical support against gravity in the ISM. For the thermal, kinetic, and magnetic pressure, the high altitude ($\sim 0.5\text{ kpc}$) values are very small compared to the midplane values, so that ΔP is essentially the same as the midplane value. For the CRs, in contrast, the pressure is nearly uniform within the neutral gas layer (see Figures 13, 16, 17) because ion-neutral collisions dampen resonant Alfvén waves, keeping the scattering rate quite small. As a consequence, $\Delta P_c \ll P_c(0)$, and the contribution of CRs to supporting the ISM weight is expected to be small. As a consequence, CRs would also not contribute to the control of star formation on $\sim\text{kpc}$ scales; Υ_c would not be included in the total Υ that is used to predict the SFR via $\Sigma_{\text{SFR}} = \mathcal{W}/\Upsilon$.

The fact that the midplane CR pressure is a factor of $\sim 5\text{--}8$ larger than observed Milky Way values is in part because all pressures are slightly enhanced in this particular TIGRESS simulation compared to the solar neighborhood. Fine-tuning of the adopted galactic model, together with the inclusion of ionizing radiation feedback to create H II regions, could reduce this. However, the CR pressure is more enhanced than other pressures. One possible reason for this is that the TIGRESS MHD simulation does not self-consistently include CRs. For the reasons explained above, we do not expect that inclusion of CRs in the MHD simulation would appreciably reduce the SFR. However, there could potentially be a significant difference in the magnetic structure at high altitude. Figure 8 shows that there is generally a very large CR pressure gradient between the mostly neutral midplane gas and the surrounding corona. Figure 2 shows that the magnetic field is preferentially horizontal in the midplane gas, and Figures 7 and 16 show that magnetic geometry and low perpendicular diffusion can significantly limit CR transport. It is likely that if the back-reaction of the CR pressure on the gas were included, the strain would cause the magnetic field lines at high altitude to open up in the direction perpendicular to the disk (Parker 1969). This rearrangement of magnetic field topology would enable CRs that would otherwise be trapped in the ISM to stream and diffuse out of the disk along the magnetic field lines, leading to a significant decrease in the CR pressure near the midplane.

With fully time-dependent simulations, we will be able to determine whether the CR pressure is reduced to be closer to the other pressures. If this is not the case, it would instead suggest that modification of the scattering rate coefficients (see Section 2.2.3) is required. Considering the case with $\sigma_\perp = 10\sigma_\parallel$, we find that an increase of the damping rates (Equations (16) and (18)) or a reduction of the Alfvén wave growth rate (Equation (15)) by a factor of ~ 10 would be required for the CR pressure to be consistent with the other pressures near the midplane. In fact, recent MHD-PIC simulations of nonlinear streaming instability and quasi-linear diffusion with local damping suggest an effective scattering rate of about half of the traditional theoretical value $(\pi/8)(\delta B/B)^2 \Omega$ (Bambic et al. 2021), already alleviating some of the tension.

Finally, it is worth pointing out that the observed CR pressure in the Milky Way is effectively a single evolutionary snapshot of the solar neighborhood, while the CR pressures shown in Figures 14 and 16 are the result of temporal averaging. Hence, the comparison with observations should be taken with a grain of salt. For example, if we consider the individual snapshot at $t=536$ Myr for the model with $\sigma_{\perp} = 10\sigma_{\parallel}$, the midplane CR energy density is 1.5 eV cm^{-3} , in good agreement with the observed value of $\sim 1 \text{ eV cm}^{-3}$.

6.2. CR Pressure versus Magnetic Pressure

In this section, we investigate the relation between CR pressure and magnetic pressure. Pressure equality (or energy density equipartition) between CRs and magnetic fields is commonly assumed in order to infer the magnetic field strength from synchrotron observations of star-forming galaxies (e.g., Longair 1994; Beck & Krause 2005). An argument used to justify the equipartition assumption is that CRs and magnetic fields have a common source of energy. While the former are accelerated in supernova shocks, the latter are amplified by ISM turbulence, which, in turn, is driven by supernova feedback. Another argument for equipartition derives from the fact that CRs are confined by magnetic fields; a CR pressure exceeding the magnetic pressure would not be able to maintain this confinement. However, while the above and related arguments suggest a relationship should exist between magnetic and CR pressure, there is no robust physical reason to support the assumption of equipartition, especially on local scales.

In practice, observational evidence shows that in Milky Way-like galaxies, CR, and magnetic pressures in midplane gas are similar on scales $\gtrsim 1$ kpc. However, there are some observational signatures, supported by recent MHD simulations (Seta & Beck 2019), showing that pressure equality is unlikely on spatial scales of the order of 100 pc (Stepanov et al. 2014). The discrepancy between CR pressure and magnetic pressure is even stronger in starburst galaxies, where the magnetic energy density is significantly larger than the CR energy density (Yoast-Hull et al. 2016).

Here, we use the outcomes of the self-consistent model for high-energy CRs to evaluate the median ratio of CR pressure P_c and magnetic pressure P_m as a function of hydrogen density n_H (see Figure 22). Clearly, the assumption of pressure equality is not valid for most of the ISM. The median value of P_c/P_m decreases with increasing the density: it is orders of magnitude above unity at low densities ($n_H \lesssim 10^{-2} \text{ cm}^{-3}$) and decreases below unity at $n_H > 1 \text{ cm}^{-3}$.

At the average midplane density of the ISM ($n_H \approx 0.1\text{--}1 \text{ cm}^{-3}$), the median ratio is $\sim 3\text{--}30$. This explains why the average CR pressure and magnetic pressure become comparable near $z \simeq 0$ in our model (see right panel of Figure 14) and to some extent justifies traditional premises for interpreting synchrotron emission when averaged on kpc scales. At higher densities, the magnetic pressure is higher than the CR pressure. Indeed, while the latter is completely uniform for $n_H > 10^{-1} \text{ cm}^{-3}$ (see Figure 12), the former increases in the densest parts of the ISM undergoing gravitational collapse. The median value of P_c/P_m is $\simeq 0.1$ in regions with $n_H \simeq 10^2 \text{ cm}^{-3}$,

⁹ The magnetic pressure P_m is calculated as $(B_x^2 + B_y^2 + B_z^2)/8\pi$. Note that the magnetic pressure is always higher than the vertical magnetic stress ($P_{m,z} = (B_x^2 + B_y^2 - B_z^2)/8\pi$) discussed in the rest of this paper. For an isotropic magnetic field, the ratio would be a factor of 3.

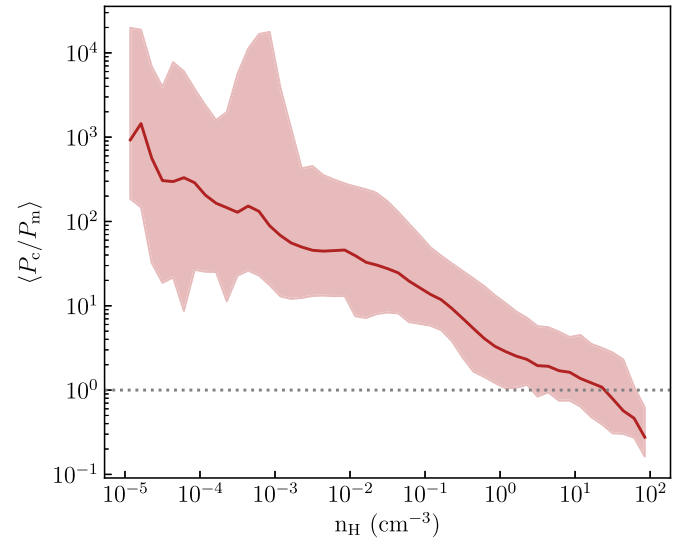


Figure 22. Temporally averaged median of the ratio between CR pressure P_c and magnetic pressure P_m as a function of hydrogen density n_H for the model with variable σ_{\parallel} and no diffusion perpendicular to the magnetic field direction. The shaded area covers the temporally averaged 16th and 84th percentile variations around the median profile. The dotted line indicates equal pressure.

whose typical size scale is $\lesssim 100$ pc (see Figure 2). This result is in agreement with what found by Stepanov et al. (2014) in the Milky Way, M31, and the LMC, i.e., that when measured on spatial scales of the order of 100 pc, the magnetic energy density is larger than what was expected from the assumption of pressure equality. Also, the variation of P_c/P_m by almost one order of magnitude around the median value indicates the lack of a strict correlation between P_c and P_m at every density. Observed synchrotron emission is of course produced by relativistic electrons rather than the CR protons studied here, but our results serve as a caution in assuming pressure equality (or correlation) to infer local properties of the magnetic field from synchrotron observations.

6.3. Comparison with Other Works

As mentioned in Section 1, many numerical studies have aimed to constrain the propagation of CRs on galactic scales with direct measurements of CR energy density in our Galaxy. These works generally assume temporally and spatially constant isotropic diffusion and often ignore the presence of CR advection (e.g., Trotta et al. 2011; Cummings et al. 2016; Jóhannesson et al. 2016). They find that the isotropically averaged scattering coefficient required to match the observed CR spectrum is of the order of $10^{-28}\text{--}10^{-29} \text{ cm}^{-2} \text{ s}$. At face value, these numbers appear to agree with our finding that, under the assumption of spatially constant scattering, a value of $\sigma_{\parallel} \sim 10^{-29} \text{ cm}^{-2} \text{ s}$ is required for the CR pressure to be comparable with the other relevant pressures near the galactic plane (see Figure 11) as observed in the solar neighborhood. However, we have also seen that advection by fast-moving magnetized gas is crucial for transporting CRs out of the disk (Section 3.2.1). In propagation models ignoring advection, the primarily horizontal magnetic field near the midplane makes the value of the perpendicular diffusion coefficient more important than the parallel coefficient; Figures 5 and 7 show that $\sigma_{\perp} \sim 10^{-29} \text{ cm}^{-2} \text{ s}$ is required for the midplane CR pressure to be comparable to other pressures. While this essentially agrees with the results of traditional models that assume

isotropic diffusion, it also points out their serious physical flaw: first, the value $\sigma_{\perp} \sim 10^{-29} \text{ cm}^{-2}$ is unrealistically low, and second, in our simulations advection is actually playing the role imputed to perpendicular diffusion.

An important difference between our models without CR advection and those mentioned above is that, while the latter makes use of simplified analytic prescriptions to model the gas distribution within the Milky Way, in our model the background gas distribution is that predicted by the TIGRESS simulation of our solar neighborhood. The high resolution and the sophisticated physics included in TIGRESS allow for accurate reproduction of the multiphase star-forming ISM. A realistic distribution of the background thermal gas and the magnetic field is crucial for detailed modeling of the CR propagation. For example, the analysis of our models without advection has shown that CRs can be easily trapped in regions with either highly tangled magnetic fields with relatively high Alfvén speed (at high altitude) or with primarily horizontal magnetic fields (near the midplane). This explains why (unrealistically) low perpendicular scattering coefficients are required for the CR pressure to decrease to the observed values. If we neglected the real structure of the magnetic field and assumed open magnetic field lines, as usually done in analytic models of CR propagation, CRs would easily stream outward, and the needed parallel scattering coefficients would be higher.

Another shortcoming of most models is that they ignore the dependence of the scattering coefficient on the properties of the background gas. In Section 4, we have seen that in realistic models with nonuniform scattering, σ_{\parallel} is relatively high in the ionized gas, while it rapidly decreases with the increase of density in the neutral gas. In the ionized gas that dominates the volume outside the midplane, the average value of σ_{\parallel} (a few $\times 10^{-28} \text{ cm}^{-2} \text{ s}$) is higher than that predicted by simple diffusive models of CR propagation in the Milky Way. In contrast, in the neutral gas, the scattering rates are far lower than in simple constant diffusion models, and this low scattering leads to a very smooth CR distribution in the midplane. Furthermore, the actual value of the CR pressure in the neutral gas is not set by local transport, but the efficiency of CR propagation in the surrounding ionized gas. One can think of the gaseous disk as composed of a thinner layer of warm/cold neutral gas surrounded by a thicker layer of warm and hot ionized gas. If the transport of CRs is slow in the ionized gas, CRs remain trapped in the neutral gas, even though the local diffusivity is extremely large.

It is also interesting to compare our results to those of Hopkins et al. (2021) based on cosmological zoom-in FIRE simulations (Hopkins et al. 2018) with CRs. The authors explore a variety of models, from some assuming constant scattering to more realistic models based either on the self-confinement or on the extrinsic turbulence picture. Their results are generally similar to ours, while differing in some details. In common with our conclusions, they find that there is no single diffusivity that characterizes transport, with the ISM phase structure leading to orders of magnitude variation. They also find, as we have emphasized based on our models, that rapid transport of CRs in the neutral gas is not the main limitation on CR residence times (and CR pressure) in dense gas. Rather, the main confinement of CRs is provided by the surrounding ionized gas. Also, from the analysis of their simulations of Milky Way-like galaxies assuming constant scattering, they find that $\sigma_{\parallel} \sim 10^{-29} \text{ cm}^{-2} \text{ s}$ is required to match the CR energy

density $e_c \sim 1 \text{ eV cm}^{-3}$ measured in the solar neighborhood, similar to the results shown in the right panel of our Figure 11.

To our knowledge, Hopkins et al. (2021) is the only work to date that has tested transport with a variable scattering model based on self-confinement, and our self-consistent model without perpendicular diffusion is most similar to their default self-confinement model. However, it should be noted that there are some non-negligible differences between our and the Hopkins et al. (2021) model. One difference regards the damping processes taken into account to compute σ_{\parallel} (see Section 2.2.3). While we consider ion-neutral and nonlinear Landau damping only, Hopkins et al. (2021) also include turbulent and linear Landau damping in their calculations. Depending on the conditions of the background thermal gas, the addition of damping mechanisms may reduce the growth of Alfvén waves, and, as a consequence, the CR scattering rate. Another difference is in the procedure to calculate n_1 in Equations (17) and (19). Hopkins et al. (2021) approximate n_1 with e_c/E , where E is equal to 1 GeV. However, deriving n_1 from a realistic CR spectrum, we find that its actual value is almost one order of magnitude lower than e_c/E . This results in a lower normalization of the scattering coefficient (a factor of $\sqrt{10}$ when $\Gamma_{\text{nl}} > \Gamma_{\text{in}}$ and a factor of 10 when $\Gamma_{\text{nl}} < \Gamma_{\text{in}}$) in our work. Also, to derive the ion number density in Equations (17) and (19), we calculate the ionization fraction in the primarily neutral gas based on the low-energy cosmic-ray ionization rate, which is not implemented by Hopkins et al. (2021). Since Hopkins et al. (2021) report CR energy density averaged over radial shells but not the corresponding thermal, turbulent, or magnetic pressures (or values of Σ_{SFR}), it is difficult to make detailed comparisons. However, we can note that the midplane CR pressure in our work is less than a factor of 2 lower than that found in their self-confinement model at $R = 8 \text{ kpc}$.

6.4. CR Spectrum and Ionization Rate in the ISM

As discussed in Section 2.2.4, the low-energy slope of the CR spectrum in the solar neighborhood is highly uncertain. A simple extrapolation of the Voyager 1 data down to energies of 1 MeV predicts $\delta \approx 0.1$. However, this value fails to reproduce the rate of CR ionization measured in nearby diffuse molecular clouds ($n \approx 100 \text{ cm}^{-3}$, $T \approx 100 \text{ K}$). Padovani et al. (2018) found that δ must be $\simeq -0.8$ at the edges of the clouds in order to match the inferred ζ_c based on abundances of molecular ions (Neufeld & Wolfire 2017). As low-energy CRs penetrate the dense clouds, they lose a significant portion of their energy due to collisional interactions with the surrounding gas. Therefore, the low-energy slope of the spectrum tends to increase from the initial value (becoming flatter). Following Padovani et al. (2018), Silsbee & Ivlev (2019) tried to constrain the value of δ using alternative models of CR propagation. They confirmed the value of -0.8 under the assumption of free streaming, as in Padovani et al. (2018). However, they found that the low-energy slope decreases to $\delta = -1.0$ for the model where CRs freely stream along magnetic field lines above a given column density and are scattered by MHD waves below such threshold, and to $\delta = -1.2$ under the assumption of pure scattering. In Section 5, we have found that low-energy CRs freely stream along the magnetic field lines at the typical densities of diffuse molecular clouds (see Figure 20), suggesting that the transport model proposed by Padovani et al. (2018) is more representative of the actual propagation of CRs at high gas densities.

In Section 5.4, we have used the predictions of our self-consistent models for the propagation of high- and low-energy CRs to constrain the low-energy slope of the injected CR spectrum, δ_{inj} , which is an input for our models. Our choices for δ_{inj} correspond to an assumption for the fraction of supernova energy going into the production of CRs with energies of about 30 MeV. We have explored three different values of δ_{inj} : $\delta_{\text{inj}} = -0.8$, in agreement with Padovani et al. (2018), $\delta_{\text{inj}} = 0.1$, in agreement with the low-energy slope extrapolated from the Voyager spectrum, and $\delta_{\text{inj}} = -0.35$, an intermediate value between -0.8 and 0.1 . We have then computed the local value of δ from the local energy density of both low-energy and high-energy CRs (Equation (23)) and inferred the corresponding CR ionization rate. Comparing the CR ionization rates predicted by the three models for low-energy CRs with the CR ionization rate measured in diffuse molecular clouds, we find that a value of $-0.8 < \delta_{\text{inj}} < -0.35$ is required to reproduce the observations. A significantly higher/lower value would result in a CR ionization rate below/above the observed range of values.

We caution that our simulations lack the resolution to capture structures with densities above $\sim 100 \text{ cm}^{-3}$. As the rate of collisional losses increases with the gas density, we expect the attenuation of CRs energy density and flux to be stronger should the internal structure of individual clouds be resolved. As a consequence, the CR ionization rate might be lower than that shown in Figure 21 for a given choice of δ_{inj} , likely making the model assuming $\delta_{\text{inj}} = -0.8$ more realistic than the model assuming $\delta_{\text{inj}} = -0.35$.

7. Final Summary

This work investigates the propagation of CRs in a galactic environment with conditions similar to the solar neighborhood, taking into account a realistic spatial distribution of multiphase gas density, velocity, and magnetic field. For this purpose, we extract a set of snapshots from a TIGRESS MHD simulation (Kim & Ostriker 2017; Kim et al. 2020a) with spatial resolution $\Delta x = 8 \text{ pc}$ and postprocess them using the algorithm for CR transport implemented in *Athena++* by Jiang & Oh (2018). By comparing to postprocessed TIGRESS simulations with the same conditions at both higher and lower resolution, we demonstrate that a resolution $\Delta x \leq 16 \text{ pc}$ is required to achieve convergence of the CR properties analyzed in this paper (see Figure 26).

We consider a wide range of CR transport models, from simple models including either diffusion or streaming only, to models including both diffusion and streaming but neglecting advection, to models including advection. We first consider models in which the diffusivity is spatially constant, and analyze the effect of different choices of the scattering coefficient. We then explore the physically motivated case in which the scattering coefficient varies spatially. The properties of the background gas and spatial distribution of CRs enter together in determining the scattering rate coefficient, under the assumption that CRs are scattered by streaming-driven Alfvén waves and that the wave amplitude is set by the balance of growth and damping (considering both ion-neutral damping and nonlinear Landau damping). We separately evaluate the transport of CRs with kinetic energies of $\sim 1 \text{ GeV}$ (high-energy CRs) and $\sim 30 \text{ MeV}$ (low-energy CRs), respectively important for the dynamics and for the ionization of the ISM.

Our main conclusions are as follows:

1. Advection by fast-moving, hot gas plays a key role in removing CRs from the disk. Streaming and diffusion parallel to the magnetic field are relatively ineffective in transporting CRs from the midplane to the coronal region, since magnetic field lines are mainly oriented in the x – y direction near the midplane in the warm gas, while the Alfvén speed is low in hot superbubbles (Figure 10). In transport models neglecting advection, diffusion perpendicular to the magnetic field direction becomes crucial for the propagation of CRs (Figure 7). In the absence of advection and for the case of spatially constant diffusivity, we find that scattering coefficients $\sigma_{\parallel} \lesssim \sigma_{\perp} \sim 10^{-29} \text{ cm}^{-2} \text{ s}$ are required for the CR pressure to be in equipartition with thermal, kinetic, and magnetic pressure near the Galactic plane (Figure 5). In contrast, a value of $\sigma_{\parallel} \sim 10^{-29} \text{ cm}^{-2} \ll \sigma_{\perp} \text{ s}$ is sufficient to reach pressure equipartition in the presence of advection (Figures 9 and 11).
2. There is no single diffusivity. For our variable-diffusion model, the scattering coefficient varies over more than four orders of magnitude depending on the properties of the ambient gas (left panel of Figure 14, and fourth panel from the left of Figure 13). Clearly, realistic spatial and thermal distributions of the background gas, as well as an accurate calculation of the ionization state, are crucial for the proper computation of σ_{\parallel} . For high-energy CRs, we find that σ_{\parallel} is roughly constant and relatively high ($\simeq 10^{-28} \text{ cm}^{-2} \text{ s}$) in low-density regions ($n_{\text{H}} < 10^{-2} \text{ cm}^{-3}$) where nonlinear Landau damping dominates. The scattering rate coefficient decreases to very low values ($\ll 10^{-29} \text{ cm}^{-2} \text{ s}$) in higher-density regions ($n_{\text{H}} > 10^{-1} \text{ cm}^{-3}$) of primarily neutral gas where ion-neutral damping dominates. The maximum value of σ_{\parallel} ($\simeq 10^{-27} \text{ cm}^{-2} \text{ s}$) is reached at intermediate gas densities ($n_{\text{H}} \sim 10^{-2} \text{ cm}^{-3}$), at the interface between neutral and fully ionized gas.
3. Diffusion and streaming regulate the propagation of CRs within most of the ISM. Our physically motivated model accounting for variable σ_{\parallel} predicts that diffusion largely dominates over advection in the higher-density, lower-temperature gas that comprises most of the mass of the ISM (Figure 15). Gas velocities are high in the hot gas but much lower in the warm/cold gas, while at the same time ion-neutral damping in these phases keeps the scattering coefficient low. The higher-density regions are also characterized by the highest values of streaming velocity, since the relatively high value of the magnetic field and low ion density leads to a high ion Alfvén speed. With ionization fraction $x_i \sim 0.01$ – 0.1 determined by the CR ionization rate, the ion Alfvén speed of 50 – 100 km s^{-1} exceeds the advection speed of $\sim 10 \text{ km s}^{-1}$ (see the third panel from the left of Figure 13). Still, the mass-weighted diffusion speed exceeds the mass-weighted streaming speed for GeV CRs.
4. The overall distribution of CRs depends on how effective their propagation is in the low-density gas. Even though the scattering rate is very low within most of the ISM’s mass near the midplane, CRs are strongly confined within this region. CR transport out of the midplane is limited by the high scattering rate in surrounding lower-density, hotter, higher-ionization gas. As a consequence, the

overall CR distribution is in better agreement with uniform diffusivity models (including advection) that have relatively high $\sigma_{\parallel} \sim 10^{-27} - 10^{-28} \text{ cm}^2 \text{ s}$, rather than models with values of the scattering coefficient similar to local values in the neutral gas (right panel of Figure 14). In realistic models, the CR pressure is strongly phase-dependent and CRs are extremely uniform at densities above $n_{\text{H}} \sim 0.1 \text{ cm}^{-3}$, while the constant diffusion models with advection have a range of CR pressure at high density (Figure 17). In contrast, constant diffusion models without advection have smooth CR distributions across all phases, and the correlation of CR pressure with gas density is a side effect of preferential CR deposition near the midplane where star formation and supernovae are concentrated (Figure 12).

5. Low-energy CRs have less effective diffusion and more significant collisional losses compared to high-energy CRs. Even though the scattering coefficient distribution as a function of gas density is qualitatively similar for high- and low-energy CRs, the value of σ_{\parallel} at a given density increases with decreasing kinetic energy. Also, for low-energy CRs, the scattering coefficient depends somewhat on the low-energy slope of the injected energy spectrum of CRs (left panel of Figure 18). We find that σ_{\parallel} increases with decreasing slope (steepening spectrum). In addition to different diffusion, high- and low-energy CRs undergo different energy losses via interaction with the ambient gas since the rate of collisional losses is more than a factor of 2 larger for low-energy CRs. For low-energy CRs, the fraction of energy losses increases for a steeper spectral slope since CRs are trapped in the dense gas for a longer time when the scattering rate is higher, thus losing more energy.
6. Streaming exceeds diffusion for low-energy CRs (Figure 20). Since diffusion is less effective for low-energy CRs, their average streaming velocity is higher than their average diffusion velocity at $n_{\text{H}} \sim 0.1 - 1 \text{ cm}^{-3}$. Diffusion becomes dominant for $n_{\text{H}} > 10 \text{ cm}^{-3}$. At $n_{\text{H}} \sim 10 - 100 \text{ cm}^{-3}$, the mean free path of both high- and low-energy CRs is comparable to the size of diffuse cold atomic/molecular clouds (right panel of Figure 18), meaning that CRs freely stream across them, subject to collisional energy losses only.

Although this paper has not directly studied dynamical effects of CRs in galaxies, our results have implications that are highly relevant to ISM dynamics. First, considering that the CR distribution in our physically motivated model is extremely uniform in primarily neutral gas, our results predict that CR pressure gradient forces are negligible compared to the other forces associated with thermal pressure and Reynolds and Maxwell stresses. We therefore expect CRs not to contribute significantly to the dynamical equilibrium of the ISM gas, or to immediate regulation of star formation rates. Nevertheless, CR pressure gradients are very large at the interface between the mostly neutral disk and the surrounding lower-density corona, suggesting that CRs may significantly contribute to the gas dynamics of this region, including driving galactic winds (which regulate star formation over long timescales). Clearly, fully self-consistent simulations with MHD and CRs are required to corroborate our expectations.

Because low-energy CRs suffer greater collisional losses than high-energy CRs, the “evolved” spectrum tends to be

flatter than the injection spectrum. This is partly offset by the higher scattering rates for low-energy CRs, which trap them more effectively than high-energy CRs. Even so, the local low-energy spectrum is always flatter than the injection spectrum. Although our models do show the expected trend of decreasing low-energy CR density in dense gas (here, at $n_{\text{H}} \gtrsim 3 \text{ cm}^{-3}$), our limited resolution does not allow us to constrain the spectrum based on differential CR ionization with density. Nevertheless, our models do suggest that a slope of the low-energy CR spectrum similar to $\delta \sim -0.5$ would be compatible with observed ionization rates. A steeper slope would produce excess ionization, while a flatter slope would produce insufficient ionization. Simulations at higher resolution, with self-consistent dynamics, will be needed to test and refine these conclusions.

We thank the anonymous referee for valuable comments and suggestions. We are grateful to Chang-Goo Kim and Munan Gong for sharing their expertise and technical tools. This work was supported in part by grant 510940 from the Simons Foundation to E. C. Ostriker, and in part by Max-Planck/Princeton Center for Plasma Physics (NSF grant PHY-1804048). Computational resources were provided by the Princeton Institute for Computational Science and Engineering (PICSciE) and the Office of Information Technology’s High Performance Computing Center at Princeton University. The Center for Computational Astrophysics at the Flatiron Institute is supported by the Simons Foundation.

Appendix A Cosmic-ray Spectrum Dependence

A.1. Relation Between n_1 and n_c and Dependence on Low-energy Spectral Slope δ

Figure 23 shows the trend of n_1 (Equation (14)) as a function of $E_k = (c^2 p_1^2 + (mc^2)^2)^{1/2} - mc^2$ for three different values of δ for the low-energy slope of the CR energy flux spectrum (Equation (21)). To normalize, n_1 is divided by $e_c(E_k \geq E_t)/(1 \text{ eV})$, with $e_c(E_k \geq E_t)$ the total energy density of CRs with kinetic energies above the break of the spectrum E_t . Clearly, different choices of δ affect the trend of n_1 only at low kinetic energy, where the three curves diverge at low energy. The value of n_1 at given energy increases with decreasing (more negative) δ . For example, at $E_k = 30 \text{ MeV}$, the value of n_1 at $\delta = -0.8$ is nearly one order of magnitude larger than the value of n_1 at $\delta = 0.1$. At kinetic energies above E_t , the value of n_1 is almost independent of δ .

To calculate the value of σ_{\parallel} (Equations (17) and (19)) for high-energy CRs, we adopt the value of n_1 at $E_k = 1 \text{ GeV}$, that is $\sim 10^{-10} e_c(E_k \geq E_t)/(1 \text{ eV}) \text{ cm}^{-3}$ (which is extremely insensitive to δ .) We note that the value of n_1 at $E_k = 1 \text{ GeV}$ is a factor of ~ 3 lower than the value of n_1 at $E_k = 30 \text{ MeV}$ for $\delta = 0.1$; this becomes more than a factor of 10 for $\delta = -0.8$. As a result, the normalization for the scattering coefficient is lower for high-energy CRs compared to low-energy CRs in all the transport models analyzed in this paper.

For reference, the dashed lines in Figure 23 show the CR number density $n_c(>E_k) = 4\pi \int_{p_1}^{\infty} F(p) p^2 dp$ as a function of E_k for the same three choices of δ . The trend of n_c is the same as n_1 at high kinetic energy, where the spectrum follows a power-law distribution ($j(E_k) \sim CE_k^{-2.7}$, $F(p) \sim Cp^{-4.7}$). Here, $n_1 = n_c(>E_k)(3+r)/(2+r)$, where $r = -4.7$ is the high-

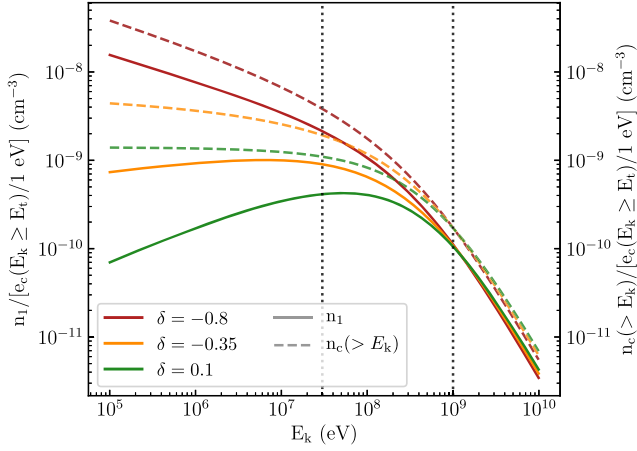


Figure 23. Trend of n_1 (solid lines) and $n_c(> E_k)$ (dashed lines) as a function of $E_k = [(cp_i)^2 + (mc^2)^2]^{1/2} - mc^2$ for different low-energy slopes in the adopted CR spectral form (Equation (21)): $\delta = 0.1$ (green lines), $\delta = -0.35$ (orange lines), and $\delta = -0.8$ (red lines). To normalize we divide n_1 and n_c by $e_c(E_k \geq E_t)/1 \text{ eV}$, where this is the total energy density of CRs with kinetic energies above $E_t = 650 \text{ MeV}$. The dotted vertical lines indicate where $E_k = 30 \text{ MeV}$ and $E_k = 1 \text{ GeV}$.

energy slope of $F(p)$. At low kinetic energy, the trends of n_c diverge with decreasing energy. Of course, unlike n_1 , n_c monotonically increases toward lower energy.

A.2. Dependence of ζ_c on δ and $E_{k,\min}$

The dependence of the primary CR ionization rate per hydrogen atom (Equation (25)) on the low-energy slope of the CR spectrum is displayed in Figure 24, showing the value of ζ_c as a function of $P_c(E_k \geq E_t)/k_B$ for three different choices of δ . ζ_c linearly increases with $P_c(E_k \geq E_t) = e_c(E_k \geq E_t)/3$, which enters in the calculation of ζ_c through the spectrum normalization C (Equation (22)). At a given CR pressure, the value of ζ_c increases with decreasing δ since this corresponds to an increase in the number density of low-energy CRs which ionize the ambient gas (see dashed lines in Figure 23). The solid lines denote the value of ζ_c obtained adopting $E_{k,\min} = 10^5 \text{ eV}$ in Equation (25) (our default assumption), while the lower and upper boundaries of the shaded area indicate the value of ζ_c obtained adopting $E_{k,\min} = 10^6 \text{ eV}$ and $E_{k,\min} = 10^4 \text{ eV}$, respectively.

The variation of ζ_c with $E_{k,\min}$ significantly depends on δ . At a given CR pressure, the value of ζ_c varies by less than a factor of 2 when $\delta = 0.1$, but by more than one order of magnitude when $\delta = -0.8$. This can be understood based on the dashed lines in Figure 23. For $\delta = 0.1$, there is a negligible increase in the CR number density toward lower E_k below $E_k \sim 10^6 \text{ eV}$, whereas for $\delta = -0.8$ there is a very large increase. This means the additional ionization from CRs with energies below 10^6 eV is negligible for a CR distribution with $\delta = 0.1$, while it is significant for a CR distribution with $\delta = -0.8$. A value of ζ_c comparable to the observed CR ionization rate ($\zeta_c \simeq 1.8 \times 10^{-16} \text{ s}^{-1}$, e.g., Padovani et al. 2020) can be recovered for P_c/k_B in the range $\sim 4\text{--}10 \times 10^3 \text{ cm}^{-3} \text{ K}$ (similar or slightly larger than solar neighborhood estimates) by the model with $\delta = -0.35$ for $E_{k,\min} \sim 10^4\text{--}10^5 \text{ eV}$ or by the model with $\delta = -0.8$ for $E_{k,\min} \gtrsim 10^6 \text{ eV}$.

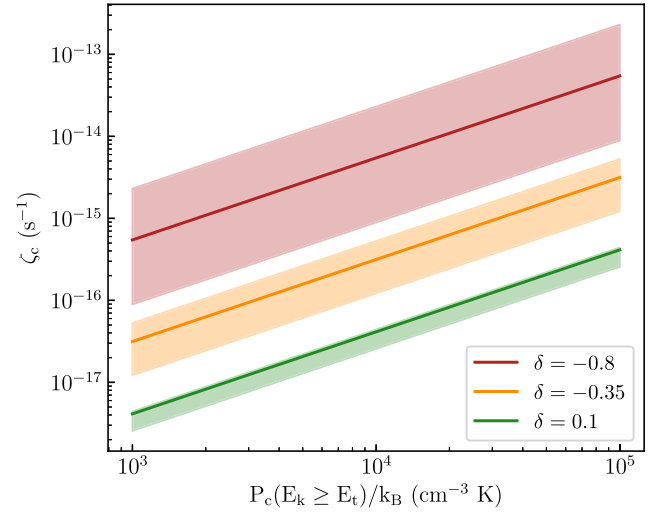


Figure 24. Trend of the primary CR ionization rate per hydrogen atom ζ_c as a function of the total pressure P_c/k_B of high-energy CRs ($E_k \geq E_t = 650 \text{ MeV}$) for $\delta = 0.1$ (green line), $\delta = -0.35$ (orange line), $\delta = -0.8$ (red lines). The solid line is obtained adopting $E_{k,\min} = 10^5 \text{ eV}$ in Equation (25). The lower and upper boundaries of the shaded area indicate the value of ζ_c obtained adopting $E_{k,\min} = 10^6 \text{ eV}$ and $E_{k,\min} = 10^4 \text{ eV}$, respectively.

A.3. Propagation Models for High-energy CRs Assuming Different δ

The self-consistent model shown in Section 4 for high-energy CRs is based on the assumption that the low-energy slope of the CR energy spectrum is $\delta = -0.35$. Here, we compare the results of the default model with those obtained for different choices of δ , i.e., $\delta = -0.8$ and $\delta = 0.1$. The left panel of Figure 25 shows that the average vertical profiles of CR pressure are almost independent of the value of δ . The three profiles are nearly identical except for a slight tendency to become steeper with decreasing δ . We can note, for example, that at low latitudes ($|z| \lesssim 1 \text{ kpc}$), the CR pressure slightly increases with decreasing δ .

To understand this behavior, we must consider how the roles of diffusion and streaming change with δ . We recollect that both the scattering coefficient (relevant for the calculation of the diffusive flux), and the ion Alfvén speed (relevant for the calculation of the streaming flux), depend on the ion number density. In particular, $\sigma_{\parallel} \propto n_i^{-0.5}$ when $\Gamma_{\text{in}} > \Gamma_{\text{nl}}$, and $\sigma_{\parallel} \propto n_i^{-0.25}$ when $\Gamma_{\text{in}} < \Gamma_{\text{nl}}$, while $v_{A,i} \propto n_i^{-0.5}$. In turn, the ion number density depends on the rate of CR ionization, which is a function of δ (see Appendix A.2). A decrease of the low-energy slope of the CR spectrum entails an increase of the number of low-energy CRs, and, as a consequence, an increase of the ionization rate. In the low-density regime, both σ_{\parallel} and $v_{A,i}$ must be similar for the three models since most of the gas is already ionized ($n_i \simeq n_H$) and the effect of different CR ionization rates is negligible. In the intermediate/high-density regime, where gas is partially or mostly neutral, we expect that the diffusive flux to increase with decreasing δ ($F_{d,\parallel} \propto 1/\sigma_{\parallel}$), and the streaming flux to decrease with decreasing δ .

In the right panel of Figure 25, the solid lines indicate the average particle-wave interaction coefficient along the magnetic field direction, $\sigma_{\text{tot},\parallel}$, as a function of hydrogen density for the three different choices of δ . In the same plot, we use the dashed and dotted lines to indicate the average trend of the scattering coefficient σ_{\parallel} and of the streaming coefficient σ_{stream} .

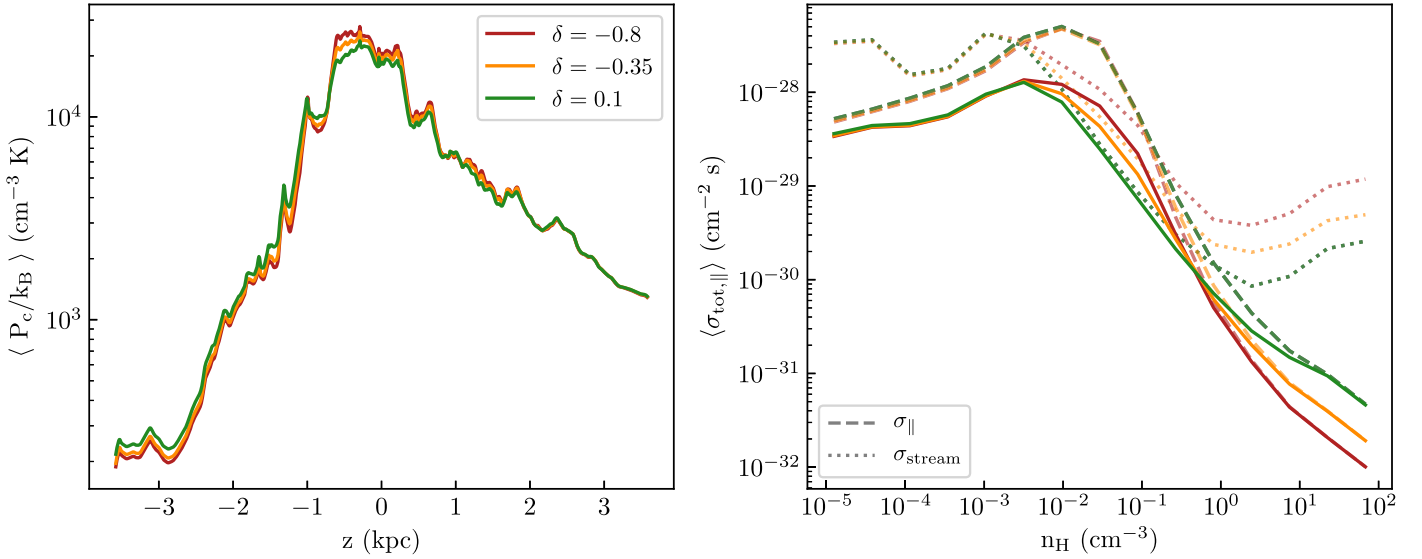


Figure 25. Comparison of self-consistent propagation models for high-energy CRs assuming a different low-energy slope of the CR spectrum, $\delta = -0.8$ (red lines), $\delta = -0.35$ (orange lines) and $\delta = 0.1$ (green lines). Left panel: horizontally averaged vertical profiles of CR pressure. Right panel: average particle-wave coefficients in the direction parallel to the mean magnetic field, $\sigma_{\text{tot},\parallel}$, as a function of hydrogen density n_H . The dashed and dotted lines indicate the average scattering coefficients σ_{parallel} and streaming coefficients σ_{stream} as a function of n_H , respectively. σ_{stream} is calculated as the inverse of the second term on the rhs of Equation (4) ($1/\sigma_{\text{tot},\parallel} = 1/\sigma_{\parallel} + 1/\sigma_{\text{stream}}$). The analysis is performed on the snapshot at $t = 286$ Myr.

The latter is defined as the inverse of the second term on the rhs of Equation (4) ($1/\sigma_{\text{tot},\parallel} = 1/\sigma_{\parallel} + 1/\sigma_{\text{stream}}$), $1/\sigma_{\text{stream}} \sim v_{A,i}H$. As anticipated above, both σ_{\parallel} and σ_{stream} are independent of the choice of δ for $n_H \lesssim 10^{-3} \text{ cm}^{-3}$. At higher density, σ_{stream} increases with decreasing δ , while σ_{\parallel} remains independent of δ up to $n_H \lesssim 10^{-1} \text{ cm}^{-3}$ and then decreases with decreasing δ .

The transition from the streaming-dominated to the diffusion-dominated regime slightly varies with δ : it happens at $n_H \sim 0.1 \text{ cm}^{-3}$ for $\delta = -0.8$ and at $n_H \sim 1 \text{ cm}^{-3}$ for $\delta = 0.1$. In Section 4, we have seen that the overall distribution of CR pressure is regulated by the efficiency of CR propagation in the low-to-intermediate density gas: the less effective the CR propagation in these regions the more CRs are trapped in higher-density regions. In the intermediate-density regime ($n_H \simeq 0.01\text{--}0.1 \text{ cm}^{-3}$) $\sigma_{\text{stream}} > \sigma_{\parallel}$, meaning that streaming dominates over diffusion ($F_s = |\hat{\mathbf{B}} \cdot \nabla P_c|/\sigma_{\text{stream}} = (4/3)e_c v_{A,i} > F_{d,\parallel} = |\hat{\mathbf{B}} \cdot \nabla P_c|/\sigma_{\parallel}$). The higher CR pressure near the midplane and the steeper profiles predicted by models with lower δ can therefore be explained by the less effective CR streaming at intermediate densities. However, we note that while the variation in σ_{stream} increases with n_H , the variation in $\sigma_{\text{tot},\parallel}$ —which determines the total flux in the wave frame—decreases as diffusion becomes more important. In the intermediate-density regime, the average variation in $\sigma_{\text{tot},\parallel}$ is much lower than that in σ_{stream} and this explains why the vertical CR pressure profile is only weakly dependent on δ .

Appendix B Sensitivity to Numerical Resolution

In this section, we conduct studies to verify the robustness of our results to the numerical resolution of the MHD simulation. We apply the self-consistent models describing the propagation of high-energy CRs in the absence of perpendicular diffusion to a single snapshot extracted from the TIGRESS simulation at twice the standard resolution ($\Delta x = 4 \text{ pc}$) and to multiple snapshots at lower resolutions ($\Delta x = 16 \text{ pc}$ and $\Delta x = 32 \text{ pc}$). The results shown for standard resolution are based on postprocessing multiple snapshots and averaging over time

(as in Figure 16). The initial conditions of the simulations at different resolutions are identical to those of the standard simulation ($\Delta x = 8 \text{ pc}$) analyzed in this paper (see Section 2.1).

In the first row of Figure 26, we compare the results from the standard run with higher spatial resolution results. The left panel shows the average scattering coefficient as a function of hydrogen density. Evidently, there is no systematic variation with the resolution of the distribution of scattering coefficient. The deviation between curves for different resolutions near $n_H \simeq 10^{-2} \text{ cm}^{-3}$ is most likely because the high-resolution result is from a single snapshot that has local excursions from a statistically steady state, rather than due to an intrinsic dependence on the spatial resolution. The right panel shows the average vertical profile of CR pressure for both resolutions. The average vertical profiles of thermal pressure, vertical kinetic pressure, and vertical magnetic stress from the high-resolution snapshot are also shown. The shaded areas around the temporally averaged standard-resolution profiles (red lines) cover the 16th to 84th percentiles of temporal fluctuations. The high-resolution pressure profile is consistent with the low-resolution one and, most importantly, lies within the shaded area indicative of temporal fluctuations around the mean profile. As found for the standard-resolution simulation, the CR pressure is a factor ~ 3 higher than the other relevant pressures in the midplane (see Section 4 and Figure 14).

The second and third rows of Figure 26 show the comparisons between the time-averaged results of the standard simulation and the time-averaged results of the simulations with lower resolutions, respectively $\Delta x = 16 \text{ pc}$ and $\Delta x = 32 \text{ pc}$. For the run at 16 pc , the average scattering coefficient distribution is in very good agreement with the standard distribution, even though characterized by larger temporal fluctuations. The average CR pressure profile is consistent with the standard profile at high latitudes ($z \gtrsim 1 \text{ kpc}$), while it lies slightly above that near the midplane. The agreement considerably worsens when we further halve the resolution. Even though the average scattering coefficient distributions obtained from the runs at 8 pc and 32 pc are roughly consistent,

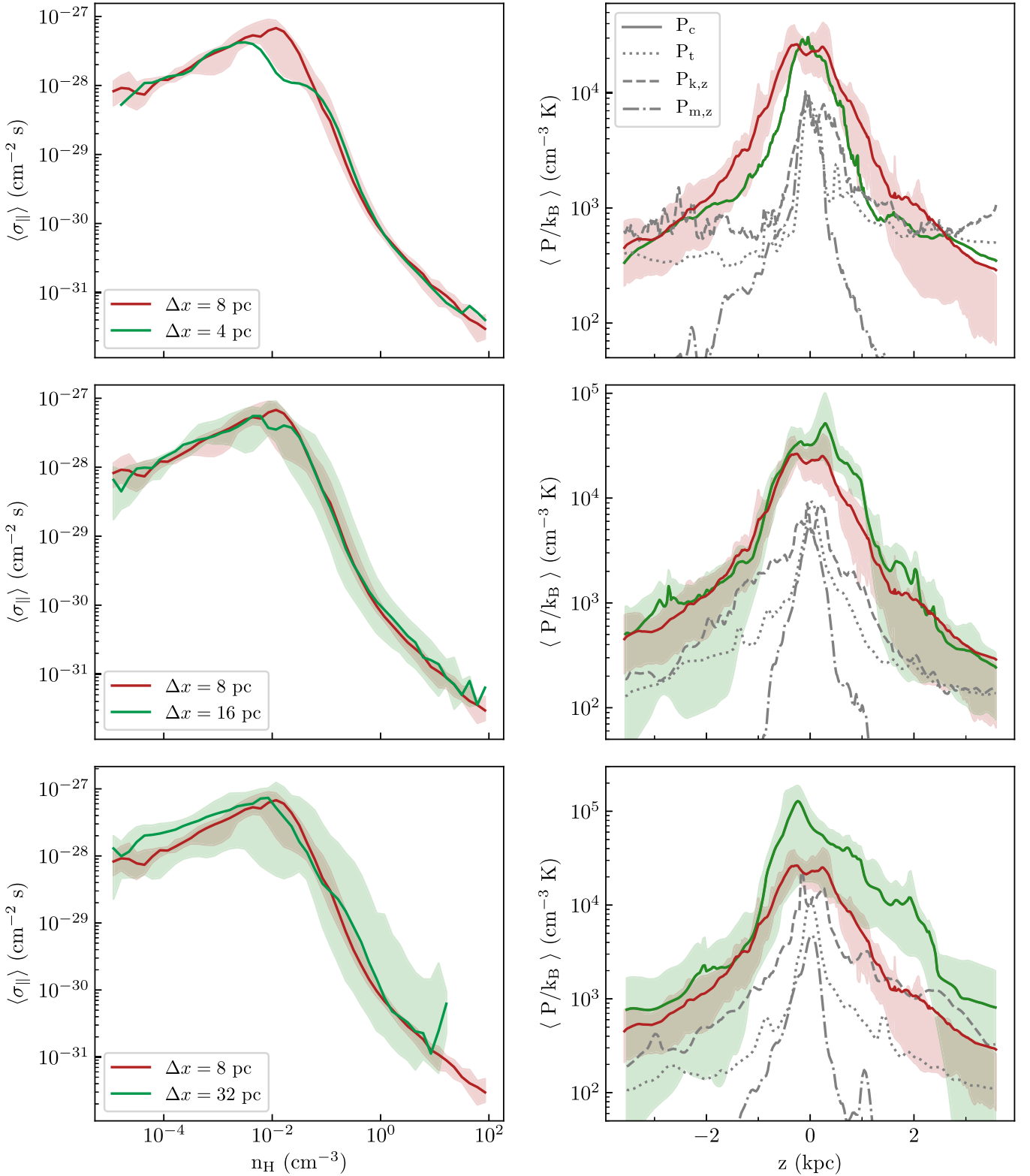


Figure 26. Resolution comparison for self-consistent CR propagation model without perpendicular diffusion. From top to bottom, each row shows the comparison between the results obtained by postprocessing the TIGRESS simulation at standard resolution ($\Delta x = 8$ pc—red lines and shaded areas) and the results obtained from simulations with resolution $\Delta x = 4$ pc, 16 pc, and 32 pc (green lines and shaded areas), respectively. While the results at resolutions $\Delta x \geq 8$ pc are averaged in time over multiple snapshots, the results at resolution $\Delta x = 4$ pc are for a single snapshot. Left panel: median scattering coefficient σ_{\parallel} as a function of hydrogen density n_{H} . Right panel: average vertical profiles of CR pressure P_{c} . For the run at resolutions $\Delta x \geq 8$ pc, the shaded areas cover the 16th to 84th percentiles of temporal fluctuations. The gray lines show the horizontally averaged profiles of thermal pressure P_{t} (dotted line), vertical kinetic pressure $P_{\text{k},z}$ (dashed line), and magnetic stress $P_{\text{m},z}$ (dotted-dashed line) extracted from the high-resolution snapshot (first row) and time-averaged over multiple snapshots at resolution $\Delta x = 16$ pc (second row) and 32 pc (third row).

the latter presents temporal fluctuations over more than one order of magnitude, meaning that the distribution of σ significantly changes from one snapshot to another. The low-resolution average profile of CR pressure is always above the standard profile and, as for σ_{\parallel} , is characterized by large temporal fluctuations. Near the midplane, the average CR pressure increases by almost one order of magnitude going from $\Delta x = 8$ pc to $\Delta x = 32$ pc. At the same time, the run at 32 pc presents higher thermal and kinetic pressures in the disk compared to the runs at $\Delta x \leq 16$ pc, as well as a very large range of SFR (see Kim & Ostriker 2017). We conclude that models with $\Delta x \leq 16$ pc are converged, thus confirming that the spatial resolution of 8 pc is sufficient to achieve robust convergence of the CR properties analyzed in this paper.

We note that moving-mesh simulations typically have resolutions much lower than fixed-grid simulations in low-density gas. For example, cosmological zoom simulations with a mass resolution of $10^4 M_{\odot}$ correspond to spatial resolution $\Delta x = 66$ pc ($n_{\text{H}}/1 \text{ cm}^{-3}$). The warm-cold ISM at $n_{\text{H}} \sim 0.1\text{--}100 \text{ cm}^{-3}$ would have $\Delta x = 140\text{--}14$ pc, while the hot ISM at $n < 0.01 \text{ cm}^{-3}$ would have $\Delta x > 300$ pc. The above analysis regarding resolution dependence suggests that while the scattering rate coefficients of these simulations may be in agreement with higher resolution simulations, the CR distribution itself may not be converged.

ORCID iDs

Lucia Armillotta  <https://orcid.org/0000-0002-5708-1927>

Eve C. Ostriker  <https://orcid.org/0000-0002-0509-9113>

Yan-Fei Jiang (姜燕飞)  <https://orcid.org/0000-0002-2624-3399>

References

- Ackermann, M., Ajello, M., Albert, A., et al. 2014, *Sci*, **345**, 554
- Aguilar, M., Aisa, D., Alpat, B., et al. 2015, *PhRvL*, **115**, 211101
- Aguilar, M., Aisa, D., Alvino, A., et al. 2014, *PhRvL*, **113**, 121102
- Amato, E., & Blasi, P. 2018, *AdSpR*, **62**, 2731
- Bacalla, X. L., Linnartz, H., Cox, N. L. J., et al. 2019, *A&A*, **622**, A31
- Bai, X.-N., Ostriker, E. C., Plotnikov, I., & Stone, J. M. 2019, *ApJ*, **876**, 60
- Bambic, C. J., Bai, X.-N., & Ostriker, E. C. 2021, arXiv:2102.11877
- Beck, R. 2001, *SSRv*, **99**, 243
- Beck, R., & Krause, M. 2005, *AN*, **326**, 414
- Bell, A. R. 1978, *MNRAS*, **182**, 147
- Blandford, R. D., & Ostriker, J. P. 1978, *ApJL*, **221**, L29
- Blasi, P., Amato, E., & Serpico, P. D. 2012, *PhRvL*, **109**, 061101
- Boulares, A., & Cox, D. P. 1990, *ApJ*, **365**, 544
- Breitschwerdt, D., McKenzie, J. F., & Voelk, H. J. 1991, *A&A*, **245**, 79
- Chan, T. K., Kereš, D., Hopkins, P. F., et al. 2019, *MNRAS*, **488**, 3716
- Chandran, B. D. G. 2000, *ApJ*, **529**, 513
- Crocker, R. M., Krumholz, M. R., & Thompson, T. A. 2021, *MNRAS*, **502**, 1312
- Cummings, A. C., Stone, E. C., Heikkilä, B. C., et al. 2016, *ApJ*, **831**, 18
- Dorfi, E. A., & Breitschwerdt, D. 2012, *A&A*, **540**, A77
- Draine, B. T. 2011, *Physics of the Interstellar and Intergalactic Medium* (Princeton, NJ: Princeton Univ. Press)
- Everett, J. E., Zweibel, E. G., Benjamin, R. A., et al. 2008, *ApJ*, **674**, 258
- Evoli, C., Blasi, P., Morlino, G., & Aloisio, R. 2018, *PhRvL*, **121**, 021102
- Farber, R., Ruszkowski, M., Yang, H. Y. K., & Zweibel, E. G. 2018, *ApJ*, **856**, 112
- Farmer, A. J., & Goldreich, P. 2004, *ApJ*, **604**, 671
- Gatto, A., Walch, S., Naab, T., et al. 2017, *MNRAS*, **466**, 1903
- Girichidis, P., Naab, T., Hanasz, M., & Walch, S. 2018, *MNRAS*, **479**, 3042
- Girichidis, P., Naab, T., Walch, S., et al. 2016, *ApJL*, **816**, L19
- Grenier, I. A., Black, J. H., & Strong, A. W. 2015, *ARA&A*, **53**, 199
- Guo, Y.-Q., Tian, Z., & Jin, C. 2016, *ApJ*, **819**, 54
- Hanasz, M., Lesch, H., Naab, T., et al. 2013, *ApJL*, **777**, L38
- Hanasz, M., Strong, A., & Girichidis, P. 2021, *LRCA*, **7**, 2
- Holguin, F., Ruszkowski, M., Lazarian, A., Farber, R., & Yang, H. Y. K. 2019, *MNRAS*, **490**, 1271
- Hopkins, P. F., Squire, J., Chan, T. K., et al. 2021, *MNRAS*, **501**, 4184
- Hopkins, P. F., Wetzel, A., Kereš, D., et al. 2018, *MNRAS*, **480**, 800
- Indriolo, N., & McCall, B. J. 2012, *ApJ*, **745**, 91
- Indriolo, N., Neufeld, D. A., Gerin, M., et al. 2015, *ApJ*, **800**, 40
- Jiang, Y.-F., & Oh, S. P. 2018, *ApJ*, **854**, 5
- Jóhannesson, G., Ruiz de Austri, R., Vincent, A. C., et al. 2016, *ApJ*, **824**, 16
- Kim, C.-G., & Ostriker, E. C. 2015, *ApJ*, **815**, 67
- Kim, C.-G., & Ostriker, E. C. 2017, *ApJ*, **846**, 133
- Kim, C.-G., & Ostriker, E. C. 2018, *ApJ*, **853**, 173
- Kim, C.-G., Ostriker, E. C., & Kim, W.-T. 2013, *ApJ*, **776**, 1
- Kim, C.-G., Ostriker, E. C., Somerville, R. S., et al. 2020a, *ApJ*, **900**, 61
- Kim, W.-T., Kim, C.-G., & Ostriker, E. C. 2020b, *ApJ*, **898**, 35
- Korsmeier, M., & Cuoco, A. 2016, *PhRvD*, **94**, 123019
- Kroupa, P. 2001, *MNRAS*, **322**, 231
- Krumholz, M. R., Crocker, R. M., Xu, S., et al. 2020, *MNRAS*, **493**, 2817
- Kulsrud, R., & Pearce, W. P. 1969, *ApJ*, **156**, 445
- Kulsrud, R. M. 2005, *Plasma Physics for Astrophysics* (Princeton, NJ: Princeton Univ. Press)
- Kulsrud, R. M., & Cesarsky, C. J. 1971, *ApL*, **8**, 189
- Lazarian, A. 2016, *ApJ*, **833**, 131
- Leitherer, C., Schaerer, D., Goldader, J. D., et al. 1999, *ApJS*, **123**, 3
- Longair, M. S. 1994, *High Energy Astrophysics. Vol. 2: Stars, the Galaxy and the Interstellar Medium* (Cambridge: Cambridge Univ. Press)
- Mao, S. A., & Ostriker, E. C. 2018, *ApJ*, **854**, 89
- Morlino, G., & Caprioli, D. 2012, *A&A*, **538**, A81
- Neufeld, D. A., & Wolfire, M. G. 2017, *ApJ*, **845**, 163
- Ostriker, E. C., McKee, C. F., & Leroy, A. K. 2010, *ApJ*, **721**, 975
- Ostriker, E. C., & Shetty, R. 2011, *ApJ*, **731**, 41
- Padovani, M., Ivlev, A. V., Galli, D., & Caselli, P. 2018, *A&A*, **614**, A111
- Padovani, M., Ivlev, A. V., Galli, D., et al. 2020, *SSRv*, **216**, 29
- Pakmor, R., Pfrommer, C., Simpson, C. M., & Springel, V. 2016, *ApJL*, **824**, L30
- Parker, E. N. 1969, *SSRv*, **9**, 651
- Plotnikov, I., Ostriker, E. C., & Bai, X.-N. 2021, *ApJ*, **914**, 3
- Ruszkowski, M., Yang, H. Y. K., & Zweibel, E. 2017, *ApJ*, **834**, 208
- Schlickeiser, R. 1989, *ApJ*, **336**, 243
- Seta, A., & Beck, R. 2019, *Galax*, **7**, 45
- Shalchi, A. 2019, *ApJL*, **881**, L27
- Shalchi, A. 2020, *SSRv*, **216**, 23
- Silsbee, K., & Ivlev, A. V. 2019, *ApJ*, **879**, 14
- Simpson, C. M., Pakmor, R., Marinacci, F., et al. 2016, *ApJL*, **827**, L29
- Skilling, J. 1971, *ApJ*, **170**, 265
- Skinner, M. A., & Ostriker, E. C. 2013, *ApJS*, **206**, 21
- Stepanov, R., Shukurov, A., Fletcher, A., et al. 2014, *MNRAS*, **437**, 2201
- Stone, J. M., & Gardiner, T. A. 2010, *ApJS*, **189**, 142
- Stone, J. M., Gardiner, T. A., Teuben, P., Hawley, J. F., & Simon, J. B. 2008, *ApJS*, **178**, 137
- Stone, J. M., Tomida, K., White, C. J., & Felker, K. G. 2020, *ApJS*, **249**, 4
- Strong, A. W., Moskalenko, I. V., & Ptuskin, V. S. 2007, *ARNPS*, **57**, 285
- Sutherland, R. S., & Dopita, M. A. 1993, *ApJS*, **88**, 253
- Trotta, R., Jóhannesson, G., Moskalenko, I. V., et al. 2011, *ApJ*, **729**, 106
- Vijayan, A., Kim, C.-G., Armillotta, L., Ostriker, E. C., & Li, M. 2020, *ApJ*, **894**, 12
- Wentzel, D. G. 1974, *ARA&A*, **12**, 71
- Werhahn, M., Pfrommer, C., Girichidis, P., Puchwein, E., & Pakmor, R. 2021, *MNRAS*, **505**, 3273
- Wiener, J., Zweibel, E. G., & Oh, S. P. 2018, *MNRAS*, **473**, 3095
- Xu, S., & Lazarian, A. 2017, *NJPh*, **19**, 065005
- Yan, H., & Lazarian, A. 2002, *PhRvL*, **89**, 281102
- Yeast-Hull, T. M., Gallagher, J. S., & Zweibel, E. G. 2016, *MNRAS*, **457**, L29
- Zweibel, E. G. 2013, *PhPI*, **20**, 055501
- Zweibel, E. G. 2017, *PhPI*, **24**, 055402